# Mathematical techniques for free boundary problems with multiple boundaries

A thesis presented for the degree of

Doctor of Philosophy of Imperial College London

and the

Diploma of Imperial College

by

**CHRISTOPHER GREEN**

Department of Mathematics

Imperial College London

180 Queen's Gate, London, SW7 2AZ

United Kingdom

18 FEBRUARY 2013

I certify that this thesis, and the research to which it refers, is the product of my own work, and that any ideas or quotations from the work of other people, published or otherwise, are fully acknowledged in accordance with the standard referencing practices of the discipline.

*Christopher Green*

# Copyright

Copyright in text of this thesis rests with the Author. Copies (by any process) either in full, or of extracts, may be made **only** in accordance with instructions given by the Author and lodged in the doctorate thesis archive of the Imperial College Central Library. Details may be obtained from the Librarian. This page must form part of any such copies made. Further copies (by any process) of copies made in accordance with such instructions may not be made without the permission (in writing) of the Author.

The ownership of any intellectual property rights which may be described in this thesis is vested in Imperial College, subject to any prior agreement to the contrary, and may not be made available for use by third parties without the written permission of Imperial College, which will prescribe the terms and conditions of any such agreement. Further information on the conditions under which disclosures and exploitation may take place is available from the Imperial College registry.

Dedicated to my parents, Keith and Debra.

# Acknowledgements

My time as a PhD student has been truly enlightening, on several different levels. I feel privileged to have had such an amazing experience. I am indebted to many people who have been so supportive of me over the past $3\frac{1}{2}$ years.

First and foremost, I express my sincere gratitude to my parents. Without their love and continued support, guidance and encouragement, I have no doubt that this thesis would not have been written. I express my sincere gratitude to my friends for their encouragement and their understanding. I am also very appreciative of the support that I have received from my godfather David Sleep.

I gratefully acknowledge, and am very appreciative, of all the mathematical training that I have received from my supervisor Darren Crowdy. I would like to sincerely thank Jonathan Marshall for his support and several enlightening conversations. Finally, I also wish to thank several individuals at various institutions around the world for making my overseas visits both worthwhile and memorable; in particular, special thanks must go to Giovani Vasconcelos.

*Christopher Green*

# Abstract

In this thesis, we study six different free boundary problems arising in the field of fluid mechanics, and the mathematical methods used to solve them. The free boundary problems are all characterised by having more than one boundary and the solution of these problems requires special mathematical treatment. The challenge in each of these problems is to determine the shape of the multiple fluid interfaces making up the particular system under consideration.

In each of the free boundary problems we employ aspects of complex function theory, conformal mapping between multiply connected domains, and specialist techniques devised in recent years by Crowdy and collaborators. At the heart of these techniques lies a special transcendental function known as the Schottky-Klein prime function. This thesis makes use of this function in a variety of novel contexts.

We first examine a single row of so-called hollow vortices in free space. This problem has been solved before but we present a new methodology which is convenient in being extendible to the case of a double row, or von Kármán vortex street, of hollow vortices. We find a concise formula for the conformal mapping describing the shapes of the free boundaries of two hollow vortices in a typical period window in the vortex street and thereby solve the free boundary problem.

We next focus on the problem of a pair of hollow vortices in an infinite channel. This free boundary problem exhibits similar mathematical features to the vortex street problem but now involves the new ingredient of solid impenetrable walls. Again we solve the free boundary problem by finding a concise formula for the conformal mapping governing the hollow vortex shapes. We then extend this analysis to a single row of hollow vortices occupying the channel.

The problem of a pair of hollow vortices of equal and opposite circulation positioned behind a circular cylinder, superposed with a uniform flow, is then considered. This system is a desingularisation of the so-called Föppl point vortex equilibrium. For this free boundary problem, we employ a hybrid analytical-numerical scheme and we are able to offer a Fourier-Laurent series expansion for the conformal mapping determining the shape of the hollow vortex boundaries.

Finally, we investigate an asymmetric assembly of steadily translating bubbles in a Hele-Shaw channel. This free boundary problem can be formulated as a special Riemann-Hilbert problem solvable in terms of the Schottky-Klein prime function. Our method of solution can be used to determine the shapes of any finite number of bubbles in a given assembly.

# Table of contents

# Chapter 1

# Introduction

This thesis concerns solving variants of a special type of mathematical problem in geometries of multiple connectivity. This special type of problem is known as a free boundary problem. By associating the term 'multiple connectivity' with a particular geometry, we mean that the geometry in consideration has more than one boundary component. Finding solutions to boundary value problems involving multiply connected geometries is always challenging owing to multiple requirements having to be satisfied simultaneously on all the boundary components and the associated search for suitable mathematical functions which can capture all necessary details. *Free* boundary problems in multiply connected geometries possess an even greater level of difficulty: these problems are characterised by the fact that the boundaries themselves are unknown *a priori* and must be determined as part of the solution.

In this thesis, we will consider six different free boundary problems in various multiply connected geometries which all arise in the field of fluid mechanics. We are motivated by the desire to understand certain configurations of multiple fluid interfaces and the specialised mathematical methods which must be summoned so that these free boundary problems can be successfully tackled. Due to the fact that the governing equation in each of the free boundary problems to be considered in this thesis is Laplace's equation in two dimensions, our problems naturally lend themselves to being solved using the powerful armoury of complex analysis and complex function theory. This is because both the real and imaginary parts of a complex-valued analytic function satisfy Laplace's equation.

Indeed, making progress when solving problems in two-dimensional fluid mechanics usually involves finding an analytic function known as the complex potential which encapsu-

lates the main characteristics of the physical system in consideration. In certain problems (such as those considered in this thesis), we can appeal to their conformal invariance: this important property essentially permits the use of conformal mapping so that the problem can be posed in a simplified geometrical framework, and thereby solved. To illustrate this notion, suppose the complex potential $w(z)$ in the physical fluid domain in a $z$-plane is defined through the composition $W(\zeta) = w(z(\zeta))$, where $z(\zeta)$ is a conformal mapping from some simple geometry in a $\zeta$-plane (often taken to be a circular domain i.e. a domain whose boundary is a union of circles) to the physical domain in the $z$-plane. Then, provided we can construct the functions $W(\zeta)$ and $z(\zeta)$ in our chosen $\zeta$-plane, the problem is solved.

This idea of 'pulling-back' to a simpler domain can be utilised in free streamline theory. Free streamline theory can originally be attributed to the work of von Helmholtz [119] on discontinuous fluid motion, and was subsequently developed by Kirchhoff and Rayleigh. The subject of free streamline theory is vast and there are many sources one can turn to in the literature; for example, Milne-Thomson [79] and Sedov [102]. An accessible discussion of the development of free streamline theory is given in Sobey [105]. This discussion is mirrored in the introduction of the work of Michell [77]. In this remarkably detailed paper, Michell builds on the work of von Helmholtz, Kirchhoff and Rayleigh by using Schwarz-Christoffel methods (i.e. conformal mappings to simply connected polygonal domains, see Nehari [84]) to give "a general solution of the problem of free non-reentrant stream lines with plane rigid boundaries" with applications to problems of condensers and hollow vortices. The content of Chapters 3-5 in this thesis is devoted to free boundary problems involving hollow vortices and are solved using ideas involving free streamline theory. We discuss the general properties of hollow vortices later in this chapter.

The monographs by Acheson [2] and Batchelor [8] explain how the techniques of complex analysis can be used to solve several basic problems in fluid mechanics, whilst the monograph by Saffman [93] presents a comprehensive overview of various problems, also using complex analysis techniques, arising specifically in vortex dynamics. Most of these problems are set in simply connected domains which are relatively simple to analyse and solutions can be written down in closed analytical form. An example of such a solution is the complex potential for steady uniform flow past an aerofoil which can be derived using the well-known Joukowski map (Nehari [84]). Saffman & Sheffield [97], with the intention of understanding lift enhancement by trapped vortices, used the Joukowski map in their model of an attached free point vortex above a flat plate. Some problems involving

two boundaries are able to be tackled provided one is proficient in the use of elliptic functions (Akhiezer [3]). For example, Lagally [68] constructed the complex potential for the so-called 'bi-plane' problem of uniform flow past two circular aerofoils in terms of elliptic functions, and Johnson & McDonald [61] were able to determine the trajectories of a point vortex in motion around two circular obstacles also by employing elliptic function theory. However, there appears to have been a distinct lack of analytical solutions for uniform flow around multiple obstacles until relatively recently. Crowdy [14, 22] has built what can be regarded as a 'new calculus' for solving inviscid fluid flow problems in multiply connected geometries. The success of his approach comes from employing a special transcendental function called the Schottky-Klein prime function and its associated function theory (the subject of Chapter 2), alongside sophisticated conformal mapping techniques, to derive general analytical expressions for the complex potentials describing particular flows. A remarkable feature of this work is that each complex potential takes exactly the same functional form regardless of the connectivity of the problem. By exploiting his new calculus, Crowdy [15] has also been able to generalise the 'bi-plane' solution of Lagally [68] to the case of an arbitrary finite number of aerofoils in a uniform stream. We will employ Crowdy's new calculus in our work in Chapter 5. Now, although the aforementioned works of this paragraph do not pertain to free boundary problems, they collectively imply that in order to find analytical solutions to problems in multiply connected geometries, the development of new analytical techniques and the use of specialised mathematics is essential.

Indeed, until relatively recently, problems arising in general multiply connected domains usually evaded being solved analytically. Over the past decade, Crowdy and collaborators have been able to formalise novel constructive techniques for solving various problems in multiply connected domains. Their approach centres around the usage of the Schottky-Klein prime function and its associated function theory, and we advocate their approach throughout this thesis. Crowdy and collaborators have pointed out on a number of occasions that this special function plays a central role in problems involving multiply connected geometries and can be used to great advantage in many applications (even though it has scarcely made an appearance in the applied mathematical literature until relatively recently). In addition to the new calculus proposed by Crowdy [14, 22], the Schottky-Klein prime function can claim to have had a profound impact on the field of conformal mapping between multiply connected domains. Crowdy [13, 16] used the Schottky-Klein prime function in his construction of generalised Schwarz-Christoffel formulae for the conformal mappings to the interior and exterior of multiply connected polygonal regions, whilst

Crowdy, Fokas & Green [36] used the Schottky-Klein prime function in combination with automorphic function theory (Ford [47]) to show that the conformal mappings to multiply connected polycircular arc domains are the solutions of a third order non-linear differential equation involving Schwarzian derivatives. Furthermore, Crowdy & Marshall [29] have constructed analytical formulae, expressed in terms of the Schottky-Klein prime function, for the special conformal mappings from bounded multiply connected circular domains to various multiply connected slit domains. The use of these conformal slit mappings is central to solving the free boundary problems of Chapters 3, 4 and 6, and we will introduce the ones we shall use in Chapter 2.

Free boundary problems arise in many areas of the applied sciences and manifest themselves in a variety of different forms. The review by Friedman [48] surveys some recent free boundary problems occurring in different scientific fields by outlining two broad types of free boundary problem known as obstacle problems and Stefan problems. For free boundary problems set in multiply connected domains, very few analytical solutions exist in the literature. We will now survey some free boundary problems set in various multiply connected domains which have been successfully tackled using complex analysis techniques. Our intention is to give a flavour of the nature of these problems, in addition to the general types of mathematical methods which have been used to solve them, as a prelude to the free boundary problems we shall address in this thesis.

A free boundary problem which exploits conformal mapping ideas in a doubly connected setting is explored in the interesting study of Milton & Serkov [80]. They consider a thin material plate with a hole taken to be surrounded by an isotropic coating of some conductivity. Their free boundary problem, which consists of finding all admissible doubly connected coating regions (and hence the shapes of the simply connected hole), is solved by constructing a conformal map, in terms of a Fourier-Laurent series expansion, from a concentric annulus to the doubly connected region of the coating. When it is not possible to find explicit analytical solutions to a particular problem, choosing to adopt these Fourier-Laurent series expansions is a very convenient way of still enabling solutions to be constructed. We have to resort to using such representations in Chapter 5. Another example of a free boundary problem over a doubly connected domain is the problem of slow viscous flow of an annular viscous drop driven by surface tension. This time-dependent biharmonic problem was solved exactly by Crowdy & Tanveer [34] using elements of automorphic function theory.

Many free boundary problems naturally arise from the consideration of different types of Hele-Shaw system. We will focus on one such system in Chapter 6. A Hele-Shaw system is where two fluids (one viscous and one inviscid) which are sandwiched between two close-to-touching parallel plates produces a flow which is essentially two-dimensional for modelling purposes. Hele-Shaw flows in various geometries have been extensively studied over the years and evidently, many processes in physics involving the evolution of interfacial boundaries, such as dendritic crystal growth, direct solidification, and fluid displacement, can be modelled mathematically (under certain assumptions) as a free boundary problem of the Hele-Shaw type. This diverse array of free boundary problems has a plethora of analytical solutions, many of which are exact, and a wide scope of mathematical methods can be used to solve them. The models defining these free boundary problems also go by the name of 'Laplacian growth processes' because the governing field equation in the fluid is Laplace's equation and the evolution of the fluid interfaces is governed through surface derivatives of this field. In the case of Hele-Shaw bubbles, the flow is governed by Darcy's law and the bubble interfaces evolve with a velocity proportional to the local gradient of the fluid pressure.

A free boundary problem solved over a general multiply connected fluid domain in a Hele-Shaw system is presented by Richardson [91]. He considered the problem of fluid injection into an empty Hele-Shaw cell and developed analytical solutions describing growing circular regions of the injected fluid which merge together in the ensuing motion to form some multiply connected region. This free boundary problem is time-dependent, and extends an earlier work of his (Richardson [90]). In this earlier work [90], Richardson laid down the mathematical formalism for both problems in [90, 91], but only considered in detail the fluid motion in a particular doubly connected configuration. This required the use of elliptic function theory. In both works [90, 91], Richardson ingeniously employed the Cauchy transform alongside various complex analysis techniques. In [91], the multiply connected region occupied by the fluid at some point in time is determined by a conformal map from some bounded multiply connected circular domain. This conformal map is found to be an automorphic function with respect to the Schottky group of the preimage circular domain (we define Schottky groups in Chapter 2), and is constructed as a ratio of Poincaré theta series. This work by Richardson [91] is important because it demonstrates the key role of the theory of Schottky groups and automorphic functions when solving problems in multiply connected geometries, and motivates our decision to employ the Schottky-Klein prime function and its associated function theory when solving the problems of this thesis. It is

important to point out that Richardson [90, 91] did not make use of, or even mention, the Schottky-Klein prime function. His work was later reappraised by Crowdy & Marshall [27].

The results in [91] are also significant in the following sense: they can be interpreted in terms of quadrature domains (Gustafsson & Shapiro [56]). Quadrature domains are essentially special planar domains which are characterised by quadrature rules, and they turn out to be useful mathematical objects in a number of different physical problems (often because they are preserved by the dynamics of the problem). In fact, there are several strong connections between the theory of quadrature domains and various free boundary problems arising in fluid mechanics (see Crowdy [12]). Motivated by these numerous applications, Crowdy & Marshall [27, 33] have devised ways to reconstruct multiply connected quadrature domains using conformal mappings written in terms of Schottky-Klein prime functions. The theory of quadrature domains is also exploited in the work by Crowdy & Kang [26]. By using the fact that the boundaries of quadrature domains are algebraic curves, Crowdy & Kang [26] were able to solve the time-dependent free boundary problem of the so-called 'squeezing flow' of multiply connected fluid domains in a Hele-Shaw cell. They constructed exact analytical solutions by tracking a finite set of time-dependent parameters governing the evolution of a multiply connected fluid domain under the squeeze flow.

A free boundary problem which has been solved recently and which employs conformal mapping methods involving the function theory of the Schottky-Klein prime function is presented by Marshall [75]. Marshall has constructed a special class of solutions describing steady flows in multiply connected regions of uniform vorticity surrounding an assembly of multiple finite-length flat plates. His sophisticated construction relies upon the use of the Schwarz function (Davis [38]) and the proceeding through an intermediate multiply connected parallel slit domain (Crowdy & Marshall [29]). He ends up solving a modified Schwarz problem for the conformal map determining the shapes of the free boundaries of the uniform vorticity region for a given assembly of plates: such a problem when posed in a multiply connected circular domain has a concise integral formula solution whose kernels are expressed in terms of the Schottky-Klein prime function (Crowdy [18]). In doing so, he was able to extend the two works of Johnson & McDonald [63, 64] who considered separately the cases of steady vortical flows around a single plate and a periodic array of plates. For four of the free boundary problems we shall treat in this thesis, the reader will detect several analogies with the approach and ideas of Marshall [75]; indeed, when solving

these problems, we shall also employ conformal slit mappings and will construct analytical formulae, expressed in terms of Schottky-Klein prime functions, for the conformal maps describing the shapes of the free boundaries we seek.

Hollow vortices are the principal fluid dynamical objects of focus motivating the majority of the free boundary problems of this thesis and so it is only appropriate that in the remainder of this chapter, we elucidate their main characteristics and discuss existing works involving them. As we shall see in this thesis, modelling hollow vortices requires solving complicated free boundary problems. A hollow vortex is defined to be a finite-area region containing vacuum at constant pressure which is bounded by a vortex sheet of uniform strength; that is, the vorticity associated with it is confined to be on its free boundary whose shape will need to be determined. In two dimensions, this free boundary is a simple closed curve and if it is in steady equilibrium, is necessarily a streamline of the flow. If the fluid in which the hollow vortex is immersed is at constant pressure, then in order that there is continuity of pressure across the vortex sheet, Bernoulli's theorem implies that the fluid speed on the vortex sheet must be constant. The hollow vortex model is an example of a classical distributed vorticity model. Distributed vorticity models are desingularisations of point vortex models in the following sense: the fluid velocity field induced by a point vortex is singular at the location of the point vortex whilst for a vortex with distributed vorticity, the fluid velocity field is non-singular at all points in the flow. Another example of a distributed vorticity model is that of the vortex patch which is a finite-area region of constant vorticity (Saffman [93]).

Even though the hollow vortex model is a classical model dating back to the late nineteenth century, many analytical solutions describing hollow vortices have remained undiscovered until relatively recently, and there are likely still many more to be found. This thesis will present many new such analytical solutions for hollow vortices in some typical physical configurations. Our new solutions are valuable: exact solutions of the two-dimensional Euler equations in vortical flow problems are hard to attain and few exist. The 1884 work of Hicks [60] is one of the first papers in which the hollow vortex model features. Hicks used so-called toroidal functions to derive some approximation formulae for the steady motion of a single hollow vortex. Michell [77] studied a single hollow vortex in an infinite channel by employing Schwarz-Christoffel methods and elliptic function theory to derive an analytical formula for its free boundary shape. Pocklington [85] focused on a co-travelling hollow vortex pair in unbounded fluid. Like Michell [77], Pocklington also

utilised Schwarz-Christoffel methods and elliptic functions to derive an analytical solution for the free boundaries of the hollow vortices. In Chapter 4, we will generalise both the works of Michell [77] and Pocklington [85].

Around eighty years after the work of Pocklington [85], Baker, Saffman & Sheffield [7] undertook a study into a single row of hollow vortices in unbounded fluid. By employing free streamline theory alongside Schwarz-Christoffel methods, and appreciating the intrinsic periodicity structure of the row, they found an exact solution for the conformal map determining the shape of a typical hollow vortex member in the row. Our work in Chapter 3 can be viewed as the generalisation of this solution due to Baker, Saffman & Sheffield [7] to a von Kármán street of hollow vortices (two rows of hollow vortices). Recently, Llewellyn Smith & Crowdy [72] analysed the effect of placing a single hollow vortex in an ambient irrotational straining flow and employed free streamline theory to establish an exact analytical solution for the shape of the hollow vortex boundary. Also, Crowdy, Llewellyn Smith & Freilich [37] have presented a new derivation and representation of Pocklington's solution [85] for a co-travelling hollow vortex pair. Appealing to free streamline theory, they were able to derive an explicit indefinite integral for the conformal mapping, expressed in terms of Schottky-Klein prime functions, determining the hollow vortex boundary shapes.

This thesis will showcase six free boundary problems defined over different multiply connected domains. Each of the problems considered in this thesis is amenable to techniques of conformal mapping and complex variable theory. Throughout, we shall focus on devising novel and sophisticated constructive methods of solution to each of our free boundary problems and exploit the rich function theory associated with the Schottky-Klein prime function. This thesis is structured as follows. In Chapter 2, we present an overview of the Schottky-Klein prime function and its associated function theory. In Chapters 3-5, hollow vortices in different configurations are studied, while in Chapter 6, a particular type of Hele-Shaw system is examined. In Chapter 3, we study a row and a street of hollow vortices in unbounded fluid; much of the material in Chapter 3 forms the content of the paper by Crowdy & Green [25]. In Chapter 4, we consider a pair and a row of hollow vortices in an infinite channel. In Chapter 5, we concentrate on a hollow vortex pair in the wake of a circular obstacle within a uniform flow. Finally in Chapter 6, we consider a finite asymmetric configuration of multiple bubbles moving steadily along a Hele-Shaw channel.

# Chapter 2

# The Schottky-Klein prime function

Since the Schottky-Klein prime function lies at the heart of the mathematical techniques of this thesis, it is instructive to give a brief overview of it and to survey a number of its key properties which we shall employ at various stages. The function theory associated with the Schottky-Klein prime function is both beautiful and powerful, and can be exploited to solve the free boundary problems of this thesis. The Schottky-Klein prime function turns out to be a relatively straightforward mathematical object to compute (we outline a possible method of computation in this chapter) and encapsulates neatly into its very definition certain geometrical properties of the multiply connected domain over which it is defined, regardless of the connectivity; consequently, many formulae written in terms of the Schottky-Klein prime function are concise and mathematically elegant. Further information about the nature of the Schottky-Klein prime function can be found, for example, in the accessible overviews by Crowdy [23, 17], whilst a more detailed treatment is given by Marshall [74].

## 2.1 The Schottky-Klein prime function

To any bounded multiply connected circular domain $D_\zeta$, we can define a Schottky-Klein prime function which we shall denote by

$$\omega(\zeta, \gamma) \tag{2.1}$$

for arbitrary points $\zeta, \gamma \in D_\zeta$. For us, a bounded $(M+1)$ connected circular domain $D_\zeta$ in a parametric $\zeta$-plane will be taken to be the intersection of the interior of the unit $\zeta$-disc and the exterior of $M$ smaller discs lying strictly inside the unit $\zeta$-disc with centres

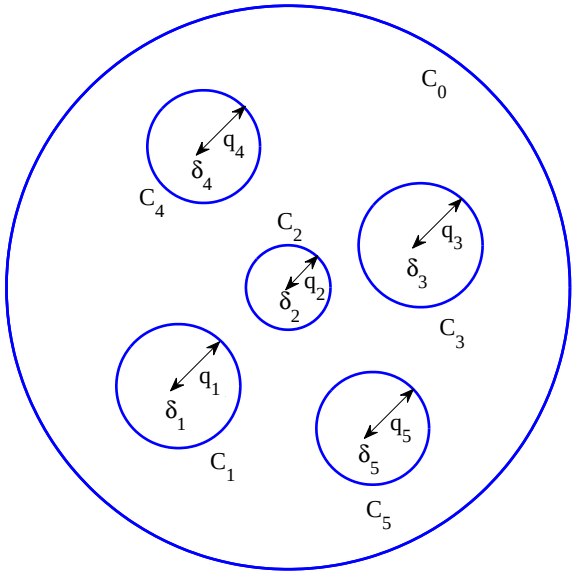


Figure 2.1: Schematic of a typical multiply connected circular domain $D_\zeta$ in the case where $M = 5$. The unit $\zeta$-circle is denoted by $C_0$. The $j$-th interior circle is denoted by $C_j$ and has centre $\delta_j$ and radius $q_j$.

$\{\delta_j \in \mathbb{C} \mid j = 1, ..., M\}$ and radii $\{q_j \in \mathbb{R} \mid j = 1, ..., M\}$; these two sets are together known as the conformal moduli of $D_\zeta$ (see Figure 2.1). Let $C_0$ label the unit $\zeta$-circle and let $C_j$ label the $j$-th interior circle, $j = 1, ..., M$. Strictly speaking, we should denote the Schottky-Klein prime function by

$$\omega(\zeta, \gamma; \delta_1, ..., \delta_M, q_1, ..., q_M) \tag{2.2}$$

to indicate its dependence on the particular circular domain $D_\zeta$ over which it is defined; however, we will drop this lengthy notation and proceed with the understanding that $D_\zeta$ is known. It should be noted that the Schottky-Klein prime function has deep connections with Riemann surface theory (Fay [45]). For the purposes of this thesis, the Schottky-Klein prime function should be thought of as a special computable function in the following sense: a Schottky-Klein prime function can be defined over any given bounded multiply connected circular domain $D_\zeta$ and is uniquely defined at any given pair of points $\zeta, \gamma \in D_\zeta$.

The Schottky-Klein prime function was originally written down independently by both Schottky [101] and Klein [67] in the nineteenth century. Baker's classical monograph on

Abelian functions [6] records the Schottky-Klein prime function; it therein appears in the form of an infinite product:

$$\omega(\zeta,\gamma) = (\zeta-\gamma)\prod_{\theta\in\Theta''}\frac{(\zeta-\theta(\gamma))(\gamma-\theta(\zeta))}{(\zeta-\theta(\zeta))(\gamma-\theta(\gamma))}. \tag{2.3}$$

Here, $\theta$ is a Möbius map belonging to the group $\Theta''$, which we now define. Introduce the $M$ Möbius maps

$$\theta_j(\zeta) = \delta_j + \frac{q_j^2\zeta}{1-\overline{\delta_j}\zeta}, \quad j=1,...,M. \tag{2.4}$$

Let $C_j'$ label the circle which is the reflection of circle $C_j$ in $C_0$. The image under $\theta_j(\zeta)$ of a point $\zeta\in C_j'$ lies on the circle $C_j$ (see Figure 2.2). We let $\Theta$ denote the so-called Schottky group of all compositions of these $M$ Möbius maps $\theta_j(\zeta)$ and their inverses $\theta_j^{-1}(\zeta)$. The subgroup $\Theta''\subset\Theta$ is defined to be the group of all compositions of $\theta_j(\zeta)$ and $\theta_j^{-1}(\zeta)$ but with the inverse composition maps and the identity element excluded; that is, if $\theta_1(\theta_2^{-1}(\zeta))$ is included in the group $\Theta''$, then $\theta_2(\theta_1^{-1}(\zeta))$ must be excluded.

Label by $D_\zeta'$ the region which is the reflection of $D_\zeta$ in $C_0$. Let $F$ be the union of the regions $D_\zeta$ and $D_\zeta'$; then $F$ is known as the fundamental region associated with the Schottky group $\Theta$ (see Figure 2.2). $F$ can be viewed as a model of the two 'sides' of a symmetric genus-$M$ compact Riemann surface called the Schottky double. By genus-$M$, it is understood that the Riemann surface has $M$ 'holes'. Note that the choice of fundamental region is not unique (one could choose to reflect $D_\zeta$ in the circle $C_j$, say, instead of $C_0$).

Associated with a symmetric compact Riemann surface of genus-$M$ is the set of $M$ functions

$$\{v_j(\zeta)\mid j=1,...,M\} \tag{2.5}$$

known as the $M$ integrals of the first kind. These are analytic but not single-valued functions everywhere in $F$. They satisfy the relations

$$v_j(\theta_k(\zeta)) - v_j(\zeta) = \tau_{jk}, \quad j,k=1,...,M, \tag{2.6}$$

where $\tau_{jk}\in\mathbb{C}$ are constants, and the relations

$$\oint_{C_j} d[v_k(\zeta)] = \delta_{jk}, \quad j,k=1,...,M. \tag{2.7}$$

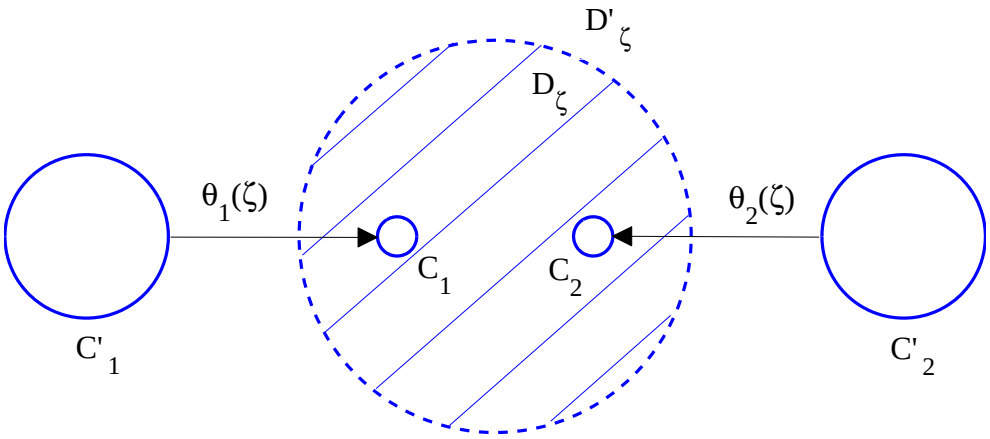


Figure 2.2: Schematic of a typical bounded triply connected circular domain $D_\zeta$ (the area indicated by lines). The action of the Möbius maps $\theta_1(\zeta)$ and $\theta_2(\zeta)$ is shown by the arrows. The two 'halves' of the fundamental region $F$ are labelled by $D_\zeta$ and $D'_\zeta$, respectively. The unit circle $C_0$ is shown by a dashed line.

Here, $\delta_{jk}$ denotes the Kronecker delta function. Henceforth, we shall refer to these relations (2.7) as the 'a-cycle' properties of the $v_j(\zeta)$ functions (following the terminology in Riemann surface theory). The $v_j(\zeta)$ functions are also such that

$$\mathrm{Im}[v_j(\zeta)] = 0, \quad \zeta \in C_0, \tag{2.8}$$

and

$$\mathrm{Im}[v_j(\zeta)] = \gamma_{jk}, \quad \zeta \in C_k, \quad k = 1, ..., M. \tag{2.9}$$

Here, $\gamma_{jk} \in \mathbb{R}$ are constants. The $v_j(\zeta)$ functions are thus uniquely defined up to an additive real constant.

Let

$$X(\zeta, \gamma) = \omega^2(\zeta, \gamma) \tag{2.10}$$

denote the square of the Schottky-Klein prime function $\omega(\zeta, \gamma)$ for a given bounded circular domain $D_\zeta$. Hejhal [59] established four defining properties of function $X(\zeta, \gamma)$ in his monograph:

1. $X(\zeta,\gamma)$ is a single-valued analytic function everywhere in the fundamental region $F$ associated with the Schottky group of $D_\zeta$;

2. $X(\zeta,\gamma)$ has second order zeroes at the set of points $\{\Theta(\gamma) \mid \Theta \in \Theta''\}$;

3. $\lim_{\zeta\to\gamma} X(\zeta,\gamma)/(\zeta-\gamma)^2 = 1$;

4. $X(\zeta,\gamma)$ satisfies the $M$ relations:

$$X(\theta_j(\zeta),\gamma) = H_j(\zeta,\gamma)X(\zeta,\gamma), \quad j = 1,...,M, \tag{2.11}$$

where

$$H_j(\zeta,\gamma) = \exp\left(-4\pi\mathrm{i}v_j(\zeta) + 4\pi\mathrm{i}v_j(\gamma) - 2\pi\mathrm{i}\tau_{jj}\right)\frac{d\theta_j(\zeta)}{d\zeta}, \tag{2.12}$$

and $\{\tau_{jj} \mid j = 1,...,M\}$ is a set of imaginary constants.

The Schottky-Klein prime function $\omega(\zeta,\gamma)$ is then defined to be

$$\omega(\zeta,\gamma) = (X(\zeta,\gamma))^{1/2} \tag{2.13}$$

where the branch of the square root is chosen so that

$$\omega(\zeta,\gamma) \sim \zeta-\gamma, \quad \zeta\to\gamma. \tag{2.14}$$

It is natural to ask why 'prime' appears in the name of the Schottky-Klein prime function. By the Fundamental Theorem of Algebra, we can uniquely factorise a monic degree $N$ complex polynomial $q(\zeta)$ into a product of $N$ monomials:

$$q(\zeta) = \prod_{j=1}^{N}(\zeta-\gamma_j). \tag{2.15}$$

Here, $\gamma_j \in \mathbb{C}$ are the $N$ roots of $q(\zeta)$ lying in the complex plane. By analogy with factorising integers into a product of prime numbers, we call

$$\omega(\zeta,\gamma_j) = \zeta-\gamma_j \tag{2.16}$$

a (Schottky-Klein) prime function. We can say this Schottky-Klein prime function (2.16) is associated with the Riemann sphere; indeed, the complex plane is 'equivalent' to the

Riemann sphere via stereographic projection. Moreover, we can also say this Schottky-Klein prime function (2.16) is associated with the unit disc because the fundamental region associated with the unit disc is the complex plane. Rational functions are the simplest kinds of meromorphic function on the Riemann sphere, and these can easily be factorised into a product of ratios of Schottky-Klein prime functions of the form (2.16).

But what about factorising meromorphic functions on higher genus compact Riemann surfaces? With a genus-$M$ compact Riemann surface, we can associate a bounded $(M+1)$ connected circular domain $D_\zeta$; this is analogous to the association made between the Riemann sphere (a genus-0 compact Riemann surface) and the unit disc. Thus, the Schottky-Klein prime function $\omega(\cdot,\cdot)$ associated with $D_\zeta$ is the generalisation of (2.16) to these higher genus compact Riemann surfaces. It is through the Schottky-Klein prime function that we can represent meromorphic functions $\mathcal{M}(\zeta)$ on higher genus compact Riemann surfaces; these functions can also be factorised into a product of ratios of Schottky-Klein prime functions:

$$\mathcal{M}(\zeta) = \prod_{j=1}^{N} \frac{\omega(\zeta, a_j)}{\omega(\zeta, b_j)}. \tag{2.17}$$

Here, $\{a_j \in \mathbb{C} \mid j = 1, ..., N\}$ are the zeroes of $\mathcal{M}(\zeta)$ and $\{b_j \in \mathbb{C} \mid j = 1, ..., N\}$ are the poles of $\mathcal{M}(\zeta)$. Cartoon illustrations of how to construct higher genus compact Riemann surfaces from their fundamental regions are presented in Mumford, Series & Wright [83].

The Schottky-Klein prime function can be shown to satisfy several functional relations; we present three important examples of these here, valid for all $\zeta, \gamma \in F$. It can be shown from the infinite product (2.3) that

$$\omega(\zeta, \gamma) = -\omega(\gamma, \zeta). \tag{2.18}$$

Crowdy & Marshall [28] established that, for the particular class of Schottky-Klein prime functions associated with multiply connected planar domains as relevant for our purposes, the relation

$$\overline{\omega}(\zeta^{-1}, \gamma^{-1}) = -\frac{1}{\zeta\gamma}\omega(\zeta, \gamma) \tag{2.19}$$

holds. From (2.11) and (2.12), it is clear that another relation is

$$\frac{\omega(\theta_j(\zeta), \gamma_1)}{\omega(\theta_j(\zeta), \gamma_2)} = \beta_j(\gamma_1, \gamma_2)\frac{\omega(\zeta, \gamma_1)}{\omega(\zeta, \gamma_2)}, \tag{2.20}$$

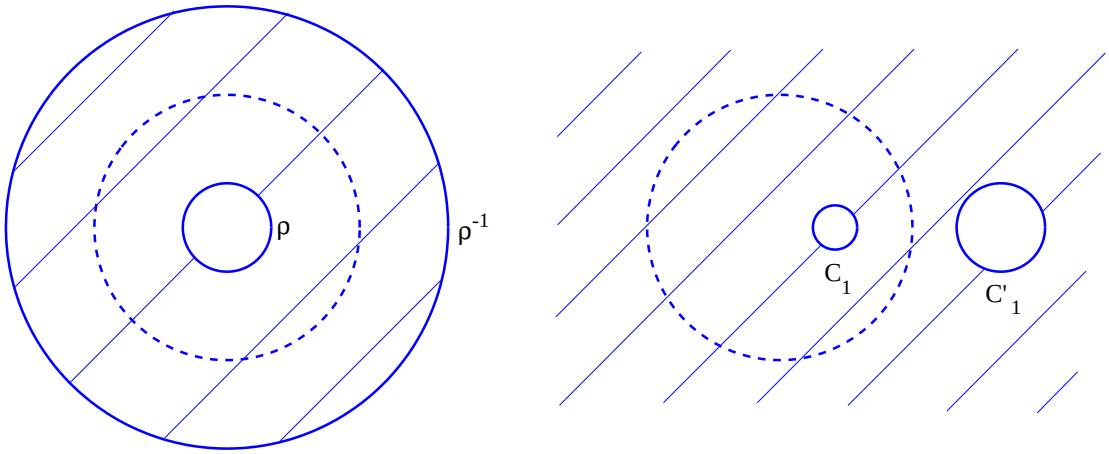


Figure 2.3: The fundamental region associated with a concentric annulus is another concentric annulus (left). The fundamental region associated with an eccentric annulus is an unbounded doubly connected circular domain (right). The fundamental regions are indicated by lines.

where

$$\beta_j(\gamma_1,\gamma_2) = \exp\left(2\pi \mathrm{i}\left(v_j(\gamma_1) - v_j(\gamma_2)\right)\right). \tag{2.21}$$

## 2.2 The Schottky-Klein prime function for doubly connected circular domains

In the case of doubly connected circular domains, the Schottky-Klein prime function can either be defined over a concentric annulus or an eccentric annulus. Note that the fundamental regions associated with these two types of doubly connected circular domain are very different. For the concentric annulus $\rho < |\zeta| < 1$, the fundamental region is another concentric annulus: $\rho \leq |\zeta| < \rho^{-1}$ (say). For the eccentric annulus, the fundamental region is an unbounded doubly connected domain with two circular boundaries. Figure 2.3 shows schematics of these two different types of fundamental region.

Let us first consider the Schottky-Klein prime function defined over a concentric annulus.

The Schottky-Klein prime function associated with $\rho < |\zeta| < 1$ is

$$\omega(\zeta, \gamma) = -\frac{\gamma}{C^2} P(\zeta/\gamma, \rho) \tag{2.22}$$

where we define the special function

$$P(\zeta, \rho) = (1-\zeta) \prod_{j=1}^{\infty} (1-\rho^{2j}\zeta)(1-\rho^{2j}\zeta^{-1}), \tag{2.23}$$

and the constant $C$ is given by

$$C = \prod_{j=1}^{\infty} (1-\rho^{2j}). \tag{2.24}$$

(2.22) follows directly from the infinite product (2.3) owing to the fact that the Schottky group associated with $\rho < |\zeta| < 1$ is $\Theta = \{\rho^{2j}\zeta \mid j \in \mathbb{Z}\}$. Function $P(\zeta, \rho)$ is analytic everywhere in $\rho < |\zeta| < 1$ and has simple zeroes at the points $\{\rho^{2j} \mid j \in \mathbb{Z}\}$. Function $P(\zeta, \rho)$ turns out to be related to the first Jacobi theta function (Marshall [74]).

There is one integral of the first kind associated with the concentric annulus $\rho < |\zeta| < 1$. It is

$$v_1(\zeta) = \frac{1}{2\pi \mathrm{i}} \log \zeta. \tag{2.25}$$

Let us verify that $v_1(\zeta)$ in (2.25) satisfies the defining properties (2.6)-(2.9). It is obvious that on $|\zeta| = 1$,

$$\mathrm{Im}[v_1(\zeta)] = 0, \tag{2.26}$$

and that on $|\zeta| = \rho$,

$$\mathrm{Im}[v_1(\zeta)] = -\frac{1}{2\pi} \log \rho. \tag{2.27}$$

It is also obvious that

$$\frac{1}{2\pi \mathrm{i}} \oint_{|\zeta|=\rho} d[\log \zeta] = 1. \tag{2.28}$$

For $\rho < |\zeta| < 1$, we have from (2.4) that

$$\theta_1(\zeta) = \rho^2 \zeta, \tag{2.29}$$

and so from (2.6), we obtain

$$\tau_{11} = v_1(\theta_1(\zeta)) - v_1(\zeta) = v_1(\rho^2\zeta) - v_1(\zeta) = \frac{1}{2\pi \mathrm{i}} \log(\rho^2\zeta) - \frac{1}{2\pi \mathrm{i}} \log \zeta = \frac{1}{\pi \mathrm{i}} \log \rho. \tag{2.30}$$

The function $P(\zeta,\rho)$ satisfies the following two functional relations:

$$P(\zeta^{-1},\rho)=-\zeta^{-1}P(\zeta,\rho),\quad P(\rho^2\zeta,\rho)=-\zeta^{-1}P(\zeta,\rho). \tag{2.31}$$

The first of these relations follows immediately from (2.23) and can also be derived from the identity (2.19). Define the Schwarz conjugate $\overline{f}(\zeta)$ of a given function $f(\zeta)$ to be

$$\overline{f}(\zeta)=\overline{f(\overline{\zeta})}. \tag{2.32}$$

We have

$$\overline{\omega}(\zeta^{-1},\gamma^{-1})=-\frac{1}{\gamma C^2}P(\gamma\zeta^{-1},\rho) \tag{2.33}$$

and

$$-\frac{1}{\zeta\gamma}\omega(\zeta,\gamma)=\frac{1}{\zeta C^2}P(\zeta\gamma^{-1},\rho). \tag{2.34}$$

Equating (2.33) and (2.34) implies

$$P(\gamma\zeta^{-1},\rho)=-\frac{\gamma}{\zeta}P(\zeta\gamma^{-1},\rho). \tag{2.35}$$

We recover the first relation in (2.31) upon setting $\gamma=1$ in (2.35). To show the second of the relations in (2.31), note that

$$P(\rho^2\zeta,\rho)=(1-\rho^2\zeta)(1-\zeta^{-1})\prod_{j=1}^{\infty}(1-\rho^{2j+2}\zeta)(1-\rho^{2j}\zeta^{-1})$$

$$=-\zeta^{-1}(1-\zeta)\prod_{j=1}^{\infty}(1-\rho^{2j}\zeta)(1-\rho^{2j}\zeta^{-1})=-\zeta^{-1}P(\zeta,\rho). \tag{2.36}$$

Alternatively, note that

$$\omega(\theta_1(\zeta),\gamma)=-\frac{\gamma}{C^2}P(\rho^2\zeta/\gamma,\rho). \tag{2.37}$$

Using (2.25) and (2.30), we obtain

$$\exp\left(-2\pi\mathrm{i}v_1(\zeta)+2\pi\mathrm{i}v_1(\gamma)-\pi\mathrm{i}\tau_{11}\right)\left(\frac{d\theta_1(\zeta)}{d\zeta}\right)^{1/2}\omega(\zeta,\gamma)=\frac{\gamma^2}{\zeta C^2}P(\zeta/\gamma,\rho), \tag{2.38}$$

where the negative branch of the square root has been taken. Thus, using (2.37) and (2.38) in (2.11), we obtain

$$P(\rho^2\zeta/\gamma,\rho)=-\frac{\gamma}{\zeta}P(\zeta/\gamma,\rho). \tag{2.39}$$

We recover the second relation in (2.31) upon setting $\gamma = 1$ in (2.39). It also follows immediately from (2.39), on taking a ratio, that

$$\frac{P(\rho^2\zeta/\gamma_1,\rho)}{P(\rho^2\zeta/\gamma_2,\rho)} = \frac{\gamma_1}{\gamma_2}\frac{P(\zeta/\gamma_1,\rho)}{P(\zeta/\gamma_2,\rho)}, \tag{2.40}$$

which recovers the relation (2.20). Finally, note that the relation (2.18) can easily be verified using the first relation in (2.31):

$$\omega(\gamma,\zeta) = -\frac{\zeta}{C^2}P(\gamma/\zeta,\rho) = \frac{\gamma}{C^2}P(\zeta/\gamma,\rho) = -\omega(\zeta,\gamma). \tag{2.41}$$

Using $P(\zeta,\rho)$, it is possible to define another special function:

$$K(\zeta,\rho) = \zeta\frac{P'(\zeta,\rho)}{P(\zeta,\rho)}. \tag{2.42}$$

Here, $P'(\zeta,\rho)$ means differentiation of $P(\zeta,\rho)$ with respect to the first argument. The function $K(\zeta,\rho)$ satisfies the following two functional relations:

$$K(\zeta^{-1},\rho) = 1 - K(\zeta,\rho), \quad K(\rho^2\zeta,\rho) = K(\zeta,\rho) - 1. \tag{2.43}$$

These are easily derived from (2.31). Indeed, taking logarithmic derivatives on the first relation in (2.31) yields

$$-\frac{1}{\zeta^2}\frac{P'(\zeta^{-1},\rho)}{P(\zeta^{-1},\rho)} \equiv -\frac{1}{\zeta}K(\zeta^{-1},\rho) = -\frac{1}{\zeta} + \frac{P'(\zeta,\rho)}{P(\zeta,\rho)} \tag{2.44}$$

which, after multiplication by $-\zeta$, recovers the first relation in (2.43). The second relation in (2.43) can be derived in a similar fashion.

Let us now consider the Schottky-Klein prime function defined over an eccentric annulus. Consider the eccentric annular region, in a parametric $\hat{\zeta}$-plane, defined to be intersection of the interior of $|\hat{\zeta}| = 1$ and the exterior of $|\hat{\zeta} - \delta| = q$ (where, without loss of generality, we choose $\delta \in \mathbb{R}$). Call this eccentric annulus $\hat{D}_\zeta$.

An interesting question to pose is: what is the integral of the first kind $\hat{v}_1(\hat{\zeta})$ associated with the eccentric annular region $\hat{D}_\zeta$? Let us map the eccentric annulus $\hat{D}_\zeta$ to the concentric annulus $\rho < |\zeta| < 1$, where $\rho$ will need to be determined. Introduce a special Möbius

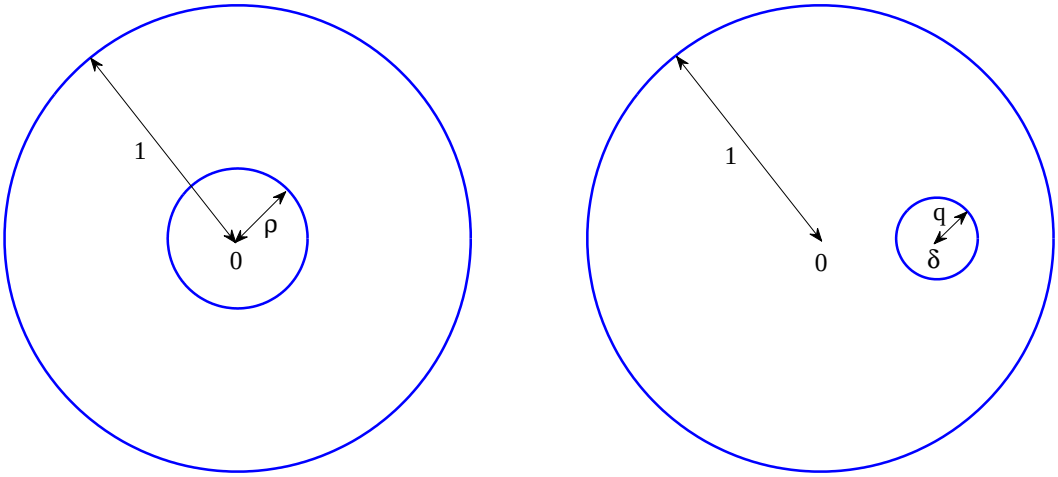


Figure 2.4: The eccentric annulus (right) is mapped to the concentric annulus (left) by the automorphism defined in (2.45).

mapping known as an automorphism of the unit disc:

$$\eta(\hat{\zeta};\alpha) = \frac{\hat{\zeta}-\alpha}{|\alpha|(\hat{\zeta}-1/\alpha)}, \tag{2.45}$$

where $\alpha \in \mathbb{R}$. The image of $|\hat{\zeta}| = 1$ under $\eta(\hat{\zeta};\alpha)$ is $|\eta| = 1$ and the image of $|\hat{\zeta}-\delta| = q$ under $\eta(\hat{\zeta};\alpha)$ is $|\eta| = \rho$, where

$$\rho = \frac{1-\delta^2+q^2-((1-\delta^2+q^2)^2-4q^2)^{1/2}}{2q}, \quad \alpha = \left(\frac{\rho-q}{\rho(1-q\rho)}\right)^{1/2}, \tag{2.46}$$

(Crowdy [private communication]). See Figure 2.4. In (2.46), the positive branches of the square roots are chosen.

We claim that the integral of the first kind associated with the eccentric annular region $\hat{D}_\zeta$ is

$$\hat{v}_1(\hat{\zeta}) = v_1(\eta(\hat{\zeta};\alpha)), \tag{2.47}$$

where $v_1(\zeta)$ is the integral of the first kind associated with the concentric annular region

$\rho < |\zeta| < 1$ as given in (2.25), and $\eta(\hat{\zeta};\alpha)$ is the automorphism in (2.45). Thus

$$\hat{v}_1(\hat{\zeta}) = \frac{1}{2\pi \mathrm{i}} \log\left(\frac{\hat{\zeta}-\alpha}{|\alpha|(\hat{\zeta}-1/\alpha)}\right), \tag{2.48}$$

where $\alpha \in \mathbb{R}$ is given in (2.46). It should be noted that $\alpha$ always lies in the interior of $|\hat{\zeta}-\delta| = q$. This function is analytic but not single-valued everywhere in $\hat{D}_\zeta$. It is straightforward to demonstrate that the necessary properties required of an integral of the first kind are satisfied by function $\hat{v}_1(\hat{\zeta})$ given in (2.48) over $\hat{D}_\zeta$; that is, these necessary properties are conformally invariant under the automorphism (2.45), and hence $\hat{v}_1(\hat{\zeta})$ is related to $v_1(\zeta)$ through the relation (2.47).

It is shown in Baker [6] that the $M$ integrals of the first kind have an infinite product representation:

$$v_j(\zeta) = \frac{1}{2\pi \mathrm{i}} \log\left(\prod_{\theta\in\Theta_k} \frac{\zeta-\theta(B_k)}{\zeta-\theta(A_k)}\right) + \mathrm{i}c_j. \tag{2.49}$$

Here, $c_j \in \mathbb{R}$ are constants chosen so that (2.26) is satisfied, $A_k$ and $B_k$ are the fixed points of $\theta_k(\zeta)$ (with $|A_k| > 1$ and $|B_k| < 1$), and $\Theta_k \subset \Theta$ is a special subgroup of $\Theta$ consisting of all members of $\Theta$ but excluding the compositions ending in $\theta_k$ and $\theta_k^{-1}$; that is, $\theta_1(\theta_2^{-1}(\zeta))$ is contained in $\Theta_3$ but $\theta_1(\theta_3^{-1}(\zeta))$ and $\theta_2^{-1}(\theta_3(\zeta))$ are not. Thus, for all doubly connected circular domains, the only member of $\Theta_1$ is the identity element. Hence, for the eccentric annulus $\hat{D}_\zeta$, (2.49) reduces to

$$\frac{1}{2\pi \mathrm{i}} \log\left(\frac{\zeta-B_1}{\zeta-A_1}\right). \tag{2.50}$$

Here, $A_1$ and $B_1$ are the two solutions of the equation

$$\theta_1(\zeta) = \zeta, \tag{2.51}$$

where, for the eccentric annulus $\hat{D}_\zeta$, we have from (2.4) that

$$\theta_1(\zeta) = \delta + \frac{q^2\zeta}{1-\delta\zeta}. \tag{2.52}$$

After lengthy algebraic manipulations (which we neglect for brevity), it can be verified that (2.50) is indeed equivalent to (2.48).

## 2.3 Conformal slit mappings

We will now introduce some important 'building block' functions which will be used throughout the thesis. These building block functions are in fact classes of conformal mappings to multiply connected slit domains. These special functions are building block functions in the following sense: they facilitate incorporating a desired structure of zeroes and poles into the definition of a particular function whilst maintaining properties such as constant modulus or constant argument on each of the boundary circles. In this thesis, we will give evidence that conformal slit mappings are natural candidate functions to consider when dealing with multiple boundary conditions in free boundary problems. The review article of Crowdy [24] elucidates the central role of the conformal slit mappings when solving certain applied mathematical problems set in multiply connected geometries. It is also worth noting here that DeLillo & Kropf [39] and DeLillo et al [40] have formulated numerically efficient infinite product representations for conformal mappings to multiply connected slit domains; however, we advocate using the Schottky-Klein prime function owing to the fact that the functional forms of the maps are mathematically elegant when written in terms of this function, and their defining properties can be both understood and demonstrated in a straightforward manner by using aspects of the function theory presented in this chapter.

Introduce the bounded circular slit mapping (Crowdy & Marshall [29]):

$$\eta(\zeta;\gamma) = \frac{\omega(\zeta,\gamma)}{|\gamma|\omega(\zeta,1/\overline{\gamma})}. \tag{2.53}$$

Here, $\zeta = \gamma$ is an arbitrary point in the interior of $D_\zeta$. Function $\eta(\zeta;\gamma)$ has constant modulus on all the boundary circles $C_0, C_1, ..., C_M$. It has a simple zero at $\zeta = \gamma$ and a simple pole at $\zeta = 1/\overline{\gamma}$. Under the map $\eta(\zeta;\gamma)$, $C_0$ is mapped to the unit $\eta$-circle while $C_1, ..., C_M$ are mapped onto finite-length concentric circular arcs lying in the interior of $|\eta| = 1$. Figure 2.5 shows the image under $\eta(\zeta;\gamma)$ of some quadruply connected circular domain $D_\zeta$. Note that when $\omega(\zeta,\gamma) = \zeta - \gamma$, the map $\eta(\zeta;\gamma)$ in (2.53) reduces to an automorphism of the unit disc (recall (2.45)).

To illustrate the usefulness of the functional relations (2.19) and (2.20), let us now prove

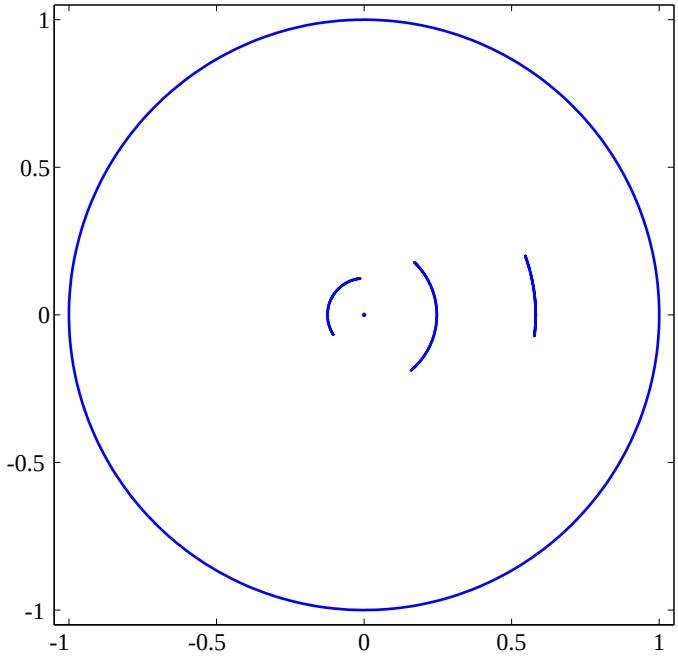


Figure 2.5: Image of $D_\zeta$ with the conformal moduli $\delta_1 = 0$, $q_1 = 0.1$, $\delta_2 = 0.3 + 0.1\mathrm{i}$, $q_2 = 0.05$, $\delta_3 = -0.35 - 0.275\mathrm{i}$, $q_3 = 0.08$ under the bounded circular slit map $\eta(\zeta; 0.2 + 0.1\mathrm{i})$ of (2.53). The origin is indicated by a dot.

explicitly that $|\eta(\zeta;\gamma)| =$ constant for $\zeta \in C_0, C_1, ..., C_M$. Consider $\zeta \in C_0$. Then

$$\overline{\zeta} = \zeta^{-1}. \tag{2.54}$$

Taking the complex conjugate of (2.53) and using (2.19) reveals:

$$\overline{\eta(\zeta;\gamma)} = \frac{\overline{\omega}(\zeta^{-1},\overline{\gamma})}{|\gamma|\overline{\omega}(\zeta^{-1},\gamma^{-1})} = \frac{|\gamma|\omega(\zeta,\gamma^{-1})}{\omega(\zeta,\gamma)} = \frac{1}{\eta(\zeta;\gamma)}. \tag{2.55}$$

Thus

$$|\eta(\zeta;\gamma)| = 1, \quad \zeta \in C_0. \tag{2.56}$$

Now consider $\zeta \in C_j$, $j = 1, ..., M$. Note that

$$\overline{\zeta} = \overline{\theta_j}(\zeta^{-1}). \tag{2.57}$$

Taking the complex conjugate of (2.53), and using (2.20) followed by (2.19), reveals:

$$\overline{\eta(\zeta;\gamma)} = \frac{\overline{\omega}(\overline{\theta_j}(\zeta^{-1}),\overline{\gamma})}{|\gamma|\overline{\omega}(\overline{\theta_j}(\zeta^{-1}),\gamma^{-1})} = \overline{\beta_j(\gamma, 1/\overline{\gamma})}\frac{\overline{\omega}(\zeta^{-1},\overline{\gamma})}{|\gamma|\overline{\omega}(\zeta^{-1},\gamma^{-1})} = \frac{\overline{\beta_j(\gamma, 1/\overline{\gamma})}}{\eta(\zeta;\gamma)}. \tag{2.58}$$

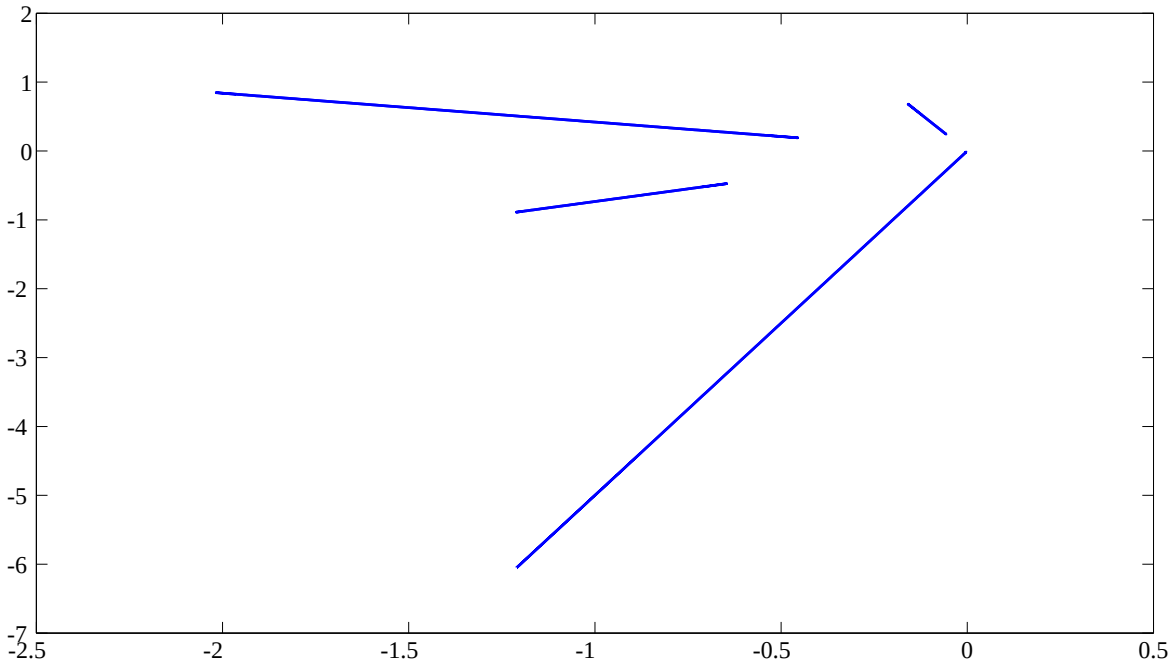


Figure 2.6: Image of $D_\zeta$ with the conformal moduli $\delta_1 = 0$, $q_1 = 0.1$, $\delta_2 = 0.3 + 0.1\mathrm{i}$, $q_2 = 0.05$, $\delta_3 = -0.35 - 0.275\mathrm{i}$, $q_3 = 0.08$ under the radial slit map $\chi(\zeta; 0.8, -0.1 + 0.5\mathrm{i})$ of (2.60).

Thus

$$|\eta(\zeta;\gamma)| = \left(\overline{\beta_j\left(\gamma, 1/\overline{\gamma}\right)}\right)^{1/2} = \text{constant}, \quad \zeta \in C_j, \quad j = 1, ..., M. \tag{2.59}$$

Let us now introduce the radial slit mapping (Crowdy & Marshall [29]):

$$\chi(\zeta;\zeta_1,\zeta_2) = \frac{\omega(\zeta,\zeta_1)\omega(\zeta,1/\overline{\zeta_1})}{\omega(\zeta,\zeta_2)\omega(\zeta,1/\overline{\zeta_2})}. \tag{2.60}$$

Here, $\zeta = \zeta_1$ and $\zeta = \zeta_2$ are any two distinct points in the closure of $D_\zeta$. Function $\chi(\zeta;\zeta_1,\zeta_2)$ has constant argument on each of the $M+1$ boundary circles $C_0, C_1, ..., C_M$ of $D_\zeta$. This can be proved by showing that

$$\frac{\chi(\zeta;\zeta_1,\zeta_2)}{\overline{\chi(\zeta;\zeta_1,\zeta_2)}} = \text{constant}, \quad \zeta \in C_0, C_1, ..., C_M, \tag{2.61}$$

using the functional relations (2.19) and (2.20). Function $\chi(\zeta;\zeta_1,\zeta_2)$ has a simple zero at $\zeta = \zeta_1$ and a simple pole at $\zeta = \zeta_2$. Function $\chi(\zeta;\zeta_1,\zeta_2)$ maps each of the boundary

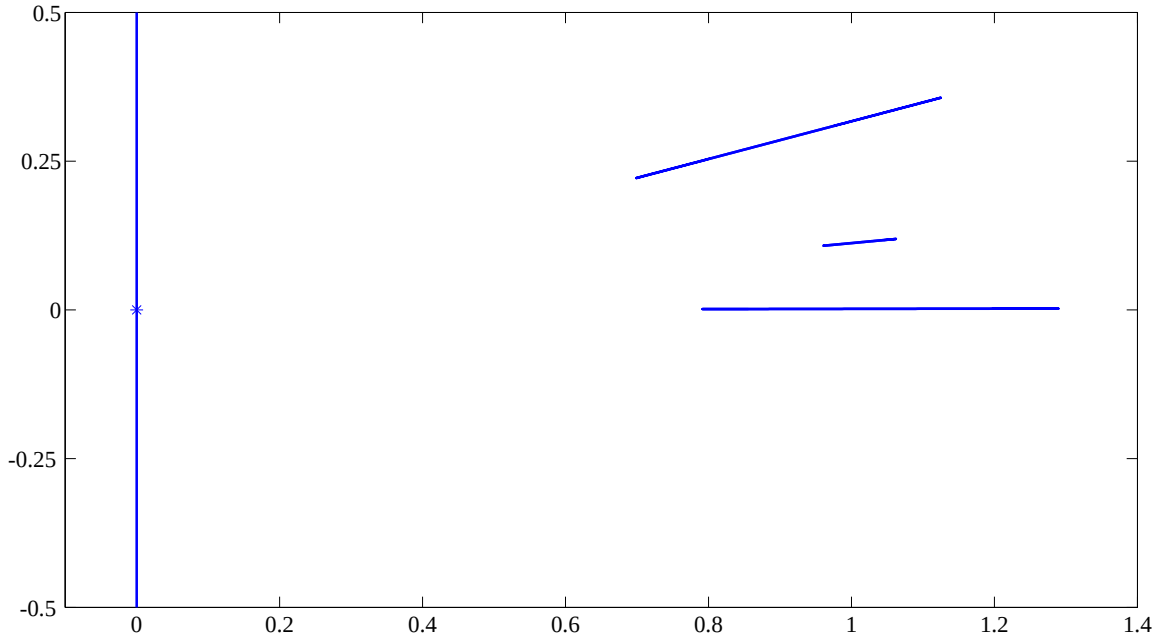


Figure 2.7: Image of $D_\zeta$ with the conformal moduli $\delta_1 = 0$, $q_1 = 0.1$, $\delta_2 = 0.3 + 0.1\mathrm{i}$, $q_2 = 0.05$, $\delta_3 = -0.35 - 0.275\mathrm{i}$, $q_3 = 0.08$ under the radial slit map $\xi(\zeta; \delta_2 + q_2 \mathrm{e}^{2\pi\mathrm{i}/3}, \delta_2 + q_2 \mathrm{e}^{5\pi\mathrm{i}/3})$ of (2.62). The origin is indicated by a star.

circles in the $\zeta$-plane onto finite-length slits emanating from origin in the $\chi$-plane. Figure 2.6 shows the image under $\chi(\zeta; \zeta_1; \zeta_2)$ of some quadruply connected circular domain $D_\zeta$.

Crowdy [13] showed that, for any two distinct points $\zeta = \zeta_3$ and $\zeta = \zeta_4$ lying on one of the boundary circles $C_j$, $j = 0, 1, ..., M$, function

$$\xi(\zeta; \zeta_3, \zeta_4) = \frac{\omega(\zeta, \zeta_3)}{\omega(\zeta, \zeta_4)} \tag{2.62}$$

has constant argument on each of the boundary circles $C_0, C_1, ..., C_M$. Function $\xi(\zeta; \zeta_3, \zeta_4)$ has a simple zero at $\zeta = \zeta_3$ and a simple pole at $\zeta = \zeta_4$. Function $\xi(\zeta; \zeta_3, \zeta_4)$ is a particular type of radial slit mapping: it maps $C_1, ..., C_{j-1}, C_{j+1}, ..., C_M$ onto finite-length slits emanating from the origin in the $\xi$-plane and $C_j$ onto an infinite line through $\xi = 0$. Figure 2.7 shows the image under $\xi(\zeta; \zeta_3; \zeta_4)$ of some quadruply connected circular domain $D_\zeta$.

For further detail on the aforementioned conformal slit mappings, the reader is referred to Crowdy & Marshall [29]. There are three other types of conformal slit mappings which will not feature in this thesis: namely, the unbounded circular slit map, the parallel slit map, and the map to an annular region with concentric circular slits. For further detail on

these, the reader is again directed to [29].

## 2.4 Computing the Schottky-Klein prime function

To conclude this chapter, we will present details of a numerical method we have devised to compute the Schottky-Klein prime function. The infinite product (2.3) is a numerically inefficient mathematical object to compute and it is not always convergent for some choices of bounded multiply connected circular domain. However, the Schottky-Klein prime function itself is a well-defined function over *any* bounded multiply connected circular domain. It is therefore important to have at hand a reliable, accurate and fast numerical scheme to compute the Schottky-Klein prime function if it is to be employed in applications.

Our numerical scheme improves on the numerical scheme presented by Crowdy & Marshall [31]. Crowdy & Marshall [31] formulated their method around the four defining properties of the square of the Schottky-Klein prime function $X(\zeta,\gamma)$ presented by Hejhal [59] and used a method of least squares to solve for the coefficients in a Fourier-Laurent series representation of $X(\zeta,\gamma)$. Our method also seeks the coefficients in a Fourier-Laurent series representation of $X(\zeta,\gamma)$ and is centred around the four defining properties of $X(\zeta,\gamma)$ from Hejhal [59]; the main difference is that our numerical scheme proceeds using a method called 'successive iteration' (explained in due course) and adopts the fast Fourier transform. One main advantage of our numerical scheme is that any level of truncation in the Fourier-Laurent series may be chosen; with a least squares method, there is an optimum level of truncation so that minimal numerical error is induced. There are two main steps to our method, and these are the same as in Crowdy & Marshall [31]: firstly, the computation of the integrals of the first kind $v_j(\zeta)$, and secondly, the computation of $X(\zeta,\gamma)$.

### 2.4.1 Computation of the $v_j(\zeta)$ functions

Consider the following ansatz:

$$v_j(\zeta) = \frac{1}{2\pi \mathrm{i}}\log(\zeta-\delta_j) + \sum_{k=0}^{\infty} a_k^{(j)}\zeta^k + \sum_{p=1}^{M}\sum_{k=1}^{\infty}\frac{b_k^{(j,p)}q_p^k}{(\zeta-\delta_p)^k}, \quad j=1,...,M. \tag{2.63}$$

Observe that this representation (2.63) is analytic everywhere in $D_\zeta$ i.e. analytic in one 'half' of $F$. However, we can exploit analytic continuation across $C_0$ to evaluate each

$v_j(\zeta)$ at points on the other 'half' of $F$, if required (recall (2.8)):

$$v_j(\zeta) = \overline{v_j}(\zeta^{-1}), \quad j = 1, ..., M. \tag{2.64}$$

Each $v_j(\zeta)$, $j = 1, ..., M$, must satisfy the conditions (2.8) and (2.9). The constants $\gamma_{jk} \in \mathbb{R}$ in (2.9) are not known *a priori* and must be solved for as part of the solution.

The numerical procedure can be outlined by the following three steps:

1. Truncate (2.63) at $\mathcal{O}(N)$. Take $4N$ equi-spaced collocation points around each $\{C_j\}_{j=0}^{M}$ (allowing for 'padding').

2. On each $\{C_j\}_{j=0}^{M}$, enforce the conditions (2.8) and (2.9) and determine the set of constants $\{\gamma_{jk}\}$.

3. Use the fast Fourier transform on each $\{C_j\}_{j=0}^{M}$ to solve for the coefficients $\{a_k^{(j)}, b_k^{(j,p)}\}$ by a method known as successive iteration.

Let us now outline what we mean by 'successive iteration'. We initially make suitable initial guesses of the coefficients $\{a_k^{(j)}, b_k^{(j,p)}\}$ (we find it is sufficient to take them all as zero) so that $v_j(\zeta)$ is a fully determined function. Upon substitution of ansatz (2.63) into the boundary conditions (2.8) and (2.9), we use fast Fourier transforms on each of the circles $\{C_j\}_{j=0}^{M}$ to determine a set of 'improved' values of the coefficients. We use these up-dated values of the coefficients as initial guesses in the next iteration. The iterations continue to be performed until a desired level of accuracy is attained and convergence can be considered to have been achieved. It should be noted that Wegmann [122] solves a special type of Riemann-Hilbert problem using similar ideas.

### 2.4.2 Computation of $X(\zeta, \gamma)$

To find a representation for $X(\zeta, \gamma)$, we need a Fourier-Laurent expansion which is analytic and single-valued everywhere in the fundamental region $F$. Write

$$X(\zeta, \gamma) = (\zeta - \gamma)^2 \hat{X}(\zeta, \gamma) \tag{2.65}$$

and let

$$\hat{X}(\zeta, \gamma) = \mathcal{A}\left(1 + \sum_{j=1}^{M}\sum_{k=1}^{\infty} \frac{b_k^{(j)} q_j^k}{(\zeta - \delta_j)^k} + \sum_{j=1}^{M}\sum_{k=1}^{\infty} \frac{c_k^{(j)} q_j'^k}{(\zeta - \delta_j')^k}\right) \tag{2.66}$$

where $\mathcal{A} \in \mathbb{C}$ is a constant to be determined.

The numerical procedure can be outlined as follows:

1. Truncate (2.66) at $\mathcal{O}(N)$ (and ignore complex constant $\mathcal{A}$ for the moment). Take $4N$ equi-spaced collocation points on each of the $2M$ circles $\{C_j, C'_j\}_{j=1}^M$ (allowing for 'padding').

2. On each $\{C'_j\}_{j=1}^M$, enforce the condition

$$\hat{X}(\theta_j(\zeta), \gamma) = R_j(\zeta, \gamma)\hat{X}(\zeta, \gamma) \tag{2.67}$$

   where we have defined function

$$R_j(\zeta, \gamma) = \exp(-4\pi \mathrm{i} v_j(\zeta) + 4\pi \mathrm{i} v_j(\gamma) - 2\pi \mathrm{i} \tau_{jj}) \left( \frac{\zeta - \gamma}{\theta_j(\zeta) - \gamma} \right)^2 \frac{d\theta_j(\zeta)}{d\zeta}. \tag{2.68}$$

3. On each $\{C_j\}_{j=1}^M$, enforce the condition

$$\hat{X}(\zeta, \gamma) = R_j(\theta_j^{-1}(\zeta), \gamma)\hat{X}(\theta_j^{-1}(\zeta), \gamma). \tag{2.69}$$

4. Use the fast Fourier transform on each $\{C_j, C'_j\}_{j=1}^M$ to solve for the coefficients $\{b_k^{(j)}, c_k^{(j)}\}$ via successive iteration.

5. Finally, enforce the normalisation

$$\hat{X}(\gamma, \gamma) = 1 \tag{2.70}$$

   to determine the complex constant $\mathcal{A}$.

For some choice of circular domain $D_\zeta$, the square of the Schottky-Klein prime function can now readily be computed. We should now think of the Schottky-Klein prime function as a special but perfectly computable function (like trigonometric functions, Bessel functions etc).

### 2.4.3 Special classes of circular pre-image domain $D_\zeta$

As it stands, our numerical scheme will fail for domains when either one of the $\delta_j = 0$, or when one of the $q_j = |\delta_j|$. We discuss the required modifications below.

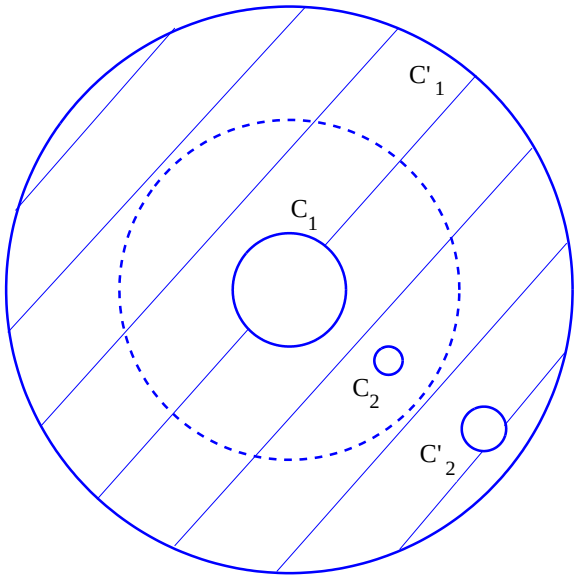


Figure 2.8: Schematic of the fundamental region (shown by lines) associated with a bounded triply connected circular domain with an interior circle $C_1$ which is centred at the origin. The unit circle is shown by a dashed line.

### The case $\delta_j = 0$

Consider a circular domain $D_\zeta$ with one interior circle $C_1$ of radius $q_1$ such that $\delta_1 = 0$. See Figure 2.8 for a schematic of the fundamental region in this case. For these circular domains, let

$$\hat{X}(\zeta,\gamma) = \mathcal{A}\left(1 + \sum_{k=1}^{\infty}\frac{a_k q_1^k}{\zeta^k} + \sum_{k=0}^{\infty} b_k q_1^k \zeta^k + \sum_{j=2}^{M}\sum_{k=1}^{\infty}\frac{c^{(j,k)}q_j^k}{(\zeta-\delta_j)^k} + \sum_{j=2}^{M}\sum_{k=1}^{\infty}\frac{d^{(j,k)}q_j'^k}{(\zeta-\delta_j')^k}\right). \tag{2.71}$$

### The case $q_j = |\delta_j|$

Consider a circular domain $D_\zeta$ with an interior circle $C_1$ such that $q_1 = |\delta_1|$. Note that the reflection of $C_1$ in the unit disc is an infinite straight line. See Figure 2.9 for a schematic of the fundamental region in this case. This explains why our previous Fourier-Laurent expansion (2.66) is now rendered inappropriate for this class of circular domain. For these

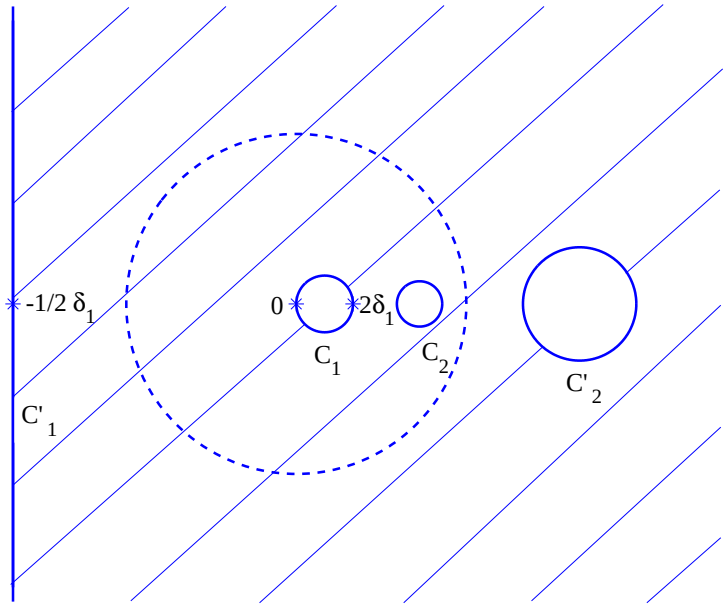


Figure 2.9: Schematic of the fundamental region (shown by lines) associated with a bounded triply connected circular domain with an interior circle $C_1$ such that $|\delta_1| = q_1$, i.e. the magnitude of the centre $\delta_1$ is equal to the radius $q_1$. The unit circle is shown by a dashed line.

circular domains, let

$$\hat{X}(\zeta,\gamma) = \mathcal{A}\left(1 + \sum_{k=1}^{\infty} \frac{a_k \rho^k}{(\eta(\zeta))^k} + \sum_{k=0}^{\infty} b_k (\eta(\zeta))^k + \sum_{j=2}^{M}\sum_{k=1}^{\infty} \frac{c^{(j,k)} q_j^k}{(\zeta-\delta_j)^k} + \sum_{j=2}^{M}\sum_{k=1}^{\infty} \frac{d^{(j,k)} q_j'^k}{(\zeta-\delta_j')^k}\right) \tag{2.72}$$

where $\eta(\zeta)$ is a Möbius map (we neglect details for brevity).

### 2.4.4 The case when $\gamma$ lies on a boundary circle

The way in which function $R_j(\zeta,\gamma)$ in (2.68) is defined leads to a potential problem: namely, when $\omega(\zeta,\gamma)$ is such that $\gamma$ lies on one of the boundary circles $\{C_j, C_j'\}_{j=1}^M$. This is because there could be a collocation point, $\zeta^* \in C_j'$ (say), such that $\theta_j(\zeta^*) = \gamma$ and the denominator of boundary condition (2.67) vanishes. Similarly, there could be a $\tilde{\zeta} \in C_j$ such that $\tilde{\zeta} = \gamma$, leading to the denominator of boundary condition (2.69) vanishing. We were able to devise a resolution to this problem, but we will not present these modifications here for brevity (it is similar to the foregoing analysis).

# Chapter 3

# Von Kármán streets of hollow vortices

## 3.1 Introduction

In this chapter, we shall examine the fascinating and well-studied phenomena of vortex rows and vortex streets. By a vortex row, we mean an infinite array of equally separated vortices of equal circulation. By a vortex street, we mean two parallel vortex rows of equal and opposite circulation. The vortex street usually goes by the name of a von Kármán vortex street owing to the fact that von Kármán pioneered the first theoretical studies into them by using point vortices (see von Kármán [120] and von Kármán & Rubach [121]). Unfortunately, using point vortices to model vortex streets is a somewhat approximate approach and presents several limitations: there is an infinite kinetic energy associated with the structure, and it is difficult to fit the model to flow past a body. Thus, to offer a more realistic physical interpretation, we have chosen to model these structures using the distributed vorticity model of the hollow vortex. Recall that a hollow vortex is a finite-area vacuum at constant pressure whose free boundary is a vortex sheet of constant strength. The free boundary problems we shall solve in this chapter will consist of determining the shapes of the hollow vortex boundaries in these structures.

We shall first develop a new mathematical approach to model a single row of hollow vortices in unbounded fluid. This configuration has already been studied by Baker, Saffman & Sheffield [7] and they were able to find an exact solution for the shape of a typical hollow vortex member of the row by appealing to symmetry and by the application of Schwarz-Christoffel methods. We will present an equivalent exact solution describing this free boundary but with a different (and arguably more concise) mathematical form. Although this free boundary problem for the single row has already been solved, our pre-

liminary study into establishing a different mathematical approach will pave the way to finding analytical solutions for a von Kármán street of hollow vortices. We shall show how to construct a concise formula for the conformal mapping determining the relative equilibrium shapes of the hollow vortices in both staggered and unstaggered street configurations. Central to the solutions of both free boundary problems in this chapter will be the use of conformal circular slit mappings.

Both the hollow vortex row and the hollow vortex street are periodic structures: a regular pattern of hollow vortices which replicates itself to infinity. Their intrinsic periodicity immediately implies that the original free boundary problem over free space can be reformulated over a simpler, 'reduced' domain. For us, these simplified domains will take the form of so-called 'period windows' or 'period cells': these are finite-width vertical slices through the structure, extending to infinity, containing either one or two hollow vortices whose boundary shapes will need to be determined. We will incorporate the periodicity into our models by introducing branch cuts in the preimage domains. This is a novel idea but one which nevertheless makes the free boundary problems to be considered analytically tractable. Similar ideas have been employed by Tanveer [110], in simply and doubly connected cases, in relation to the free boundary problem of determining the shapes of inviscid planar finite-amplitude water waves. We will employ this branch cut technique again in Chapter 4.

The fundamental approach of the present chapter (and also the proceeding two chapters) is to exploit ideas from free streamline theory and conformal mapping theory in order to produce analytical solutions to our free boundary problems: knowledge of the complex velocity function $dw/dz$ and the complex potential $W(\zeta)$ will allow us to construct an integral for the conformal map $z(\zeta)$ determining the shapes of the hollow vortex free boundaries:

$$z(\zeta) = \int_{\zeta_0}^{\zeta} \frac{(dW/d\zeta)(\zeta')}{(dw/dz)(\zeta')} d\zeta'. \tag{3.1}$$

In the case of the row of hollow vortices, this integral (3.1) can be evaluated analytically to produce an exact solution for the conformal map. For the von Kármán street of hollow vortices, we obtain an explicit indefinite integral for the conformal map whose integrand is expressed in terms of the Schottky-Klein prime function associated with a concentric annulus, and which can be readily evaluated numerically. The solutions we present in this chapter for the von Kármán street of hollow vortices appear to be the first of their kind.

## 3.2 Background

There is a very wide literature on the subject of von Kármán vortex streets and they arise throughout nature. There are some photographs of typical von Kármán vortex streets in Van Dyke [114]. They are commonly formed in the wakes behind obstacles in uniform flow, as discussed by both Williamson [125] and Saffman [93]; they are also commonly formed in the oceans and in the atmosphere. In the atmosphere, turbulence caused by wind interacting with a land mass produces eddies which swirl clouds into a von Kármán vortex street. Heinze, Raasch & Etling [58] studied von Kármán vortex streets generated in the wake of an idealised island using large eddy simulation, and Chopra & Hubert [11] determined the properties of mesoscale eddies in the wake of islands due to their resemblance with von Kármán vortex streets. Chopra & Hubert [10] have also studied von Kármán vortex streets in the atmosphere of the Earth. Li et al [70] have analysed the sea surface imprint of two atmospheric von Kármán vortex streets observed in satellite imagery. Von Kármán vortex streets have also been studied on curved surfaces. Chamoun, Kanso & Newton [9] identified the complete family of streamline patterns associated with von Kármán point vortex streets on the surface of a non-rotating sphere whilst Alobaidi & Mallier [4] have recently derived some new expressions for vortex streets on a spheroidal surface. Hally [57] has also considered streets of vortices on surfaces of revolution from a more abstract perspective. Vortex streets can now, in principle, be studied on a ring torus using the function theory recently proposed by Green & Marshall [54].

More realistic theoretical models of von Kármán vortex streets have emerged over the years since the initial investigations of von Kármán. Saffman & Schatzman [94] desingularised the point vortex model of a von Kármán street by using finite-area vortex patches. They determined the relative equilibrium shapes of the vortex patches in a steadily translating staggered street configuration, in ideal unbounded fluid, by finding numerical solutions to an integro-differential equation. We shall be making several intriguing connections with the results of Saffman & Schatzman [94] later in this chapter. In a subsequent work, Saffman & Schatzman [96] analysed the stability of their street of vortex patches. Kamm [65] studied a street of vortex patches by using an approach based on Schwarz functions whilst Saffman & Szeto [98] found a one-parameter family of shapes for a linear array of vortex patches by numerically solving an integro-differential equation.

Von Kármán vortex streets continually arise in new applications. Recently, Liao et al [71]

found that rainbow trout interacting with von Kármán streets voluntarily adjust their body kinematics and adopt a pattern of movement to aide their swimming, a phenomenon dubbed the 'Kármán gait'. Such studies into fish schooling were the inspiration for Whittlesey, Liska & Dabiri [124] who have proposed that wind farm efficiency can be enhanced by placing vertical axis turbines in the form of staggered von Kármán vortex streets. Von Kármán vortex streets can also be made to form in the laboratory. Sasaki, Suzuki & Saito [100] investigated vortex shedding from an obstacle potential moving in a Bose-Einstein condensate and discovered a von Kármán vortex street can establish in the wake. Saito, Aioi & Kadokura [99] showed that a von Kármán vortex street can emerge in an exciton-polariton superfluid resonantly injected into a semiconductor microcavity. Shao et al [103] used von Kármán vortex streets with ethanol flowing around a cylinder to deposit tin catalyst in such a way as to grow a pattern of nanoscale silicon disks.

## 3.3 A single row of hollow vortices

Baker, Saffman & Sheffield [7] found analytical expressions describing the shapes of hollow vortices aligned in a single row. They used hodograph plane techniques and exploited symmetry. By a row of hollow vortices, we mean an infinite line of equally separated hollow vortices of equal circulation. In this section, we re-derive the solution of Baker, Saffman & Sheffield [7] using a different and novel mathematical approach.

### 3.3.1 Formulation of problem

In a physical $z = (x + \mathrm{i}y)$-plane, let the centroids of the hollow vortices be at $x = nL$, $n \in \mathbb{Z}$, where $L$ is the period (i.e. the horizontal distance between two neighbouring centroids). Given this periodic structure, it suffices to consider a single period cell: this cell contains one hollow vortex of finite-area with circulation $\Gamma$, has width $L$, and extends to $\infty^{\pm}$. Here, $\infty^{+}$ denotes the region of the period cell as $y \to +\infty$ while $\infty^{-}$ denotes the region as $y \to -\infty$. Figure 3.1 illustrates this arrangement.

Let $z(\zeta)$ be the conformal mapping taking the unit $\zeta$-disc to a single period cell of the hollow vortex row. Our task is to determine the shape of the boundary of the hollow vortex by constructing a suitable functional form for $z(\zeta)$. The boundary of the hollow vortex will be taken to be the image of the unit circle $|\zeta| = 1$ under the map $z(\zeta)$. Note that traversing $|\zeta| = 1$ in an anticlockwise sense corresponds to traversing the hollow vortex boundary in

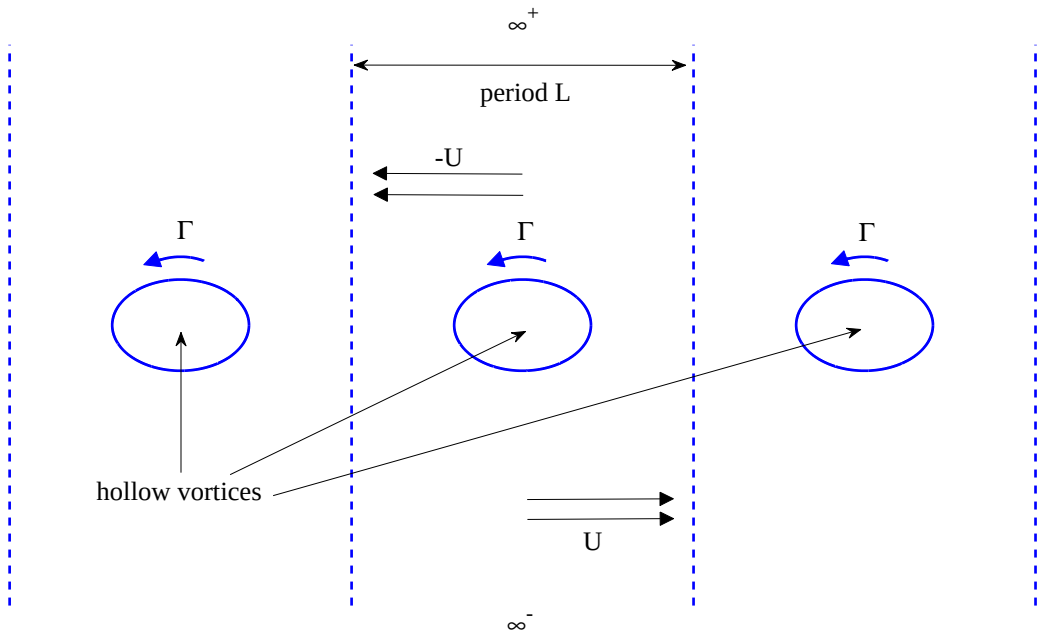


Figure 3.1: Schematic showing three periods of length $L$ of a row of hollow vortices, each of circulation $\Gamma$. The shapes of the hollow vortex boundaries are to be determined.

a clockwise sense (keeping the fluid region on the left). There are two points in the interior of the unit disc, $\zeta = \alpha$ and $\zeta = \beta$, which will map respectively to $\infty^+$ and $\infty^-$. We require $z(\zeta)$ to behave in the following manner near $\zeta = \alpha$:

$$z(\zeta) = -\frac{\mathrm{i}L}{2\pi}\log(\zeta - \alpha) + \text{locally analytic function.} \tag{3.2}$$

In other words, encircling $\zeta = \alpha$ by $2\pi$ corresponds to a jump in $z(\zeta)$ by the real amount $L$. Similarly, near $\zeta = \beta$, we require $z(\zeta)$ to behave in the following manner:

$$z(\zeta) = \frac{\mathrm{i}L}{2\pi}\log(\zeta - \beta) + \text{locally analytic function.} \tag{3.3}$$

That is, encircling $\zeta = \beta$ by $2\pi$ corresponds to a jump in $z(\zeta)$ by the real amount $-L$. A choice of branch cut joining the logarithmic branch points at $\zeta = \alpha$ and $\zeta = \beta$ is required to be made in order to uniquely define the map $z(\zeta)$. We give further details in due course.

The fluid region in a typical period cell of the hollow vortex row is doubly connected: the two boundaries are that of the hollow vortex and the edges of the cell. Introducing a branch cut between $\zeta = \alpha$ and $\zeta = \beta$ has a dual purpose: the two sides of this branch cut will

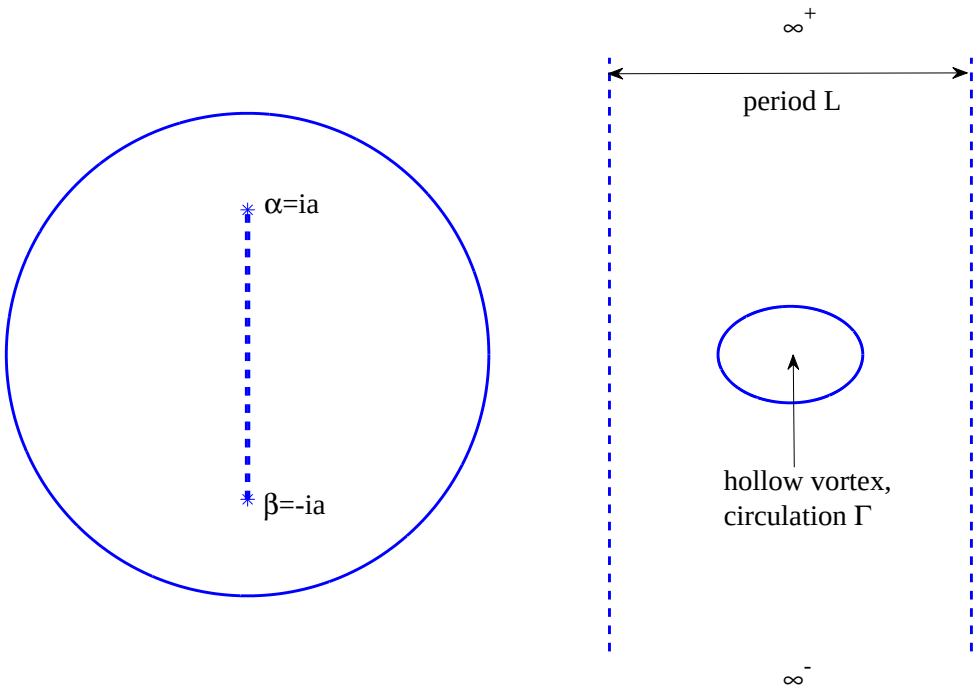


Figure 3.2: The preimage unit $\zeta$-disc with a branch cut, shown as a dashed line, joining $\alpha = \mathrm{i}a = -\beta$ (the preimages of $\infty^+$ and $\infty^-$) chosen along the imaginary $\zeta$-axis [left], and a typical period window of the hollow vortex row [right]. Under the conformal map $z(\zeta)$, the circle $|\zeta| = 1$ is taken to map to the hollow vortex boundary. The two sides of the branch cut map, under $z(\zeta)$, to the two edges of the period window.

be taken to map to the two edges of the period cell under $z(\zeta)$ and this branch cut neatly encodes the intrinsic periodicity structure of the hollow vortex row into our mathematical model. This branch cut could be interpreted as a second boundary in the $\zeta$-plane, but the key point is that we only require periodicity across it. Alternatively, the periodicity structure can be viewed from a Riemann surface perspective. Moving through the branch cut corresponds to moving onto a different sheet of some infinite-sheeted Riemann surface, where each sheet of this surface is a copy of $|\zeta| = 1$ corresponding to a particular period cell in the hollow vortex row.

In our analysis, we shall make use of the bounded circular slit mapping (2.53). Since, for the present problem, we are mapping between two conformally equivalent simply connected domains, (2.53) reduces to

$$\eta(\zeta;\gamma) = \frac{\zeta - \gamma}{|\gamma|\,(\zeta - 1/\overline{\gamma})}, \tag{3.4}$$

where $\gamma \in \mathbb{C}$, $|\gamma| < 1$. It is easy to see that $\eta(\zeta;\gamma)$ has a simple zero at $\zeta = \gamma$. Straightforward algebra can be used to show that $|\eta(\zeta;\gamma)| = 1$ on $|\zeta| = 1$; thus, $\eta(\zeta;\gamma)$ maps the unit $\zeta$-circle onto the unit circle in the complex $\eta$-plane.

### 3.3.2 Function $W(\zeta)$

Let the complex potential for the potential flow associated with the hollow vortex row be denoted by $w(z)$. Owing to the symmetry of the hollow vortex row, the hollow vortices are expected to be in equilibrium, and so $w(z)$ will be defined in a stationary frame of reference. The complex potential $w(z)$ in the $z$-plane is related to the complex potential $W(\zeta)$ in the $\zeta$-plane through the composition

$$W(\zeta) = w(z(\zeta)). \tag{3.5}$$

Let the circulation around the hollow vortex be $\Gamma$; this means that

$$\oint_{|\zeta|=1} d[W(\zeta)] = -\Gamma, \tag{3.6}$$

where $|\zeta| = 1$ is positively oriented in the anticlockwise direction. Notice the appearance of the minus sign on the right-hand-side of (3.6); recall that traversing $|\zeta| = 1$ in an anticlockwise direction corresponds to traversing the hollow vortex boundary in a clockwise

direction. The circulation around the hollow vortex induces the following uniform flow type behaviour of the complex potential:

$$w(z) = \mp Uz + \text{locally analytic function}, \quad z \to \infty^{\pm}. \tag{3.7}$$

The value of $U$ will be determined shortly. The boundary of the hollow vortex must be a streamline of the flow. Thus, on $|\zeta| = 1$, we require

$$\mathrm{Im}[W(\zeta)] = \text{constant}. \tag{3.8}$$

It follows from (3.2), (3.3) and (3.7) that we must have

$$W(\zeta) = \frac{\mathrm{i}LU}{2\pi} \log(\zeta - \alpha) + \text{locally analytic function}, \quad \zeta \to \alpha, \tag{3.9}$$

and

$$W(\zeta) = \frac{\mathrm{i}LU}{2\pi} \log(\zeta - \beta) + \text{locally analytic function}, \quad \zeta \to \beta. \tag{3.10}$$

We shall now build the complex potential function $W(\zeta)$. Consider the function

$$\mathcal{L}_1(\zeta; \alpha) = \log \eta(\zeta; \alpha), \tag{3.11}$$

where $\eta(\zeta; \alpha)$ is the bounded circular slit mapping of (3.4). Since $\eta(\zeta; \alpha)$ has a simple zero at $\zeta = \alpha$, function $\mathcal{L}_1(\zeta; \alpha)$ must have the following behaviour:

$$\mathcal{L}_1(\zeta; \alpha) = \log(\zeta - \alpha) + \text{locally analytic function}, \quad \zeta \to \alpha. \tag{3.12}$$

Also, since $|\eta(\zeta; \alpha)| = 1$ on $|\zeta| = 1$, we must have that

$$\mathrm{Re}[\mathcal{L}_1(\zeta; \alpha)] = \log |\eta(\zeta; \alpha)| = 0 \tag{3.13}$$

on $|\zeta| = 1$. Let us consider the integral

$$\oint_{|\zeta|=1} d[\mathcal{L}_1(\zeta; \alpha)], \tag{3.14}$$

where $|\zeta| = 1$ is positively oriented in the anticlockwise direction. Since this integral is of the logarithmic type, we can invoke the Argument Principle (Ablowitz & Fokas [1]).

Function $\eta(\zeta;\alpha)$ has one simple zero at $\zeta=\alpha$ inside $|\zeta|=1$ and no poles anywhere inside $|\zeta|=1$. Thus, by the Argument Principle, we have

$$\frac{1}{2\pi\mathrm{i}}\oint_{|\zeta|=1} d[\mathcal{L}_1(\zeta;\alpha)] = \frac{1}{2\pi\mathrm{i}}\oint_{|\zeta|=1} d[\log\eta(\zeta;\alpha)] = 1. \tag{3.15}$$

Next, consider the function

$$\mathcal{L}_2(\zeta;\alpha,\beta) = \mathcal{L}_1(\zeta;\alpha)+\mathcal{L}_1(\zeta;\beta) = \log\eta(\zeta;\alpha)\eta(\zeta;\beta). \tag{3.16}$$

Using (3.12), it is clear to see that

$$\mathcal{L}_2(\zeta;\alpha,\beta) = \log(\zeta-\alpha)+\text{locally analytic function}, \quad \zeta\to\alpha, \tag{3.17}$$

and

$$\mathcal{L}_2(\zeta;\alpha,\beta) = \log(\zeta-\beta)+\text{locally analytic function}, \quad \zeta\to\beta. \tag{3.18}$$

Using (3.13), it is also clear to see that on $|\zeta|=1$,

$$\mathrm{Re}[\mathcal{L}_2(\zeta;\alpha,\beta)] = \log|\eta(\zeta;\alpha)|+\log|\eta(\zeta;\beta)| = \log|\eta(\zeta;\alpha)\eta(\zeta;\beta)| = 0. \tag{3.19}$$

From (3.15), it is immediate that

$$\frac{1}{2\pi\mathrm{i}}\oint_{|\zeta|=1} d[\mathcal{L}_2(\zeta;\alpha,\beta)] = \frac{1}{2\pi\mathrm{i}}\oint_{|\zeta|=1} (d[\log\eta(\zeta;\alpha)]+d[\log\eta(\zeta;\beta)]) = 2, \tag{3.20}$$

where $|\zeta|=1$ is positively oriented in the anticlockwise direction.

Consider, thus, the following function:

$$W(\zeta) = \frac{\mathrm{i}LU}{2\pi}\mathcal{L}_2(\zeta;\alpha,\beta), \tag{3.21}$$

i.e.

$$W(\zeta) = \frac{\mathrm{i}LU}{2\pi}\log\eta(\zeta;\alpha)\eta(\zeta;\beta). \tag{3.22}$$

From (3.19), we see that this function has constant imaginary part on $|\zeta|=1$. It has the required behaviours (3.9) and (3.10) owing to (3.17) and (3.18). It also changes by $-\Gamma$ as $|\zeta|=1$ is traversed in an anticlockwise sense thereby producing the required circulation

(3.6) around the hollow vortex, provided

$$U = \frac{\Gamma}{2L}. \tag{3.23}$$

Indeed, using (3.58), we have that

$$\oint_{|\zeta|=1} d[W(\zeta)] = -2LU, \tag{3.24}$$

where $|\zeta| = 1$ is positively oriented in the anticlockwise direction. But from (3.6), it is required that

$$\oint_{|\zeta|=1} d[W(\zeta)] = -\Gamma, \tag{3.25}$$

and hence we must choose $U$ as in (3.23).

Given the symmetry of the arrangement, we take

$$\alpha = \mathrm{i}a = -\beta, \tag{3.26}$$

where $a \in \mathbb{R}$, $|a| < 1$. See Figure 3.2. We shall take the branch cut linking the logarithmic branch points at $\zeta = \pm \mathrm{i}a$ to lie along the segment of the imaginary axis between these points with the two sides of the branch cut mapping to the two edges of the period cell. By the symmetry, the centre of the branch cut at $\zeta = 0$ will map to the two real points on the edges of the period cell and we expect these two points to be stagnation points of the flow. With the choices (3.26) in (3.22), we obtain

$$W(\zeta) = \frac{\mathrm{i}LU}{2\pi} \log\left(\frac{\zeta^2 + a^2}{\zeta^2 + 1/a^2}\right). \tag{3.27}$$

### 3.3.3 Function $dw/dz$

One of the defining properties of the complex velocity function $dw/dz$ stems from Bernoulli's theorem. The boundary of the hollow vortex is a vortex sheet and the pressure is constant inside it. Thus, Bernoulli's theorem implies that the fluid speed is constant on the hollow vortex boundary. Consequently, on $|\zeta| = 1$:

$$\left|\frac{dw}{dz}\right| = \text{constant}. \tag{3.28}$$

$dw/dz$ must also incorporate the stagnation points lying on the real axis on the edges of the period cell:

$$\frac{dw}{dz}(0) = 0. \tag{3.29}$$

Finally, $dw/dz$ must be $L$-periodic.

It turns out that the complex velocity function takes a particularly simple form:

$$\frac{dw}{dz} = R\zeta, \tag{3.30}$$

where $R \in \mathbb{C}$ is a constant. This function (3.30) is clearly analytic and single-valued everywhere in $|\zeta| < 1$; in particular, it is invariant as either $\zeta = \pm \mathrm{i}a$ are encircled. Hence, $dw/dz$ is $L$-periodic across the period cell. Function (3.30) also clearly has constant modulus on $|\zeta| = 1$, and a simple zero at $\zeta = 0$, as required. In light of (3.7), we must have that

$$\frac{dw}{dz} = -U + \text{locally analytic function}, \quad \zeta \to \mathrm{i}a, \tag{3.31}$$

and so it follows at once that

$$R = \frac{\mathrm{i}U}{a}. \tag{3.32}$$

It is then apparent that

$$\frac{dw}{dz} = U + \text{locally analytic function}, \quad \zeta \to -\mathrm{i}a, \tag{3.33}$$

as required by (3.7).

### 3.3.4 Conformal map $z(\zeta)$

Free streamline theory allows us to derive an expression for the derivative of the conformal map using the chain rule, given separate expressions for $W(\zeta)$ and $dw/dz$:

$$\frac{dz}{d\zeta} = \frac{dW/d\zeta}{dw/dz}. \tag{3.34}$$

Using (3.30) and the derivative of (3.27) with respect to $\zeta$ in (3.34), it follows that

$$\frac{dz}{d\zeta} = \frac{aL}{\pi}\left(\frac{1}{\zeta^2 + a^2} - \frac{1}{\zeta^2 + 1/a^2}\right). \tag{3.35}$$

On integration, the conformal map is found to be

$$z(\zeta) = \frac{L}{\pi}\left(\tan^{-1}(\zeta/a) - a^2\tan^{-1}(a\zeta)\right) + z_0, \tag{3.36}$$

where $z_0 \in \mathbb{C}$ is a constant. Given the period $L$, (3.36) represents a one-parameter family of conformal maps governing the shape of the boundary of the hollow vortex. The dependency on the single real parameter $a$ can be viewed as a measure of the area of the hollow vortex. Our solution (3.36) is different (and, arguably, in a more concise form) to that of Baker, Saffman & Sheffield [7], but it can be shown to be equivalent (see Appendix B).

## 3.4 Hollow vortex streets

Using the ideas developed in the preceding section, we can now shift attention to finding solutions describing the shapes of hollow vortices in a street configuration. By a street of hollow vortices, we mean two parallel rows of hollow vortices where the hollow vortices in one row have an equal and opposite circulation to those in the other row, and these streets can be either staggered or unstaggered. We will focus specifically on solutions where the hollow vortices in each row have identical shapes and are of equal area. In principle, our method should be able to be modified to cater for more general classes of solution describing, perhaps, configurations where the areas of the hollow vortices are different in each row.

### 3.4.1 Formulation of problem

In a physical $z = (x+\mathrm{i}y)$-plane, consider a von Kármán street of hollow vortices consisting of two rows of equal area hollow vortices moving in unbounded fluid. Let the centroids of the hollow vortices in both rows be separated by a horizontal distance $L$. Let the circulation around the hollow vortices in the top row be $\Gamma$ (where $\Gamma > 0$) and let the circulation around the hollow vortices in the bottom row be $-\Gamma$. We will seek solutions for which the street is expected to translate steadily parallel to the $x$-axis towards the right with speed $U$. Figure 3.3 shows a schematic of this configuration for a typical staggered hollow vortex street.

Consider a conformal mapping $z(\zeta)$ from the concentric annulus $\rho < |\zeta| < 1$ to a single period cell of the hollow vortex street in the $z$-plane. The circles $|\zeta| = 1$ and $|\zeta| = \rho$ will be mapped onto the boundaries of the two hollow vortices in the period cell. Note that

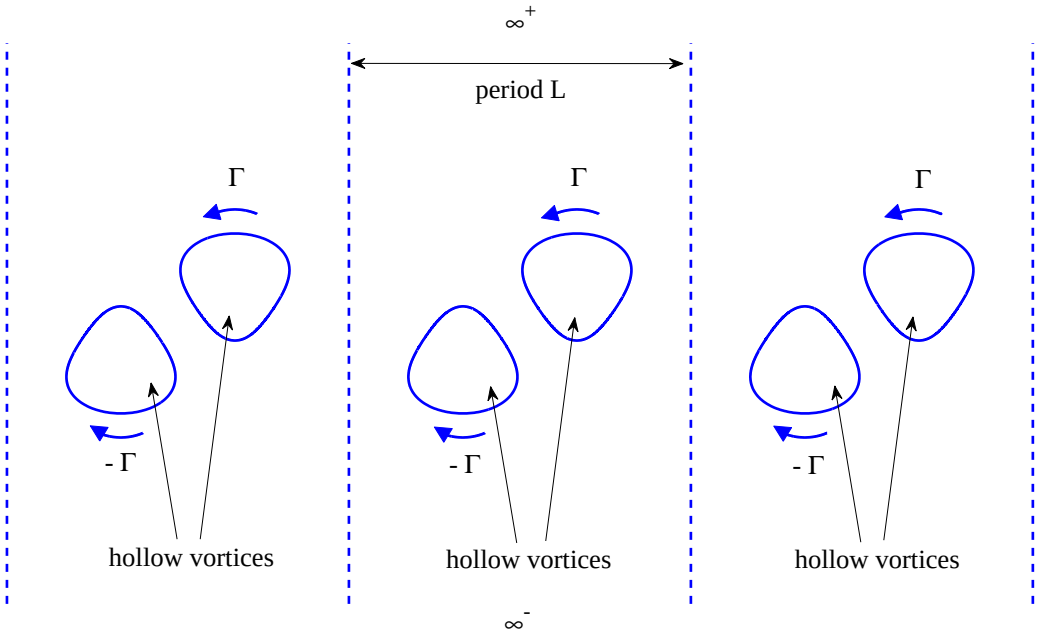


Figure 3.3: Schematic showing three periods of a period-$L$ von Kármán street of hollow vortices. The hollow vortices will be taken to have circulation $\Gamma$ in the top row and $-\Gamma$ in the bottom row. The hollow vortex street is expected to translate with speed $U$ towards the right. The shape of the vortex sheets bounding the hollow regions are to be determined.

traversing $|\zeta| = 1$ in an anticlockwise sense corresponds to traversing the boundary of its image in a clockwise sense, but traversing $|\zeta| = \rho$ in an anticlockwise sense corresponds to traversing the boundary of its image in an anticlockwise sense. As before, two interior points of the annulus, $\zeta = \alpha$ and $\zeta = \beta$, will map to $\infty^+$ and $\infty^-$, respectively. Near $\zeta = \alpha$, we must have

$$z(\zeta) = -\frac{\mathrm{i}L}{2\pi}\log(\zeta - \alpha) + \text{locally analytic function}, \tag{3.37}$$

and near $\zeta = \beta$, we must have

$$z(\zeta) = \frac{\mathrm{i}L}{2\pi}\log(\zeta - \beta) + \text{locally analytic function}. \tag{3.38}$$

Like before, we must of course also make a choice of branch cut in the interior of the annulus $\rho < |\zeta| < 1$ joining the two points $\zeta = \alpha$ and $\zeta = \beta$ in order to uniquely define $z(\zeta)$. The two sides of this branch cut will map to the two edges of the period cell. By a rotational degree of freedom in the Riemann-Koebe mapping theorem (Goluzin [52]), we can take $\alpha \in \mathbb{R}$ and lying on the positive real axis. See Figure 3.4.

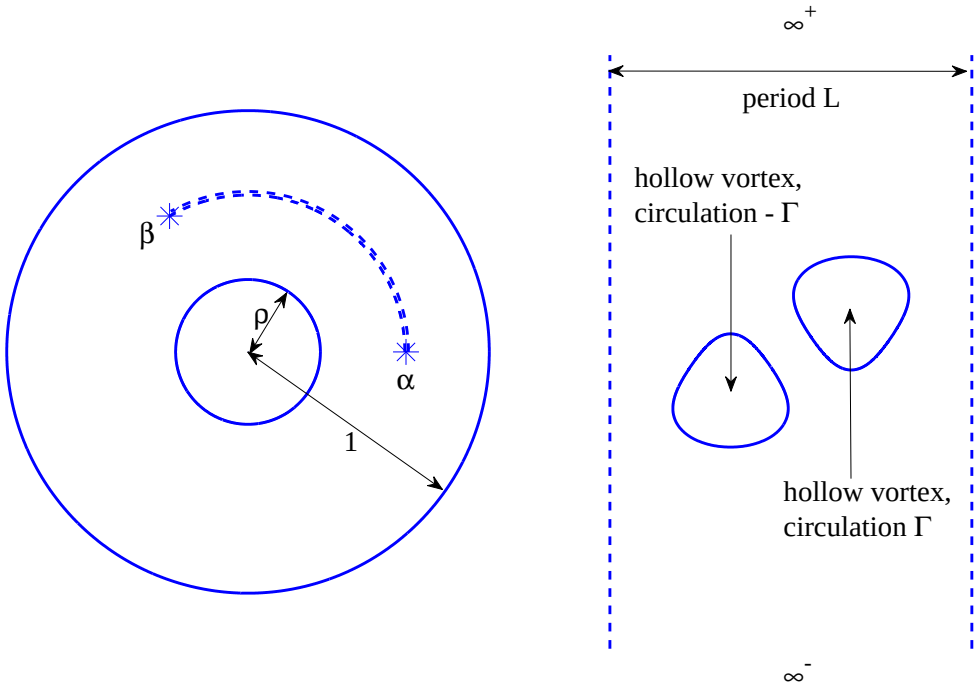


Figure 3.4: The preimage annulus $\rho < |\zeta| < 1$ [left] and a typical period window of a von Kármán hollow vortex street [right]. The two sides of the branch cut, shown as a dashed line, joining $\zeta = \alpha$ and $\zeta = \beta$ (the preimages of $\infty^+$ and $\infty^-$) are mapped by $z(\zeta)$ onto the two edges of the period window. The two circles $|\zeta| = 1$ and $|\zeta| = \rho$ each map to one of the hollow vortex boundaries.

The fluid region in a typical period cell of the hollow vortex street is triply connected: the three boundaries are those of the two hollow vortices and the edges of the period cell. To proceed, we will use the same technique as we did for the single row: introduce a branch cut linking $\zeta = \alpha$ and $\zeta = \beta$. As before, this serves two main purposes: the two sides of the branch cut will be taken to map to the two edges of the period cell under $z(\zeta)$ and this branch cut neatly encapsulates the intrinsic periodicity structure of the hollow vortex street into our mathematical model. Moving through the branch cut corresponds to moving onto a different sheet of some infinite-sheeted Riemann surface, where each sheet of this surface is a copy of the concentric annulus $\rho < |\zeta| < 1$ corresponding to a particular period cell in the hollow vortex street.

Also like before, we shall again employ the bounded circular slit mapping (2.53). We are now mapping between two conformally equivalent doubly connected domains. In this case, (2.53) becomes

$$\eta(\zeta;\gamma) = \frac{|\gamma| P(\zeta/\gamma, \rho)}{P(\zeta\overline{\gamma}, \rho)}. \tag{3.39}$$

Here, $\gamma \in \mathbb{C}$ is an arbitrary point in the interior of the annulus $\rho < |\zeta| < 1$. Note that $\eta(\zeta;\gamma)$ has a simple zero at $\zeta = \gamma$. Straightforward manipulations using the relations (2.31) can be used to show that $\eta(\zeta;\gamma)$ has constant modulus on both $|\zeta| = 1$ and $|\zeta| = \rho$. It can be shown that $\eta(\zeta;\gamma)$ maps $|\zeta| = 1$ onto the unit circle in the complex $\eta$-plane with $|\zeta| = \rho$ mapping onto a finite-length concentric circular slit in the interior of $|\eta| = 1$.

### 3.4.2 Function $W(\zeta)$

We expect the hollow vortex street to translate uniformly, without change of form, in the positive $x$-direction with speed $U$. Let the complex potential for the potential flow associated with the hollow vortex street in a co-travelling frame with the street be denoted by $w(z)$; in this co-travelling frame, the hollow vortices will be in a state of relative equilibrium. Introduce the composition

$$W(\zeta) = w(z(\zeta)). \tag{3.40}$$

Let the circulations around the two hollow vortices be $\pm\Gamma$; this means that

$$\oint_{|\zeta|=1} d[W(\zeta)] = -\oint_{|\zeta|=\rho} d[W(\zeta)] = -\Gamma, \tag{3.41}$$

where both $|\zeta| = 1$ and $|\zeta| = \rho$ are positively oriented in the anticlockwise direction. As $z \to \infty^{\pm}$, we require

$$w(z) = -Uz + \text{locally analytic function.} \tag{3.42}$$

The hollow vortices are stationary in the co-travelling frame and their boundaries will be streamlines. Thus, on both $|\zeta| = 1$ and $|\zeta| = \rho$, we require

$$\mathrm{Im}[W(\zeta)] = \text{constant.} \tag{3.43}$$

It follows from (3.37), (3.38) and (3.42) that we need to ensure that

$$W(\zeta) = \frac{\mathrm{i}LU}{2\pi}\log(\zeta - \alpha) + \text{locally analytic function}, \quad \zeta \to \alpha, \tag{3.44}$$

and

$$W(\zeta) = -\frac{\mathrm{i}LU}{2\pi}\log(\zeta - \beta) + \text{locally analytic function}, \quad \zeta \to \beta. \tag{3.45}$$

We shall now build the complex potential function $W(\zeta)$. Consider the function

$$\mathcal{L}_1(\zeta;\alpha) = \log\eta(\zeta;\alpha), \tag{3.46}$$

where $\eta(\zeta;\alpha)$ is the bounded circular slit mapping of (3.39). Since $\eta(\zeta;\alpha)$ has a simple zero at $\zeta = \alpha$, function $\mathcal{L}_1(\zeta;\alpha)$ must have the following behaviour:

$$\mathcal{L}_1(\zeta;\alpha) = \log(\zeta - \alpha) + \text{locally analytic function}, \quad \zeta \to \alpha. \tag{3.47}$$

Also, since $|\eta(\zeta;\alpha)| = \text{constant}$ on both $|\zeta| = 1$ and $|\zeta| = \rho$, we must have that

$$\mathrm{Re}[\mathcal{L}_1(\zeta;\alpha)] = \log|\eta(\zeta;\alpha)| = \text{constant} \tag{3.48}$$

on $|\zeta| = 1$ and $|\zeta| = \rho$. Let us consider the integral

$$\oint_{|\zeta|=1} d[\mathcal{L}_1(\zeta;\alpha)], \tag{3.49}$$

where $|\zeta| = 1$ is positively oriented in the anticlockwise direction. Since this integral is of the logarithmic type, we can invoke the Argument Principle. The simple zeroes of $\eta(\zeta;\alpha)$

inside $|\zeta| = 1$ are

$$\alpha, \quad \left\{\alpha\rho^{2j} \mid j \in \mathbb{N}\right\}, \tag{3.50}$$

and the simple poles of $\eta(\zeta;\alpha)$ inside $|\zeta| = 1$ are

$$\left\{\rho^{2j}/\overline{\alpha} \mid j \in \mathbb{N}\right\}. \tag{3.51}$$

Note that the cardinality of the sets $\{\alpha\rho^{2j} \mid j \in \mathbb{N}\}$ and $\{\rho^{2j}/\overline{\alpha} \mid j \in \mathbb{N}\}$ is equal. Let $N-P$ denote the difference between the number of simple zeroes and the number of simple poles of function $\eta(\zeta;\alpha)$ lying inside $|\zeta| = 1$. Thus, by the Argument Principle, we have

$$\frac{1}{2\pi\mathrm{i}}\oint_{|\zeta|=1} d[\mathcal{L}_1(\zeta;\alpha)] = \frac{1}{2\pi\mathrm{i}}\oint_{|\zeta|=1} d[\log\eta(\zeta;\alpha)] = N - P = 1. \tag{3.52}$$

Next, consider the function

$$\mathcal{L}_2(\zeta;\alpha,\beta) = \mathcal{L}_1(\zeta;\alpha) - \mathcal{L}_1(\zeta;\beta) = \log\left(\frac{\eta(\zeta;\alpha)}{\eta(\zeta;\beta)}\right). \tag{3.53}$$

Using (3.47), it is clear to see that

$$\mathcal{L}_2(\zeta;\alpha,\beta) = \log(\zeta-\alpha) + \text{locally analytic function}, \quad \zeta \to \alpha, \tag{3.54}$$

and

$$\mathcal{L}_2(\zeta;\alpha,\beta) = -\log(\zeta-\beta) + \text{locally analytic function}, \quad \zeta \to \beta. \tag{3.55}$$

Using (3.48), it is also clear to see that

$$\mathrm{Re}[\mathcal{L}_2(\zeta;\alpha,\beta)] = \log|\eta(\zeta;\alpha)| - \log|\eta(\zeta;\beta)| = \log\left|\frac{\eta(\zeta;\alpha)}{\eta(\zeta;\beta)}\right| = \text{constant}. \tag{3.56}$$

From (3.52), it is immediate that

$$\frac{1}{2\pi\mathrm{i}}\oint_{|\zeta|=1} d[\mathcal{L}_2(\zeta;\alpha,\beta)] = \frac{1}{2\pi\mathrm{i}}\oint_{|\zeta|=1} (d[\log\eta(\zeta;\alpha)] - d[\log\eta(\zeta;\beta)]) = 0. \tag{3.57}$$

The preceding analysis is very similar in order to show that

$$\frac{1}{2\pi\mathrm{i}}\oint_{|\zeta|=\rho} d[\mathcal{L}_2(\zeta;\alpha,\beta)] = 0. \tag{3.58}$$

Consider, thus, the function

$$W(\zeta) = -\frac{\mathrm{i}\Gamma}{2\pi}\log\zeta + \frac{\mathrm{i}LU}{2\pi}\mathcal{L}_2(\zeta;\alpha,\beta), \tag{3.59}$$

i.e.

$$W(\zeta) = -\frac{\mathrm{i}\Gamma}{2\pi}\log\zeta + \frac{\mathrm{i}LU}{2\pi}\log\left(\frac{\eta(\zeta;\alpha)}{\eta(\zeta;\beta)}\right). \tag{3.60}$$

From (3.56), we see that this function has constant imaginary part on both $|\zeta| = 1$ and $|\zeta| = \rho$. It has the required behaviours (3.44) and (3.45), owing to (3.54) and (3.55). It also changes by $\Gamma$ as either $|\zeta| = 1$ or $|\zeta| = \rho$ is traversed in an anticlockwise sense thereby producing the required circulations (3.41) around the hollow vortices (to see this, recall (3.57) and (3.58)).

### 3.4.3 Function $\zeta W_\zeta(\zeta)$

In order to derive the most convenient analytical expression for the conformal map $z(\zeta)$, it is necessary to make some further analytical observations.

From the boundary conditions (3.43), it is straightforward to deduce that on $|\zeta| = 1$, we have

$$W(\zeta) - \overline{W}(\zeta^{-1}) = \text{constant}, \tag{3.61}$$

whilst on $|\zeta| = \rho$, we have

$$W(\zeta) - \overline{W}(\rho^2\zeta^{-1}) = \text{constant}. \tag{3.62}$$

These relations (3.61) and (3.62) can be analytically continued off their respective circles to deduce the following functional relation for function $W(\zeta)$:

$$W(\rho^2\zeta) = W(\zeta) + \text{constant}. \tag{3.63}$$

Taking a derivative of (3.63) with respect to $\zeta$ yields

$$\rho^2 W_\zeta(\rho^2\zeta) = W_\zeta(\zeta), \tag{3.64}$$

where we denote $W_\zeta = dW/d\zeta$ (and similarly for other functions). Let us define the

function

$$S(\zeta) = \zeta W_\zeta(\zeta). \tag{3.65}$$

It follows immediately on multiplication of (3.64) by $\zeta$ that we have

$$S(\rho^2\zeta) = S(\zeta). \tag{3.66}$$

In other words, the function $S(\zeta)$ is invariant if its argument undergoes the transformation $\zeta \mapsto \rho^2\zeta$. Meromorphic functions satisfying this property (3.66) are known as loxodromic functions (Valiron [113]).

Let us deduce another important property of function $S(\zeta)$. After analytic continuation off $|\zeta| = 1$, taking a derivative of (3.61) with respect to $\zeta$ yields

$$W_\zeta(\zeta) + \zeta^{-2}\overline{W}_\zeta(\zeta^{-1}) = 0, \tag{3.67}$$

from which it follows that

$$S(\zeta) = -\overline{S}(\zeta^{-1}). \tag{3.68}$$

From (3.44) and (3.45), we require $W_\zeta(\zeta)$ to have simple poles at $\zeta = \alpha$ and $\zeta = \beta$, implying that $S(\zeta)$ must also have simple poles at $\zeta = \alpha$ and $\zeta = \beta$. It follows from (3.68) that if $S(\zeta)$ has simple poles at $\zeta = \alpha$ and $\zeta = \beta$, then it will necessarily have simple poles at $\zeta = 1/\overline{\alpha}$ and $\zeta = 1/\overline{\beta}$.

From an analysis of the von Kármán point vortex street (see Appendix A), in both the unstaggered and staggered cases, we expect two stagnation points in a typical period cell. For the von Kármán hollow vortex street, let the preimages in the annulus $\rho < |\zeta| < 1$ of the two stagnation points in a typical period cell be labelled $\zeta = \gamma_1$ and $\zeta = \gamma_2$. Then the complex velocity function must have two simple zeroes at these points:

$$\frac{dw}{dz}(\gamma_1) = \frac{dw}{dz}(\gamma_2) = 0. \tag{3.69}$$

By the chain rule:

$$W_\zeta(\zeta) = \frac{dw}{dz}\frac{dz}{d\zeta}. \tag{3.70}$$

Now, $dz/d\zeta$ must be non-zero everywhere in $\rho < |\zeta| < 1$ (ensuring that $z(\zeta)$ is indeed a conformal map). Thus, any zeroes of $dw/dz$ in $\rho < |\zeta| < 1$ must also be zeroes of $W_\zeta(\zeta)$

in $\rho < |\zeta| < 1$.

It follows that we also require $\zeta = \gamma_1$ and $\zeta = \gamma_2$ to be simple zeroes of $W_\zeta(\zeta)$ implying that $S(\zeta)$ must also have simple zeroes at $\zeta = \gamma_1$ and $\zeta = \gamma_2$. It follows from (3.68) that if $S(\zeta)$ has simple zeroes at $\zeta = \gamma_1$ and $\zeta = \gamma_2$, then it will necessarily have simple zeroes at $\zeta = 1/\overline{\gamma_1}$ and $\zeta = 1/\overline{\gamma_2}$. In light of property (3.66), it suffices to build the singularity structure of function $S(\zeta)$ in the fundamental region $\rho \leq |\zeta| < 1/\rho$; this is because the singularity structure of $S(\zeta)$ in all other concentric annuli in the $\zeta$-plane can be deduced using relation (3.66).

Consider the function

$$\frac{P(\zeta/\gamma_1,\rho)P(\zeta\overline{\gamma_1},\rho)P(\zeta/\gamma_2,\rho)P(\zeta\overline{\gamma_2},\rho)}{P(\zeta/\alpha,\rho)P(\zeta\overline{\alpha},\rho)P(\zeta/\beta,\rho)P(\zeta\overline{\beta},\rho)}. \tag{3.71}$$

This function (3.71) can be shown to be loxodromic by using the properties (2.31), provided the product of its zeroes is equal to the product of its poles:

$$\frac{\gamma_1\gamma_2}{\overline{\gamma_1\gamma_2}} = \frac{\alpha\beta}{\overline{\alpha\beta}}. \tag{3.72}$$

Function (3.71) has only simple zeroes and simple poles in the fundamental region $\rho \leq |\zeta| < 1/\rho$. Moreover, it has precisely the same simple zeroes $\zeta = \gamma_1, 1/\overline{\gamma_1}, \gamma_2, 1/\overline{\gamma_2}$ and simple poles $\zeta = \alpha, 1/\overline{\alpha}, \beta, 1/\overline{\beta}$ as required of function $S(\zeta)$. Appealing to a special version of Liouville's theorem for loxodromic functions (Valiron [113]), functions $S(\zeta)$ and (3.71) are in fact proportional:

$$\zeta W_\zeta(\zeta) = \mathcal{B}\frac{P(\zeta/\gamma_1,\rho)P(\zeta\overline{\gamma_1},\rho)P(\zeta/\gamma_2,\rho)P(\zeta\overline{\gamma_2},\rho)}{P(\zeta/\alpha,\rho)P(\zeta\overline{\alpha},\rho)P(\zeta/\beta,\rho)P(\zeta\overline{\beta},\rho)}. \tag{3.73}$$

Here, $\mathcal{B} \in \mathbb{C}$ is a constant.

### 3.4.4 Function $dw/dz$

We will now construct the complex velocity function $dw/dz$. Bernoulli's theorem implies that on $|\zeta| = 1$ and $|\zeta| = \rho$,

$$\left|\frac{dw}{dz}\right| = \text{constant}. \tag{3.74}$$

Recall from (3.69) that we require

$$\frac{dw}{dz}(\gamma_1) = \frac{dw}{dz}(\gamma_2) = 0. \tag{3.75}$$

We also require $dw/dz$ to be $L$-periodic.

Consider the function

$$\frac{dw}{dz} = \frac{R\eta(\zeta;\gamma_1)\eta(\zeta;\gamma_2)}{\zeta}. \tag{3.76}$$

This function has constant modulus on $|\zeta| = 1$ and $|\zeta| = \rho$, and two simple zeroes at $\zeta = \gamma_1$ and $\zeta = \gamma_2$. It is analytic and single-valued everywhere in $\rho < |\zeta| < 1$; in particular, it is invariant as either $\zeta = \alpha$ or $\zeta = \beta$ is encircled, and hence $L$-periodic across the period window. The factor of $\zeta$ in the denominator can be explained as follows. Recall, from either (3.60) or (3.73), that $W_\zeta(\zeta)$ has a simple pole at $\zeta = 0$. In order that $z_\zeta(\zeta)$ does not have a simple pole at $\zeta = 0$, and thereby be appropriately single-valued upon traversing either $|\zeta| = 1$ or $|\zeta| = \rho$ (for particular values of $\zeta = \gamma_1$ and $\zeta = \gamma_2$ to be determined), it is required that $dw/dz$ must indeed have a simple pole at $\zeta = 0$.

### 3.4.5 Conformal map $z(\zeta)$

Given the functions in (3.73) and (3.76), it follows from the chain rule that

$$\frac{dz}{d\zeta} = \mathcal{A}\frac{P^2(\zeta\overline{\gamma_1},\rho)P^2(\zeta\overline{\gamma_2},\rho)}{P(\zeta/\alpha,\rho)P(\zeta\overline{\alpha},\rho)P(\zeta/\beta,\rho)P(\zeta\overline{\beta},\rho)}, \tag{3.77}$$

where $\mathcal{A} \in \mathbb{C}$ is a constant. The final form of the conformal map $z(\zeta)$ is

$$z(\zeta) = \mathcal{A}\int_{\zeta_0}^{\zeta} \frac{P^2(\zeta'\overline{\gamma_1},\rho)P^2(\zeta'\overline{\gamma_2},\rho)}{P(\zeta'/\alpha,\rho)P(\zeta'\overline{\alpha},\rho)P(\zeta'/\beta,\rho)P(\zeta'\overline{\beta},\rho)}d\zeta'. \tag{3.78}$$

We have found that this conformal map (3.78) encapsulates both unstaggered and staggered street configurations. Here, $\zeta_0 \in \mathbb{C}$ is an arbitrary point in the annulus $\rho < |\zeta| < 1$. It reflects a translational degree of freedom and determines the position of the origin in the $z$-plane; this can be set arbitrarily and the mapping shifted by an appropriate constant *a posteriori*. The value of $\mathcal{A}$ is found *a posteriori* by insisting that the residue of $dz/d\zeta$ at $\zeta = \alpha$ is $-\mathrm{i}L/2\pi$ as required by (3.37). We thus obtain the following expression for the constant $\mathcal{A}$:

$$\mathcal{A} = \frac{\mathrm{i}L}{2\pi}\left(\frac{\hat{P}(1,\rho)P(|\alpha|^2,\rho)P(\alpha/\beta,\rho)P(\alpha\overline{\beta},\rho)}{\alpha P^2(\alpha\overline{\gamma_1},\rho)P^2(\alpha\overline{\gamma_2},\rho)}\right), \tag{3.79}$$

where

$$\hat{P}(\zeta,\rho)=\frac{P(\zeta,\rho)}{1-\zeta}. \tag{3.80}$$

Recall that $\zeta=\gamma_1$ and $\zeta=\gamma_2$ are two solutions in $\rho<|\zeta|<1$ of the equation

$$\frac{dW}{d\zeta}(\zeta)=0, \tag{3.81}$$

which, on use of (2.42) and (3.60), can be expressed as

$$K(\zeta/\alpha,\rho)-K(\zeta\overline{\alpha},\rho)-K(\zeta/\beta,\rho)+K(\zeta\overline{\beta},\rho)=\frac{\Gamma}{LU}, \tag{3.82}$$

where we recall that

$$K(\zeta,\rho)=\zeta\frac{P'(\zeta,\rho)}{P(\zeta,\rho)}. \tag{3.83}$$

Since

$$\frac{dw}{dz}\to -U,\quad z\to\infty^{\pm}, \tag{3.84}$$

we must have

$$\frac{R\eta(\alpha;\gamma_1)\eta(\alpha;\gamma_2)}{\alpha}=\frac{R\eta(\beta;\gamma_1)\eta(\beta;\gamma_2)}{\beta}=-U. \tag{3.85}$$

One of the equations in (3.85) can be used to determine the value of $R$; the velocity field then follows from (3.76). If the velocity field in a typical period cell is required, a particular choice of branch cut between $\zeta=\alpha$ and $\zeta=\beta$ needs to be made in order to guarantee that the edges of the period cell are straight and vertical. To find such a branch cut, it is necessary to solve an ordinary differential equation for $\zeta$ as a function of $z$ obtained by differentiating the equation

$$\mathrm{Re}[z(\zeta)]=\text{constant} \tag{3.86}$$

and then making use of the expression (3.77) for $dz/d\zeta$. It should be noted that the shapes of the two edges of the period cell (i.e. the images of the two sides of the branch cut under $z(\zeta)$) are irrelevant if one is interested solely in determining the shapes of the hollow vortex boundaries. As mentioned before, the key point of introducing the branch cut between $\zeta=\alpha$ and $\zeta=\beta$ is to capture the periodicity structure of the hollow vortex street.

### 3.4.6 Characterisation of the solutions

We fix

$$L = \Gamma = 1 \tag{3.87}$$

which sets the length scale and the time scale, respectively. Both unstaggered and staggered von Kármán streets of point vortices admit one-parameter families of equilibrium solutions (see Appendix A): we shall take this parameter to be $U$. For a hollow vortex street, we expect an additional freedom associated with the area of the hollow vortices: the parameter $\rho$ is a natural choice for this.

We will now examine the solution spaces for both unstaggered and staggered hollow vortex streets. For both street configurations, we find two-parameter families of solutions parameterised by $\rho$ and $U$. We choose a value of $U$ *a priori* and proceed in tracing out a solution branch corresponding to this value of $U$ by a continuation procedure in $\rho$; that is, gradually increasing $\rho$ to obtain hollow vortices of gradually increasing area. For small values of $\rho$, the hollow vortices are always found to be small and close-to-circular in shape.

#### Unstaggered streets

It has been found that unstaggered hollow vortex streets exist for $U \gtrsim 0.5$; this is consistent with the result for point vortex streets as indicated in Appendix A. We have found that the parameters $\alpha$, $\beta$, $\gamma_1$ and $\gamma_2$ are either all real and such that

$$\beta = \frac{\rho}{\alpha}, \quad \gamma_2 = \frac{\rho}{\gamma_1}, \tag{3.88}$$

or are such that

$$\beta = \frac{\rho}{\alpha}, \quad \gamma_2 = \overline{\gamma_1} = \sqrt{\rho}\mathrm{e}^{\mathrm{i}\phi}, \tag{3.89}$$

with $\alpha, \beta, \phi \in \mathbb{R}$. Figure 3.5 shows two schematics of the preimage domain in the $\zeta$-plane illustrating the locations of the parameters $\alpha$, $\beta$, $\gamma_1$ and $\gamma_2$ according to (3.88) and (3.89). With the choices (3.88) and (3.89), it turns out that the images of the circles $|\zeta| = \rho$ and $|\zeta| = 1$ under the map $z(\zeta)$ are reflections of each other through a horizontal midline between them. Recall that we are restricting attention to hollow vortices whose shapes and areas are the same in both rows, and thus, given the symmetry, it is not necessary to enforce an equation requiring the hollow vortex areas, or perimeters, be equal.

Given $U$ and $\rho$, we solve two real equations for $\alpha$ and $\gamma_1$; $\beta$ and $\gamma_2$ then follow immediately from either (3.88) or (3.89). The first equation to enforce is

$$\mathrm{Im}\left[\oint_{|\zeta|=1} z_\zeta(\zeta')d\zeta'\right] = 0 \tag{3.90}$$

so that the conformal map be appropriately single-valued. By the symmetry, imposing (3.90) is sufficient to ensure that also

$$\mathrm{Im}\left[\oint_{|\zeta|=\rho} z_\zeta(\zeta')d\zeta'\right] = 0. \tag{3.91}$$

With the choice of parameters (3.88) and (3.89), it turns out to be automatic that

$$\mathrm{Re}\left[\oint_{|\zeta|=1} z_\zeta(\zeta')d\zeta'\right] = \mathrm{Re}\left[\oint_{|\zeta|=\rho} z_\zeta(\zeta')d\zeta'\right] = 0. \tag{3.92}$$

The second equation to enforce is

$$K(\gamma_1/\alpha,\rho) - K(\gamma_1\overline{\alpha},\rho) - K(\gamma_1/\beta,\rho) + K(\gamma_1\overline{\beta},\rho) = \frac{\Gamma}{LU} \tag{3.93}$$

so that function $W_\zeta(\zeta)$ has the correct zero structure: by the symmetry, imposing (3.93) is sufficient to ensure that $W_\zeta(\zeta)$ will also have a zero at $\zeta = \gamma_2$, as required. Equations (3.90) and (3.93) can be readily solved using Newton's method.

For each fixed value of $0.5 \lesssim U < 0.5773502693$, there is a critical value of $\rho = \rho^*$ (say) below which all parameters are real and satisfy the relations in (3.88). When $\rho = \rho^*$, $\gamma_1$ and $\gamma_2$ coincide at $\zeta = \sqrt{\rho}$. Then, for $\rho > \rho^*$, $\gamma_1$ and $\gamma_2$ become a complex conjugate pair on the circle $|\zeta| = \sqrt{\rho}$. Figure 3.6 shows a graph of the critical value of $\rho$ as a function of $U$. This transition of $\gamma_1$ and $\gamma_2$ off the real axis onto the circle $|\zeta| = \sqrt{\rho}$ has a physical significance: the two stagnation points lying on the edge of each period cell move off the edges onto the real $z$-axis. For $U > 0.5773502693$, the parameters $\alpha$, $\beta$, $\gamma_1$ and $\gamma_2$ are such that they obey the relations in (3.89) and, therefore, the stagnation points for these solutions are always on the real $z$-axis.

In Figure 3.7, three periods of unstaggered hollow vortex streets are shown for when $U = 0.6$ and $U = 0.8$. It appears from these figures that the maximum area of the hollow vortices decreases as $U$ increases (the graph in Figure 3.12 vindicates this observation). These unstaggered street solutions can be considered as a generalisation of the classical

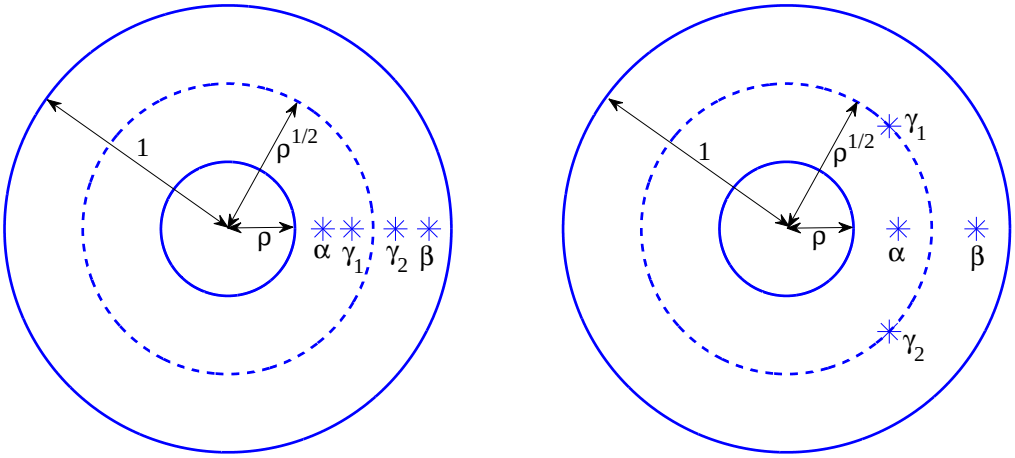


Figure 3.5: The distribution of parameters $\alpha$, $\beta$, $\gamma_1$ and $\gamma_2$ in the two cases (3.88) [left] and (3.89) [right] for the unstaggered street solutions. For fixed $0.5 \lesssim U < 0.5773502693$, there is a critical $\rho$ for which $\gamma_1 = \gamma_2 = \sqrt{\rho}$ represents a transition between the two situations shown.

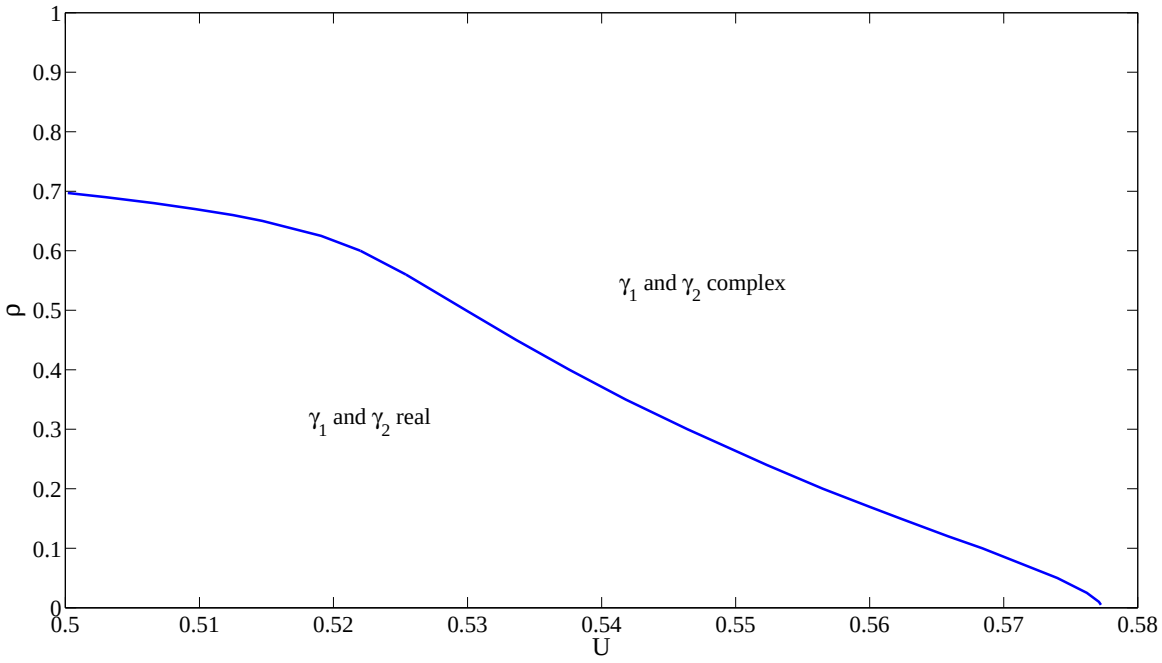


Figure 3.6: A graph showing the critical value of $\rho$, for each $U$, at which the parameters for unstaggered vortex streets transition from satisfying (3.88) to satisfying (3.89).

hollow vortex pair solutions due to Pocklington [85] to the case of a singly periodic array of such hollow vortex pairs moving steadily and uni-directionally. Indeed, the hollow vortex shapes we present look qualitatively similar to those found by Pocklington [85]. A feature characterising the maximum area configurations is the long flattened part of the hollow vortex boundaries which are closest together.

## Staggered streets

We find that solutions for staggered hollow vortex streets exist for $0 < U \lesssim 0.5$; this is again consistent with the staggered point vortex street solutions (see Appendix A). We find that the parameters $\alpha$, $\beta$, $\gamma_1$ and $\gamma_2$ are all real and such that

$$\beta = -\frac{\rho}{\alpha}, \quad \gamma_2 = -\frac{\rho}{\gamma_1}. \tag{3.94}$$

For given values of $\rho$ and $U$, we solve for $\alpha$ and $\gamma_1$ by enforcing

$$\mathrm{Im}\left[\oint_{|\zeta|=1} z_\zeta(\zeta')d\zeta'\right] = 0 \tag{3.95}$$

and

$$K(\gamma_1/\alpha,\rho) - K(\gamma_1\overline{\alpha},\rho) - K(\gamma_1/\beta,\rho) + K(\gamma_1\overline{\beta},\rho) = \frac{\Gamma}{LU}. \tag{3.96}$$

As for unstaggered streets, due to the symmetry, (3.95) is sufficient to ensure that

$$\mathrm{Im}\left[\oint_{|\zeta|=\rho} z_\zeta(\zeta')d\zeta'\right] = 0 \tag{3.97}$$

for staggered streets. With the choice of parameters (3.94), it is automatic that

$$\mathrm{Re}\left[\oint_{|\zeta|=1} z_\zeta(\zeta')d\zeta'\right] = \mathrm{Re}\left[\oint_{|\zeta|=\rho} z_\zeta(\zeta')d\zeta'\right] = 0. \tag{3.98}$$

By the symmetry, imposing (3.96) is sufficient to ensure that $W_\zeta(\zeta)$ will also have a zero at $\zeta = \gamma_2$, as required. Equations (3.95) and (3.96) can be readily solved using Newton's method. The solution branch for the fixed value of $U$ is traced out by a continuation procedure in $\rho$.

Figure 3.8 shows three periods of staggered hollow vortex streets for when $U = 0.2$ and $U = 0.4$. As the areas increase, the hollow vortices assume quasi-triangular shapes with

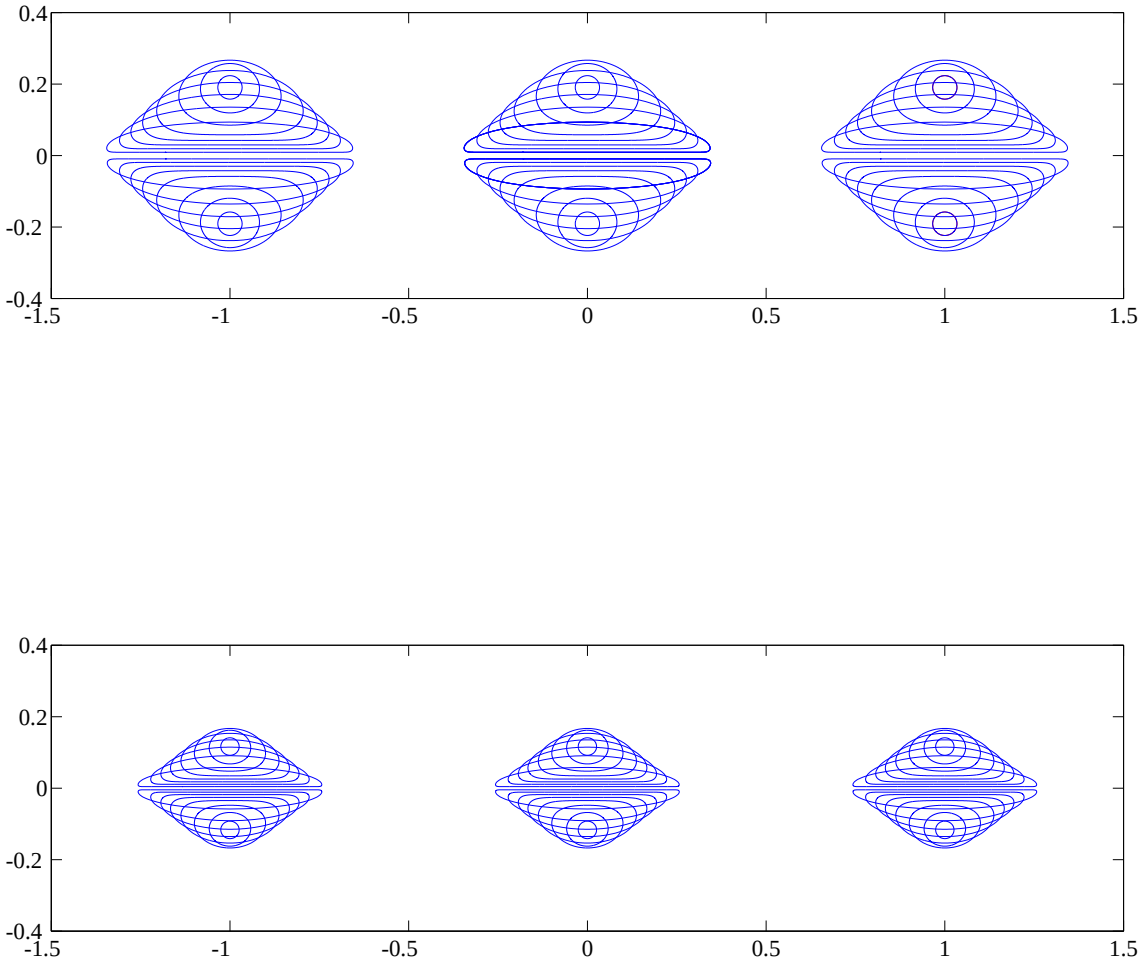


Figure 3.7: Three periods of unstaggered hollow vortex streets, showing hollow vortices of different areas, with speeds $U = 0.6$ [top] and $U = 0.8$ [bottom]. The different solutions have been superposed. The maximum possible area of the hollow vortices in the street decreases as $U$ increases.

two flattened regions of their boundary which are nearest to the neighbouring hollow vortices in the adjacent row. It is interesting that these quasi-triangular shapes are reminiscent of the shapes of the vortices appearing in photographs of certain staggered vortex streets shown, for example, in Van Dyke [114]. For a fixed $U$, we find that $\rho$ can be increased up to some limiting value with no apparent singularity in the hollow vortex shapes and without the conformal map becoming multi-valued.

Our staggered street solutions are the hollow vortex analogues of the staggered streets of vortex patches found by Saffman & Schatzman [94]. It is instructive to compare our solutions with those of Saffman & Schatzman [94]. We reparametrise our solutions to emulate their presentation for means of effective comparison. Figure 2 of Saffman & Schatzman [94] shows the speed $U$ against the area of the vortex patches making up the street for several fixed aspect ratios $\kappa$, defined to be

$$\kappa = \frac{h}{L}, \tag{3.99}$$

where $h$ is the vertical separation of the vortex centroids in the two rows. Figure 3 of Saffman & Schatzman [94] shows the quantity $D$ against vortex patch area for the same set of aspect ratios. The quantity $D$ is a measure of the streamwise momentum flux of the fluid (with the contribution from the vortices neglected):

$$D = -\frac{1}{2}\mathrm{Im}\left[\int_{-\mathrm{i}\infty}^{\mathrm{i}\infty}(u - U - \mathrm{i}v)^2 dz\right]. \tag{3.100}$$

The contour of integration can be taken to be any path from $-\mathrm{i}\infty$ to $\mathrm{i}\infty$ which does not intersect the hollow vortices. Note that the integral in (3.100) is defined in a stationary frame of reference (and not in the co-travelling frame with the hollow vortices).

The perimeter of the hollow vortex which is the image of $|\zeta| = \rho$ under $z(\zeta)$ is given by

$$\oint_{|\zeta|=\rho} ds = \oint_{|\zeta|=\rho} |z_\zeta(\zeta')d\zeta'|\,. \tag{3.101}$$

Here, $ds$ denotes an element of arc length on $|\zeta| = \rho$. To enforce the desired aspect ratio of the street $\kappa$, we must compute the imaginary part of the centroid of the hollow vortex

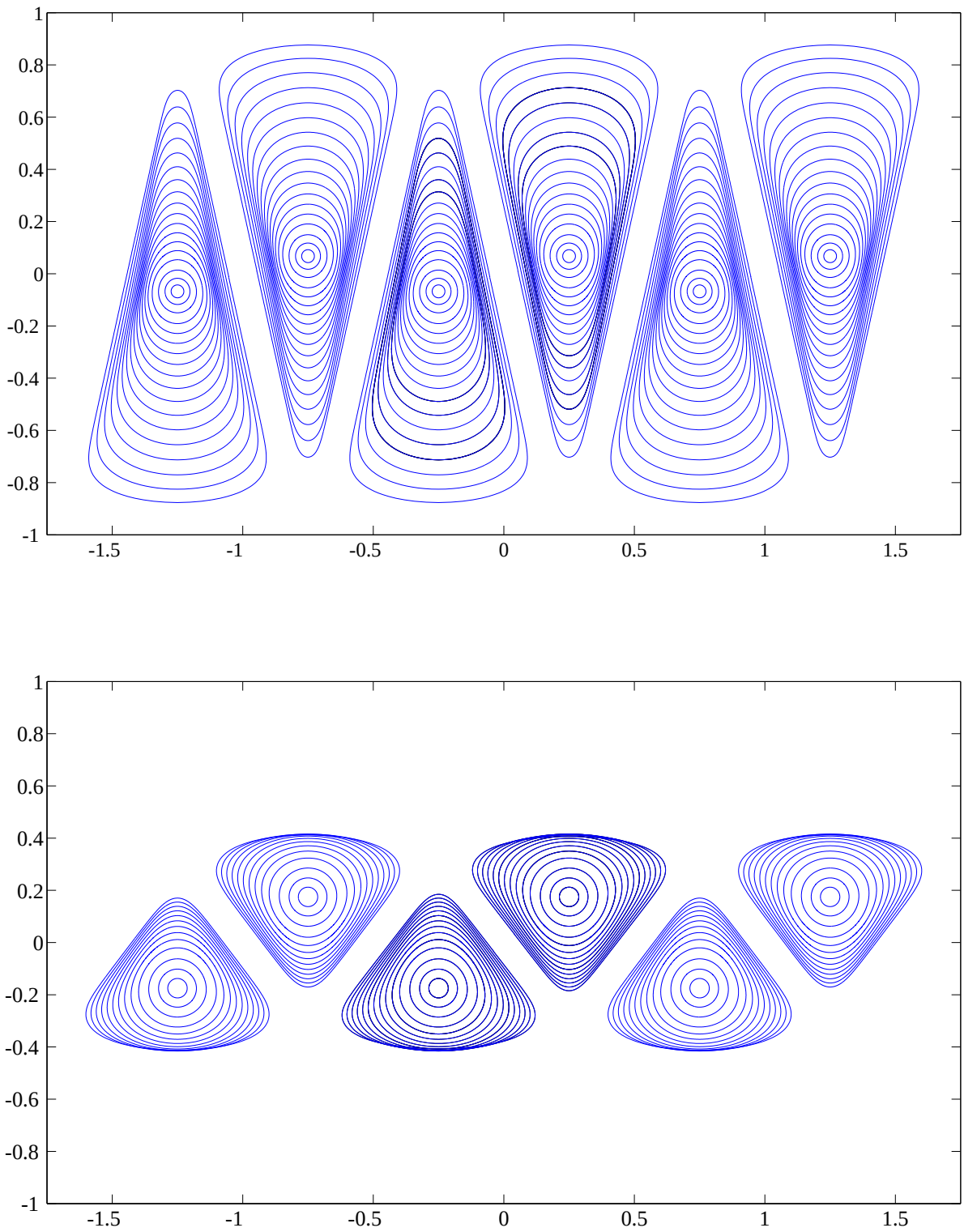


Figure 3.8: Three periods of typical staggered hollow vortex streets, showing hollow vortices of different areas, with $U = 0.2$ [top] and $U = 0.4$ [bottom]. The different solutions have been superposed.

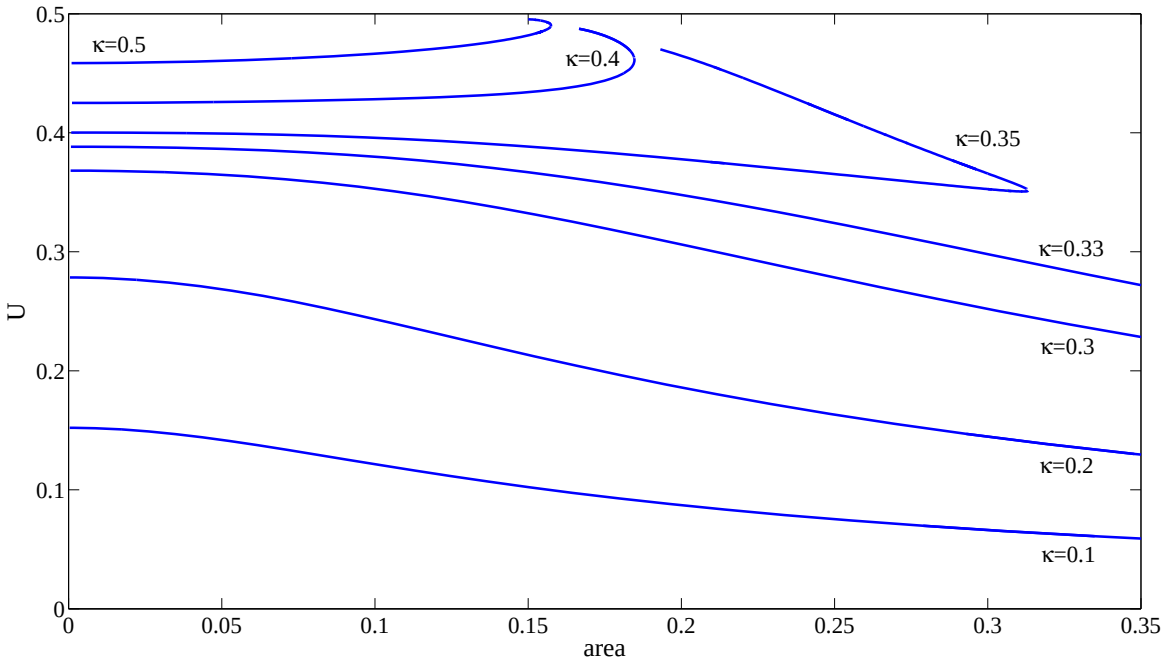


Figure 3.9: Graphs of $U$ against area for several fixed aspect ratios $\kappa$. This figure should be compared with Figure 2 of Saffman & Schatzman [94].

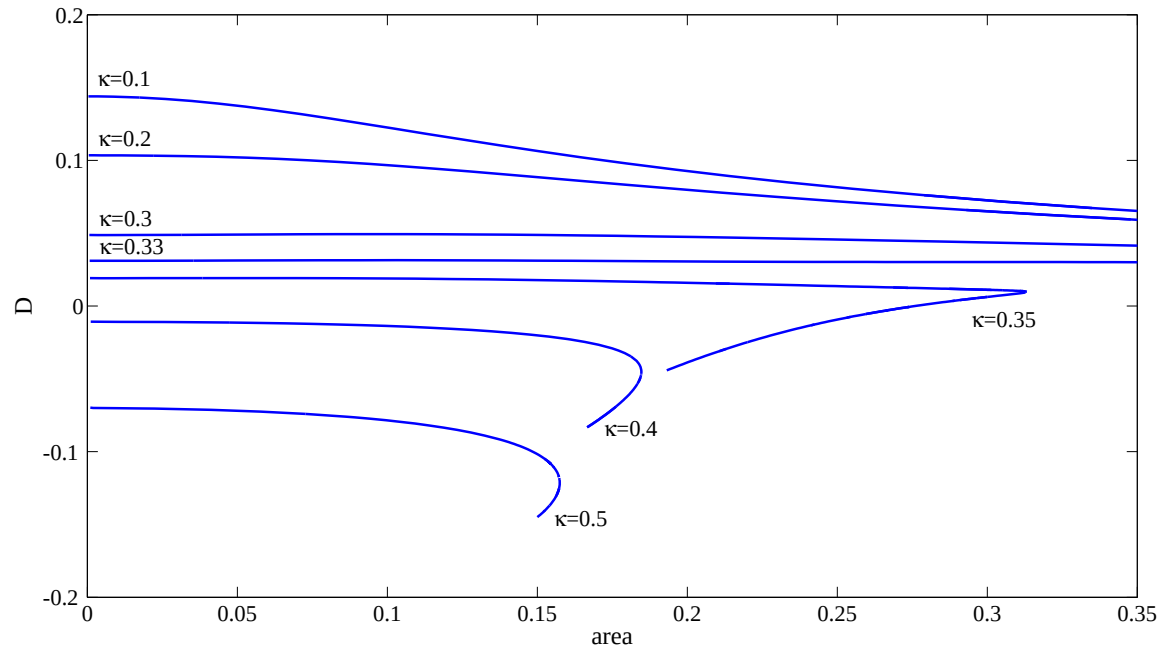


Figure 3.10: Graphs of $D$ against area for different aspect ratios $\kappa$. This figure should be compared with Figure 3 of Saffman & Schatzman [94].

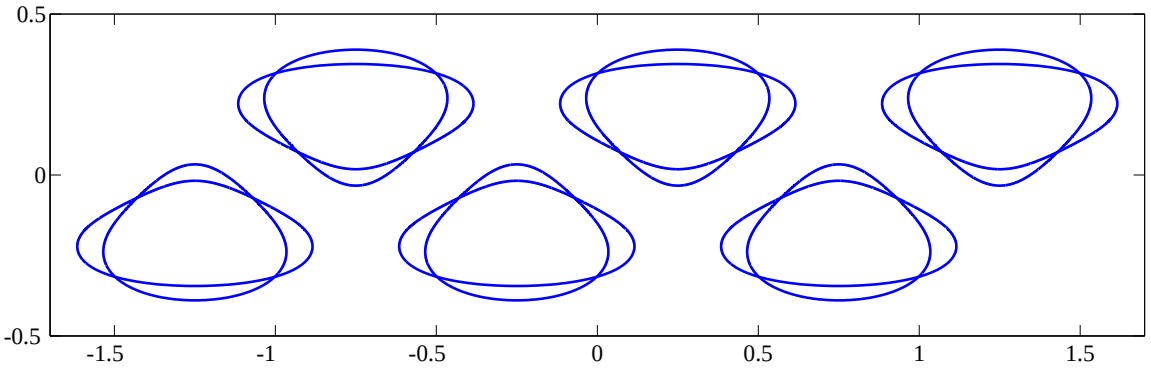


Figure 3.11: Non-uniqueness of solutions: two different hollow vortex streets are superposed, each comprising hollow vortices of area 0.175 and with aspect ratio $\kappa = 0.4$. The street with hollow vortices that are more extended in the streamwise direction travels faster ($U = 4817$, compared to $U = 0.4437$) but has a lower value of the momentum flux $D$.

which is the image of $|\zeta| = \rho$ under $z(\zeta)$, and set this equal to $\kappa/2$:

$$\mathrm{Im}\left[\oint_{|\zeta|=\rho} z(\zeta')|z_\zeta(\zeta')d\zeta'|\right] \Big/ \left(\oint_{|\zeta|=\rho} |z_\zeta(\zeta')d\zeta'|\right) = \kappa/2. \tag{3.102}$$

(3.102) follows from the general formula for the centroid of a planar shape $\mathcal{S}$:

$$\left(\iint_{\mathcal{S}} z dA\right) \Big/ \left(\iint_{\mathcal{S}} dA\right). \tag{3.103}$$

Here, $dA$ denotes an element of area of $\mathcal{S}$. However, since we do not have any *a priori* knowledge of the area of the hollow vortices, the formula in (3.103) reduces to

$$\left(\oint_{\partial\mathcal{S}} z ds\right) \Big/ \left(\oint_{\partial\mathcal{S}} ds\right). \tag{3.104}$$

Here, $\partial\mathcal{S}$ denotes the boundary of planar shape $\mathcal{S}$ and $ds$ is an element of arc length on $\partial\mathcal{S}$. Figure 3.9 shows graphs of $U$ against the area of the hollow vortices for various values of $\kappa$. The area of the hollow vortex which is the image of $|\zeta| = \rho$ under $z(\zeta)$ is given by

$$\left|\frac{1}{2\mathrm{i}}\oint_{|\zeta|=\rho} \overline{z(\zeta')} z_\zeta(\zeta')d\zeta'\right|. \tag{3.105}$$

(3.105) can be derived using Stokes' theorem. The speed of translation of the hollow vortices, whose centroids have been fixed, is retrieved using (3.82):

$$U = \left(K(\gamma_1/\alpha, \rho) - K(\gamma_1\alpha, \rho) - K(\gamma_1/\beta, \rho) + K(\gamma_1\beta, \rho)\right)^{-1}. \tag{3.106}$$

We find that there is a critical value of $\kappa$ between $\kappa = 0.33$ and $\kappa = 0.35$ signalling a dramatic change in the qualitative behaviour of these graphs. For $\kappa < 0.33$, the speed $U$ of the street for a given hollow vortex area is unique but, for $\kappa > 0.35$, the graphs turn around on themselves implying non-uniqueness of the street solutions for a given aspect ratio $\kappa$ and a given hollow vortex area. Figure 3.11 shows two different hollow vortex streets, of aspect ratio $\kappa = 0.4$, with area equal to 0.175. The street in which the hollow vortices are more extended in the streamwise direction travels with the greater speed ($U = 4817$ compared to $U = 0.4437$) but has a lower value of the momentum flux $D$. Saffman & Schatzman [94] find exactly the same qualitative behaviour for their streets of vortex patches: they report the critical aspect ratio to be $\kappa \approx 0.36$ which is very close to the value we have found. This is quite remarkable given that these two inviscid vortex models are so different. There could be special physical significance of this given that these similar aspect ratios have arisen in two different distributed vorticity models of staggered vortex streets; however at present, it is unknown what this significance could be. One interpretation could be a qualitative classification of two types of hollow vortex equilibria: one where as the hollow vortices grow, the shapes encroach on the neighbouring row, and the other where two continuous vortex 'layers' of equal and opposite circulation form (perhaps in a similar manner to the special limit of lens shaped touching vortices mentioned by Saffman & Szeto [98] for their street of vortex patches).

Figure 3.10 shows graphs of the quantity $D$ against hollow vortex area for various values of $\kappa$. We observe qualitatively similar behaviour to the graphs in Figure 3 of Saffman & Schatzman [94] and again notice that for $\kappa \geq 0.35$, the graphs turn around on themselves, reflecting the non-uniqueness of the solutions. It is worth mentioning that Saffman & Schatzman [94] also presented graphs of excess energy against vortex area for their streets of vortex patches; we have not computed such graphs but they would be expected to share a resemblance with those shown in Figure 4 of [7].

Each solution branch terminates owing to the Newton iteration no longer being able to converge. The solution branches of Saffman & Schatzman [94] were also terminated for

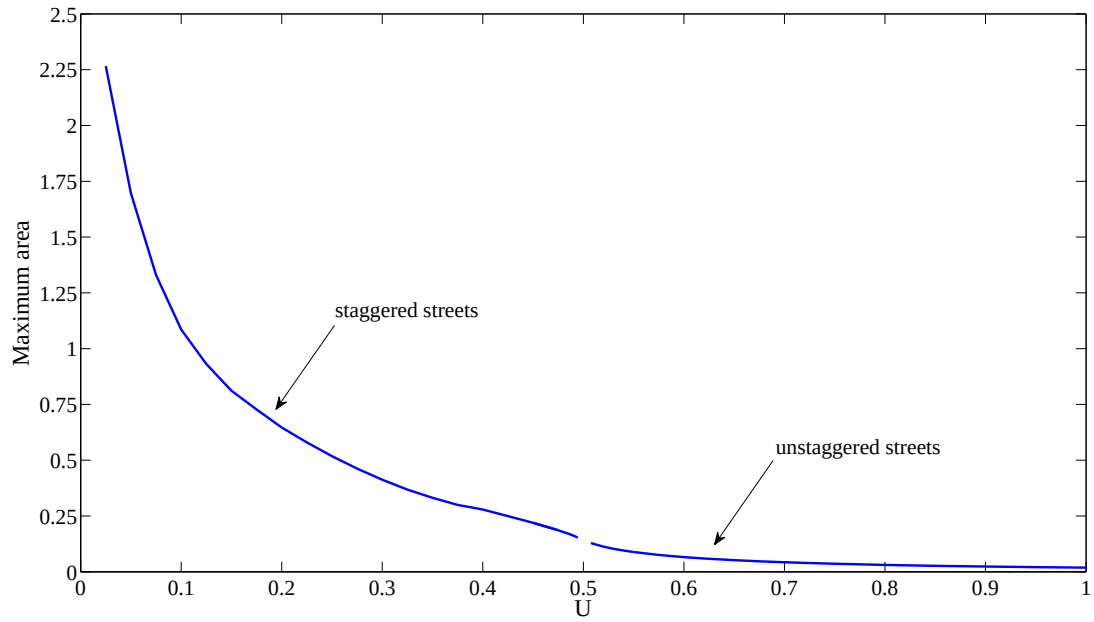


Figure 3.12: A graph of the maximum area of the hollow vortices in a street as a function of the speed of the street $U$, including both unstaggered and staggered varieties. It is difficult to find parameters for $U \approx 0.5$, but the graph appears to be a near-continuous function.

similar numerical reasons. We note that the hollow vortex shapes corresponding to the end of the solution branches do not possess any singularities and they remain univalent. Recall that we found solutions where the hollow vortices in each row had identical shapes and equal areas; in light of this, it could be possible that the solution branches continue into a different class of solution where, for example, the hollow vortices in each row do not have the same shape.

Finally, we found that there exists a maximum admissible area of the hollow vortices in a given staggered or unstaggered street for a fixed value of $U$. Figure 3.12 shows a graph of the maximum admissible area of the hollow vortices as a function of $U$, for both staggered and unstaggered streets. The graph appears to be a near-continuous and monotonically decreasing function. It was difficult to find solutions in the vicinity of $U = 0.5$; hence the small 'gap' in the graph. Saffman & Schatzman [94] also found similar regions of parameter space where convergence of their numerical scheme was hard to achieve.

## 3.5 Summary

After re-deriving the solution, in a different but equivalent form, for a single row of hollow vortices in unbounded fluid due to Baker, Saffman & Sheffield [7] using new mathematical techniques, we presented new classes of analytical solutions describing steadily translating von Kármán streets of hollow vortices, in staggered and unstaggered configurations. We solved this free boundary problem by generalising the approach we used to resolve the single row: we took a single period window of the configuration and, by using free streamline and conformal mapping theory, determined the relative equilibrium shapes of the two hollow vortex boundaries. The periodicity of the street structure was incorporated into our model by the introduction of a branch cut in the preimage domain whose two sides map to the two edges of the period window (and whose precise shapes are irrelevant). The use of conformal circular slit mappings was essential to constructing the functions we needed. We found a concise formula for our conformal map as an explicit indefinite integral whose integrand is expressed in terms of the Schottky-Klein prime function associated with the preimage concentric annulus, and is fully determined with the knowledge of just two geometrical parameters to be found as part of the solution. The solutions we have presented in this chapter are believed to be the first analytical solutions for von Kármán vortex streets with distributed vorticity; consequently, we expect them to arise in many future modelling applications.

We were able to reveal an array of features about hollow vortex streets from our solutions. From the plots illustrating the shapes of the free boundaries, we observed remarkable similarities between our staggered hollow vortex street solutions and experimentally-observed staggered vortex streets such as those shown in photographs in Van Dyke's monograph [114]. For the unstaggered configurations, we observed an increased flattening of the free boundaries in the regions where the hollow vortices are closest together. This was a characteristic found by Pocklington [85] for a co-travelling hollow vortex pair and indeed, the unstaggered hollow vortex street is a precisely a singly periodic array of Pocklington pairs. We then undertook a comparison of our staggered hollow vortex street solutions with the staggered vortex patch street solutions found by Saffman & Schatzman [94] by plotting graphs of streamwise fluid momentum flux and speed of translation against area. We found that there is a critical aspect ratio of the street, in both our model and the model of Saffman & Schatzman [94], of approximately 0.34-0.36, which has special significance for the equilibria and also determines whether or not there is non-uniqueness in the solutions.

# Chapter 4

# Hollow vortices in an infinite channel

## 4.1 Introduction

This chapter is devoted to the analysis of two different hollow vortex configurations in an infinite channel with straight, parallel-sided, impenetrable walls. We examine first the situation of a co-travelling hollow vortex pair in a channel. This free boundary problem turns out to exhibit similar mathematical features to the von Kármán hollow vortex street problem. We then extend our analysis to investigate a single row of hollow vortices in a channel. This problem requires the use of special conformal mappings known as polycircular arc mappings. As in Chapter 3, we will employ free streamline theory in combination with conformal mapping ideas in order to find analytical solutions which will reveal the shapes of the hollow vortex boundaries in our two chosen configurations set in the infinite channel. Given that these two free boundary problems are both set in infinite channels, the fluid flows to which they pertain are examples of so called 'wall-bounded flows' and as such, are expected to exhibit interesting physical features as well as requiring a special mathematical treatment.

In Chapter 3, our approach was to find separate expressions for the complex potential $W(\zeta)$ and the complex velocity function $dw/dz$, and from these, apply the chain rule to determine the conformal mapping $z(\zeta)$. This approach proved to be particularly expedient given that formulae for $W(\zeta)$ and $dw/dz$ were constructed in a straightforward manner using conformal slit mappings. We shall adopt the same approach in this chapter in order to solve our two free boundary problems. Also central to our approach in Chapter 3 was the introduction of a branch cut in the preimage circular domain. This served the primary purpose of incorporating the intrinsic periodicity of the configuration into our model, and also af-

forded us some analytical simplifications; for the same reasons, we shall again employ this mathematical technique of using branch cuts in this chapter. The solutions we present in this chapter for the single row of hollow vortices in the channel appear to be the first of their kind.

## 4.2 Background

To construct the complex potential for ideal fluid flows involving point vortices in infinite channels, the so-called 'method of images' (Acheson [2]) is usually adopted to produce an image system in free space through a series of successive reflections of the original system in the two channel walls; consequently, the two channel walls are guaranteed to be streamlines of the flow. Glauert [51] used the method of images in this way to derive an estimate for the reduction in the velocity of point vortices in a von Kármán street in an infinite channel due to the effects of the channel walls. The method of images was also the cornerstone of the approach by Rosenhead [92]. He analysed the von Kármán point vortex street in a channel, in both staggered and unstaggered configurations, and found analytical expressions for the complex potentials for both these systems, determined the speed of translation of the streets, and found explicit equations for the streamlines, using elliptic function theory. Greengard [55] has devised a fast numerical algorithm to calculate planar potential flows in infinite channels. He used the method of images to deduce an expression for the velocity field induced by a point vortex in an infinite channel and consequently, the associated streamfunction. Knowledge of these allowed him to develop the algorithm, based on recursive subdivisions of space and multipole expansions, in which the method of images also plays a central role.

The methods we will use to solve the free boundary problems of this chapter are not associated in any way with the method of images. Unlike point vortices, vortices with distributed vorticity intrinsically have an area and a boundary shape. In point vortex problems set in an infinite channel, there is of course no notion of size associated with the point vortices (point vortices have no area): the two length scales in these problems are the channel width and the distance of the point vortex to a channel wall. By considering the hollow vortex analogues of these point vortex problems in infinite channels, we see that there are now three length scales which feature: the channel width, the distance of the hollow vortex centroid to a channel wall and the area of the hollow vortex. The tantalising question fuelling our study into the free boundary problems of this chapter is how introducing a distributed vor-

ticity structure into a confined geometry has an effect on the shape of its free boundary. By considering the pair of hollow vortices in a channel, we are also motivated in devising an idealised mathematical model of a vortex ring travelling along a tube: the two-dimensional analogue of this problem is precisely our free boundary problem for a co-travelling pair of hollow vortices in a channel.

Two of the earliest works on hollow vortices are directly relevant to the free boundary problems we shall tackle in this chapter. Michell [77] used Schwarz-Christoffel methods and elliptic functions to derive an expression for the conformal map determining the shape of the free boundary of a single hollow vortex in an infinite channel. An interesting feature of this hollow vortex configuration is that it is stationary for all time and does not propagate along the channel. Pocklington [85] also used Schwarz-Christoffel methods and elliptic function theory to derive the conformal map for a steadily translating pair of hollow vortices in free space. Crowdy, Llewellyn Smith & Freilich [37] have recently re-derived this solution due to Pocklington using mathematical methods analogous to those that we shall use in this chapter. For this configuration, the pair of hollow vortices translates at constant speed parallel to their axis of symmetry, without change of form. We will make connections with both these classical solutions of Michell [77] and Pocklington [85]. A very recent study by Zannetti & Lasagna [128] replaces the stagnation points associated with hollow vortex pairs by so-called 'Chaplygin cusps' or finite-area regions of stagnant fluid. They have been able to determine the shapes of a pair of hollow vortices in a channel but their approach is different to ours. (This paper appeared in the literature after the work in this chapter was completed).

Other studies pertaining to vortex dynamics in channel geometries include the following. Giannakidis [50] has undertaken a numerical study into the effects of placing a Sadovskii vortex, which is a vortex patch bounded by a vortex sheet, in a channel containing ideal fluid. This type of steady planar flow also goes by the name of Prandtl-Batchelor flow, and the hollow vortex is a special type of Sadovskii vortex. Govorukhin, Morgulis & Vladimirov [53] have studied in detail the dynamics of planar inviscid incompressible flows in a straight channel of finite-length, focusing on the effects of boundary conditions on the vorticity dynamics. Yu et al [126] have studied vortices in superconducting channels with periodic constrictions, and Suzuki & Colonius [108] have devised an inverse-imaging method using a least-squares algorithm for the detection of a point vortex in ideal fluid in a channel.

Finally, it is worth highlighting some studies involving point vortices and vortex patches evolving around gaps in walls. Johnson & McDonald [62] have looked into point vortex and vortex patch dynamics near an infinitely long barrier with multiple gaps. Crowdy & Marshall [30] employed Kirchhoff-Routh theory to analyse the dynamics of a point vortex in fluid domains bounded by straight walls with multiple gaps. Elcrat, Hu & Miller [43] determined the equilibrium configurations of point vortices for flow past objects, such as an inclined flat plate, in an infinite channel.

## 4.3 Hollow vortex pair in an infinite channel

We first consider the case of a pair of hollow vortices in an infinite channel. We shall present a method of solution to this free boundary problem which is conceptually different to that of Zannetti & Lasagna [128].

### 4.3.1 Formulation of problem

In a physical $z = (x + \mathrm{i}y)$-plane, consider an infinite channel of width $L$ with impenetrable walls at $x = \pm L/2$. We will seek solutions for which a hollow vortex pair is steadily translating along the channel in the $y$-direction parallel to the walls of the channel with speed $U$. In a co-travelling frame of reference, one hollow vortex is assumed to have its centroid at $x = c$ and to have circulation $-\Gamma$ (where $\Gamma > 0$) with the other hollow vortex assumed to have its centroid at $x = -c$ with circulation $\Gamma$. Figure 4.1 shows a schematic of this configuration.

Consider a conformal mapping $z(\zeta)$ from a concentric annulus $\rho < |\zeta| < 1$ to the fluid region occupying the infinite channel exterior to the two hollow vortices. Let the circles $|\zeta| = 1$ and $|\zeta| = \rho$ map to the two hollow vortex boundaries in the channel. Let the two points $\zeta = \alpha$ and $\zeta = \beta$ lying inside this concentric annulus map to the two ends of the channel at infinity which we shall label by $\infty^{\pm}$. This means that we require

$$z(\zeta) = \frac{\mathrm{i}L}{2\pi}\log(\zeta - \alpha) + \text{locally analytic function}, \quad \zeta \to \alpha, \tag{4.1}$$

and

$$z(\zeta) = -\frac{\mathrm{i}L}{2\pi}\log(\zeta - \beta) + \text{locally analytic function}, \quad \zeta \to \beta. \tag{4.2}$$

It will be necessary to make some choice of branch cut between the two logarithmic branch

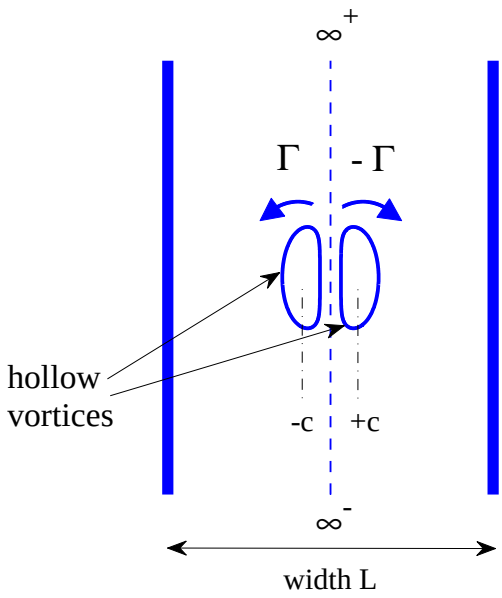


Figure 4.1: Schematic, in a co-travelling frame moving with the hollow vortices in a $z$-plane, of an infinite channel containing a pair of hollow vortices of equal and opposite circulation. The hollow vortex on the left has circulation $\Gamma$ and the hollow vortex on the right has circulation $-\Gamma$. The centroids of the hollow vortices are taken to be such that $\mathrm{Re}[z] = \pm c \in \mathbb{R}$. The two ends of the channel at infinity are denotes by $\infty^{\pm}$. The shapes of the hollow vortex boundaries are to be determined.

points at $\zeta = \alpha$ and $\zeta = \beta$, and it is natural to choose this so that the images under $z(\zeta)$ of the two sides of the branch cut map to the channel walls. The choice of this branch cut will be made later. Figure 4.2 shows a schematic of the preimage domain in the $\zeta$-plane.

It may seem surprising why we have chosen to map the two sides of the branch cut onto the channel walls. The reason for this becomes apparent if we consider an equivalent problem. If, instead of considering an infinite channel containing a pair of hollow vortices, we consider a singly periodic array of period windows (extending to $\infty^{\pm}$ and each containing a pair of hollow vortices), the problem now has an in-built periodicity structure and is analogous to the mathematical framework introduced in Chapter 3. The two problems are equivalent because, in the infinite channel case, the channel walls are streamlines, whilst in the singly periodic case, the straight vertical edges of a typical period window are precisely the same streamlines. For the case of the pair of hollow vortices in a channel, there is no periodicity in the problem, but when interpreted as a singly periodic array of hollow vortex pairs in free space, we can view the two sides of the branch cut mapping to the edges of a typical period window (moving through the branch cut corresponds to moving into a neighbouring period window) or, equivalently, the two channel walls.

### 4.3.2 Function $W(\zeta)$

We shall work in the co-travelling frame with the hollow vortex pair in which the configuration is steady and the hollow vortices assume a state of relative equilibrium with no change of form. Let complex potential associated with the flow in the co-travelling frame be $w(z)$. Introduce the composition

$$W(\zeta) = w(z(\zeta)). \tag{4.3}$$

The circulations around the two hollow vortices are $\pm\Gamma$; this means that

$$\oint_{|\zeta|=1} d[W(\zeta)] = -\oint_{|\zeta|=\rho} d[W(\zeta)] = -\Gamma, \tag{4.4}$$

where both $|\zeta| = 1$ and $|\zeta| = \rho$ are positively oriented in the anticlockwise direction. As $z \to \infty^{\pm}$, we require

$$w(z) = \mathrm{i}Uz + \text{locally analytic function}. \tag{4.5}$$

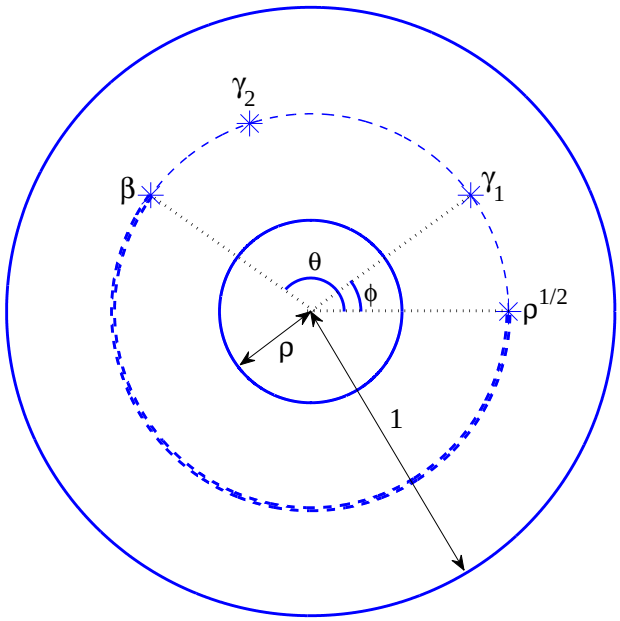


Figure 4.2: Schematic of the preimage circular domain in the $\zeta$-plane. The circles $|\zeta| = 1$ and $|\zeta| = \rho$ map to the two hollow vortex boundaries under the map $z(\zeta)$. The branch cut joining $\zeta = \sqrt{\rho}$ and $\zeta = \beta$ (the preimages of $\infty^{\pm}$) on $|\zeta| = \sqrt{\rho}$ is shown by a dashed line. The preimages of the two stagnation points on $|\zeta| = \sqrt{\rho}$ are labelled by $\zeta = \gamma_1$ and $\zeta = \gamma_2$.

Apart from this simple pole at infinity, $w(z)$ is an analytic function everywhere in the fluid region exterior to the two hollow vortices. In light of (4.1), (4.2) and (4.5), we require

$$W(\zeta) = -\frac{LU}{2\pi}\log(\zeta-\alpha) + \text{locally analytic function}, \quad \zeta \to \alpha, \tag{4.6}$$

and

$$W(\zeta) = \frac{LU}{2\pi}\log(\zeta-\beta) + \text{locally analytic function}, \quad \zeta \to \beta. \tag{4.7}$$

Function $W(\zeta)$ must also satisfy

$$\mathrm{Im}[W(\zeta)] = \text{constant} \tag{4.8}$$

on both circles $|\zeta| = \rho$ and $|\zeta| = 1$, as well as on the two sides of the branch cut, thereby ensuring that the two hollow vortex boundaries and the two channel walls are streamlines of the flow.

By using similar arguments to those presented in Chapter 3 to construct function (3.60), we claim that function $W(\zeta)$ is

$$W(\zeta) = -\frac{\mathrm{i}\Gamma}{2\pi}\log\zeta - \frac{LU}{2\pi}\log\chi(\zeta;\alpha,\beta), \tag{4.9}$$

where the conformal radial slit mapping $\chi(\zeta;\alpha,\beta)$ of (2.60), in the present case, is given by

$$\chi(\zeta;\alpha,\beta) = \frac{P(\zeta/\alpha,\rho)P(\zeta\overline{\alpha},\rho)}{P(\zeta/\beta,\rho)P(\zeta\overline{\beta},\rho)}. \tag{4.10}$$

Note that $\chi(\zeta;\alpha,\beta)$ has a simple zero at $\zeta = \alpha$. Straightforward manipulations using the relations (2.31) can be used to show that $\arg[\chi(\zeta;\alpha,\beta)] =$ constant on both $|\zeta| = 1$ and $|\zeta| = \rho$. It can be shown that $\chi(\zeta;\alpha,\beta)$ maps $|\zeta| = 1$ and $|\zeta| = \rho$ onto two finite-length radial slits emanating from the origin in the complex $\chi$-plane.

Due to the presence of the radial slit mapping (4.10) in (4.9), (4.8) is clearly satisfied on $|\zeta| = 1$ and $|\zeta| = \rho$. It also has the required behaviours (4.6) and (4.7) near $\zeta = \alpha$ and $\zeta = \beta$. It changes by $\Gamma$ as either $|\zeta| = 1$ or $|\zeta| = \rho$ is traversed in an anticlockwise sense thereby producing the required circulations (4.4) around the hollow vortices. We may choose $\zeta = \alpha$ to be on the positive real axis by the remaining rotational freedom of the Riemann-Koebe mapping theorem and, in order to enforce the required left-right

symmetry about the vertical channel centreline, we take

$$\alpha = \sqrt{\rho}. \tag{4.11}$$

Then

$$\beta = \sqrt{\rho}\mathrm{e}^{\mathrm{i}\theta} \tag{4.12}$$

where $\theta \in \mathbb{R}$ will need to be determined.

### 4.3.3 Function $dw/dz$

The complex velocity function needs to be analytic and single-valued in the fluid region exterior to the two hollow vortices. Based on the problem of a co-travelling point vortex pair in an infinite channel (see Appendix C), we expect two stagnation points at $y = \pm d$ lying on the channel centreline $x = 0$; this implies that the preimages of this pair of stagnation points will lie on $|\zeta| = \sqrt{\rho}$. Thus $dw/dz$ will have two simple zeroes:

$$\frac{dw}{dz}(\gamma_1) = \frac{dw}{dz}(\gamma_2) = 0. \tag{4.13}$$

Here, the preimages of the two stagnation points have been labelled by $\zeta = \gamma_1$ and $\zeta = \gamma_2$. As before, Bernoulli's theorem implies that

$$\left|\frac{dw}{dz}\right| = \text{constant} \tag{4.14}$$

on both $|\zeta| = 1$ and $|\zeta| = \rho$. We also require $dw/dz$ to be $L$-periodic across the channel.

Consider the function

$$\frac{dw}{dz} = \frac{R\eta(\zeta;\gamma_1)\eta(\zeta;\gamma_2)}{\zeta} \tag{4.15}$$

which has been derived using similar arguments to those presented in Chapter 3. Here, $R \in \mathbb{C}$ is a constant, and $\eta(\zeta;\gamma)$ is the bounded circular slit map as in (3.39). Note that this complex velocity function (4.15) has the same functional form as the complex velocity function (3.76) for the hollow vortex street. This function has constant modulus on $|\zeta| = 1$ and $|\zeta| = \rho$, and two simple zeroes at $\zeta = \gamma_1$ and $\zeta = \gamma_2$, as required. It is analytic and single-valued in $\rho < |\zeta| < 1$ and so it is invariant as either $\zeta = \sqrt{\rho}$ or $\zeta = \beta$ is encircled, and hence $L$-periodic across the channel. The reason for the factor of $\zeta$ in the denominator is the same as that given in Chapter 3 for von Kármán hollow vortex streets.

The parameters $\zeta = \gamma_1$ and $\zeta = \gamma_2$ are two solutions in $\rho < |\zeta| < 1$ of the equation

$$\frac{dW}{d\zeta}(\zeta) = 0, \tag{4.16}$$

which, on use of (2.42) and (4.9), can be expressed as

$$K(\gamma_j/\sqrt{\rho}, \rho) + K(\gamma_j\sqrt{\rho}, \rho) - K(\gamma_j/\beta, \rho) - K(\gamma_j\overline{\beta}, \rho) = -\frac{\mathrm{i}\Gamma}{LU}, \quad j = 1, 2. \tag{4.17}$$

Since

$$\frac{dw}{dz} \to \mathrm{i}U, \quad z \to \infty^{\pm}, \tag{4.18}$$

we must have

$$\frac{R\eta(\alpha;\gamma_1)\eta(\alpha;\gamma_2)}{\alpha} = \frac{R\eta(\beta;\gamma_1)\eta(\beta;\gamma_2)}{\beta} = \mathrm{i}U. \tag{4.19}$$

One of the equations in (4.19) can be used to determine the value of $R$; the velocity field then follows from (4.15) once a particular choice of branch cut between $\zeta = \sqrt{\rho}$ and $\zeta = \beta$ is made. This choice of branch cut is discussed later.

### 4.3.4 Conformal map $z(\zeta)$

Using similar arguments to those presented in Chapter 3, it is straightforward to show that the function $\zeta W_\zeta(\zeta)$ is a loxodromic function. It can be argued that another representation of $\zeta W_\zeta(\zeta)$ is given by

$$\zeta W_\zeta(\zeta) = \mathcal{B}\frac{P(\zeta/\gamma_1, \rho)P(\zeta\overline{\gamma_1}, \rho)P(\zeta/\gamma_2, \rho)P(\zeta\overline{\gamma_2}, \rho)}{P(\zeta/\sqrt{\rho}, \rho)P(\zeta\sqrt{\rho}, \rho)P(\zeta/\beta, \rho)P(\zeta\overline{\beta}, \rho)}, \tag{4.20}$$

where $\mathcal{B} \in \mathbb{C}$ is a constant. By free streamline theory, it follows on use of (4.15) and (4.20) that

$$\frac{dz}{d\zeta} = \mathcal{A}\frac{P^2(\zeta\overline{\gamma_1}, \rho)P^2(\zeta\overline{\gamma_2}, \rho)}{P(\zeta/\sqrt{\rho}, \rho)P(\zeta\sqrt{\rho}, \rho)P(\zeta/\beta, \rho)P(\zeta\overline{\beta}, \rho)}, \tag{4.21}$$

where $\mathcal{A} \in \mathbb{C}$ is a constant. Thus, an integral for the conformal mapping $z(\zeta)$ is

$$z(\zeta) = \mathcal{A}\int_{\zeta_0}^{\zeta} \frac{P^2(\zeta'\overline{\gamma_1}, \rho)P^2(\zeta'\overline{\gamma_2}, \rho)}{P(\zeta'/\sqrt{\rho}, \rho)P(\zeta'\sqrt{\rho}, \rho)P(\zeta'/\beta, \rho)P(\zeta'\overline{\beta}, \rho)}d\zeta'. \tag{4.22}$$

Here, $\zeta_0 \in \mathbb{C}$ is an arbitrary point inside the annulus $\rho < |\zeta| < 1$. Remarkably, (4.22) shares the same functional form as the conformal map (3.78) governing the shapes of the hollow vortices in a von Kármán street. The value of the pre-multiplicative constant $\mathcal{A}$ in

(4.22) is found *a posteriori* by insisting that the residue of $dz/d\zeta$ at $\zeta = \sqrt{\rho}$ is $\mathrm{i}L/2\pi$ as required by (4.1). An explicit expression for it is given by

$$\mathcal{A} = -\frac{\mathrm{i}L}{2\pi}\left(\frac{\hat{P}(1,\rho)P(\rho,\rho)P(\sqrt{\rho}/\beta,\rho)P(\sqrt{\rho}\overline{\beta},\rho)}{\sqrt{\rho}P^2(\sqrt{\rho}\overline{\gamma_1},\rho)P^2(\sqrt{\rho}\overline{\gamma_2},\rho)}\right), \tag{4.23}$$

where function $\hat{P}(\zeta,\rho)$ is as in (3.80).

### 4.3.5 Characterisation of the solutions

We fix

$$L = \Gamma = 1. \tag{4.24}$$

This corresponds to setting one of the length scales of the problem (i.e. the width of the channel) and the time scale of the motion, respectively. The analogous problem of a pair of point vortices in an infinite channel admits a one-parameter family of equilibrium solutions (see Appendix C); we shall take this parameter to be $c \in \mathbb{R}$, where the centroids of the two hollow vortices are

$$x = \pm c. \tag{4.25}$$

This corresponds to setting the second length scale of the problem. We additionally expect to be able to dictate the area of the hollow vortices; this then sets the third length scale of the problem. As in Chapter 3, a natural way to do this is to specify the value of $\rho$. Once all these parameters have been determined, the translation speed $U$ of the hollow vortices will follow from (4.17):

$$U = \left(\mathrm{i}\left(K(\gamma_1/\sqrt{\rho},\rho) + K(\gamma_1\sqrt{\rho},\rho) - K(\gamma_1/\beta,\rho) - K(\gamma_1\beta,\rho)\right)\right)^{-1}. \tag{4.26}$$

The constant $\zeta_0$ in the conformal map (4.22) reflects a translational degree of freedom which can be set arbitrarily and the mapping shifted by an appropriate constant *a posteriori*. We shall now proceed to examine the solution class with $c$ and $\rho$ as our two free real parameters.

Our general strategy in finding solutions is to choose a value $c$ for the hollow vortex centroids and then gradually increase the value of $\rho$ from zero in a standard continuation procedure. As in Chapter 3, we will focus on solutions where the hollow vortex pair have identical shapes and equal areas. Note that this is already intrinsic in our model due to the

symmetry in the preimage $\zeta$-plane through the circle $|\zeta| = \sqrt{\rho}$.

We have found that solutions for two hollow vortices of equal area and identical shape are given by the special parameter choices:

$$\beta = \sqrt{\rho}\mathrm{e}^{\mathrm{i}\theta}, \quad \gamma_1 = \sqrt{\rho}\mathrm{e}^{\mathrm{i}\phi}, \quad \gamma_2 = \frac{\sqrt{\rho}\beta}{\gamma_1} = \sqrt{\rho}\mathrm{e}^{\mathrm{i}(\theta-\phi)}. \tag{4.27}$$

Figure 4.2 shows the location of these parameters (4.27) in the preimage $\zeta$-plane. With these parameter choices (4.27), the images of the circles $|\zeta| = 1$ and $|\zeta| = \rho$ under the map (4.22) are reflections of each other through the vertical channel centreline between them. For a given $\rho$ and $c$, the two real parameters

$$\theta = \arg[\beta], \quad \phi = \arg[\gamma_2], \tag{4.28}$$

remain to be determined. Knowledge of these two real parameters will reveal the shapes of the hollow vortex boundaries. One condition to determine these parameters is

$$\mathrm{Re}\left[\oint_{|\zeta|=1} z_\zeta(\zeta')d\zeta'\right] = 0 \tag{4.29}$$

which is a necessary condition for the image of $|\zeta| = 1$ under $z(\zeta)$ to be a closed curve. Once (4.29) has been satisfied, the symmetry is such that the image of $|\zeta| = \rho$ is also a closed curve:

$$\mathrm{Re}\left[\oint_{|\zeta|=\rho} z_\zeta(\zeta')d\zeta'\right] = 0. \tag{4.30}$$

With the choice of parameters (4.27), it turns out to be automatic that

$$\mathrm{Im}\left[\oint_{|\zeta|=1} z_\zeta(\zeta')d\zeta'\right] = \mathrm{Im}\left[\oint_{|\zeta|=\rho} z_\zeta(\zeta')d\zeta'\right] = 0. \tag{4.31}$$

The other condition to be enforced is:

$$\mathrm{Re}\left[\oint_{|\zeta|=\rho} z(\zeta')|z_\zeta(\zeta')d\zeta'|\right] \Big/ \left(\oint_{|\zeta|=\rho} |z_\zeta(\zeta')d\zeta'|\right) = c. \tag{4.32}$$

This sets the real part of one of the hollow vortex centroids. Equations (4.29) and (4.32) can be readily solved using Newton's method.

It should be noted that thus far, we have not enforced the streamline conditions (4.8) on the

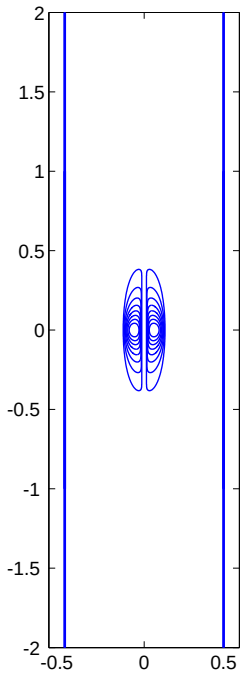


Figure 4.3: Superposition of co-travelling hollow vortex pairs in an infinite channel with centroids $\mathrm{Re}[z] = \pm c = 1/16$.

channel walls; indeed, we have not even determined the preimages of the channel walls in the $\zeta$-plane. We will now show that the channel walls correspond to the image of an arc of the circle $|\zeta| = \sqrt{\rho}$ under the conformal mapping $z(\zeta)$. It can be shown using the relations (2.31) that

$$\mathrm{Im}[W(\zeta)] = \text{constant} \tag{4.33}$$

on $|\zeta| = \sqrt{\rho}$. Recall that $\zeta = \sqrt{\rho}$ and $\zeta = \beta$ map to the two ends of the channel at infinity. In light of the left-right symmetry of the configuration in the $z$-plane, one arc of the circle $|\zeta| = \sqrt{\rho}$ between $\zeta = \sqrt{\rho}$ and $\zeta = \beta$ will map onto the channel centreline $x = 0$ joining $\infty^{\pm}$. (4.33) then immediately implies that the channel centreline $x = 0$ will indeed be a streamline of the flow, as required. The preimages of the stagnation points, $\zeta = \gamma_1$ and $\zeta = \gamma_2$, will lie on this arc. The second arc on $|\zeta| = \sqrt{\rho}$ joining $\zeta = \sqrt{\rho}$ and $\zeta = \beta$ will be taken to be our branch cut whose two sides will map to the channel walls (see Figure 4.2). It is then automatic from (4.33) that the two channel walls will indeed be streamlines of the flow, as required.

Figures 4.3-4.6 show infinite channels of unit width containing co-travelling hollow vortex pairs of varying areas. In each channel, the hollow vortex centroids are fixed at $\mathrm{Re}[z] = \pm c$,

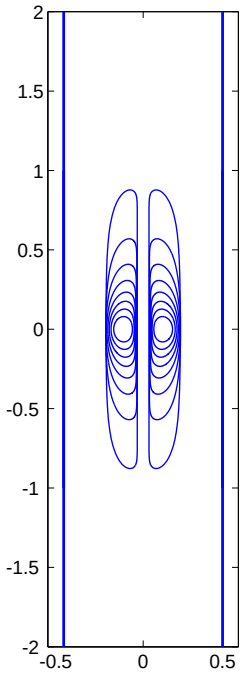


Figure 4.4: Superposition of co-travelling hollow vortex pairs in an infinite channel with centroids $\mathrm{Re}[z] = \pm c = 1/8$.

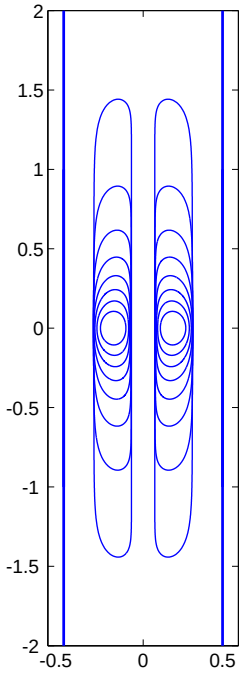


Figure 4.5: Superposition of co-travelling hollow vortex pairs in an infinite channel with centroids $\mathrm{Re}[z] = \pm c = 3/16$.

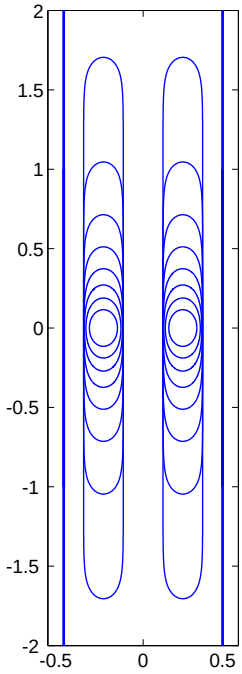


Figure 4.6: Superposition of co-travelling hollow vortex pairs in an infinite channel with centroids $\mathrm{Re}[z] = \pm c = 1/4$. These solutions for $c = 1/4$ correspond to the solutions due to Michell [77].

for some specified value of $c$. We have established that there exist solutions, corresponding to a distinct shape of hollow vortex, with a unique value of area, for each value of $\rho$. One interesting observation to make is that our solutions do not exhibit maximum area configurations; rather, the area of the hollow vortices appears to increase without bound as $\rho \to 1$. This is consistent with the results shown in Figure 4.8 which shows graphs of hollow vortex area as a function of $\rho$: the area of the hollow vortices, for a given value of $c$, is a monotonically increasing function of $\rho$. We also observe that the hollow vortex areas are smallest when the centroids are closest together, and are largest when the centroids are equi-distant to the channel centreline and to a channel wall. For small values of $\rho$, the hollow vortices are always found to be small and almost circular. We also remark that the hollow vortices in Figures 2 and 6 of Zannetti & Lasagna [128] look qualitatively the same as our solutions for similar hollow vortex areas and centroid locations; this is reassuring given that our mathematical approaches are different.

Pocklington [85] makes the observation that when a pair of co-travelling hollow vortices in free space are very close together, their boundary shapes are much flatter on their near

rather than on their remote sides. We observe this phenomenon when $c = 1/16$ and $c = 1/8$ in Figures 4.3, when the centroids are close together. These hollow vortex shapes indeed closely resemble those found by Pocklington [85]; this is to be expected when the centroids are close together because the hollow vortices are never close to the channel walls and should therefore appear qualitatively similar to their free space counterparts. Indeed, our solutions can be viewed as generalisations of the co-travelling hollow vortex pair due to Pocklington [85] to the infinite channel geometry.

The case when $c = 1/4$ is special (Figure 4.5). Here, each of the two centroids of the hollow vortices is equi-distant to both the channel centreline and to one of the channel walls. Since both the channel centreline and the channel walls are streamlines of the flow, the hollow vortex shapes in the case when $c = 1/4$ are precisely those obtainable from the solution due to Michell [77] for a single hollow vortex in an infinite channel. It should be possible to exactly superpose a solution of given area, obtained from the conformal map in [77], onto one of our solutions with the same area; however, due to a lack of notational explanation in his paper, we have been unable to do this.

We have also established that both the area and the hollow vortex centroids have an effect on the speed of translation of the hollow vortex pair along the channel. Figure 4.7 shows graphs for $c = 1/16, 1/8, 3/16$ of the ratio $U/U_p$ as a function of $\rho$, where $U_p$ is the speed of translation of a pair of point vortices in an infinite channel positioned at $\mathrm{Re}[z] = \pm c$:

$$U_p = \frac{1}{2}\cot(2\pi c). \tag{4.34}$$

The graph for $c = 1/4$ does not feature because the hollow vortex pair is stationary for all time, in the same way that the single hollow vortex considered by Michell [77] is. For each value of $c$, it is clear that

$$\lim_{\rho \to 0} \frac{U}{U_p} = 1, \tag{4.35}$$

as expected. For a fixed value of $c$, we observe that $U$ is a monotonically decreasing function with hollow vortex area; hollow vortex pairs with large areas will translate with a smaller speed. We also observe that the hollow vortex pairs whose centroids are closest together move along the channel faster than those whose centroids are spaced further apart.

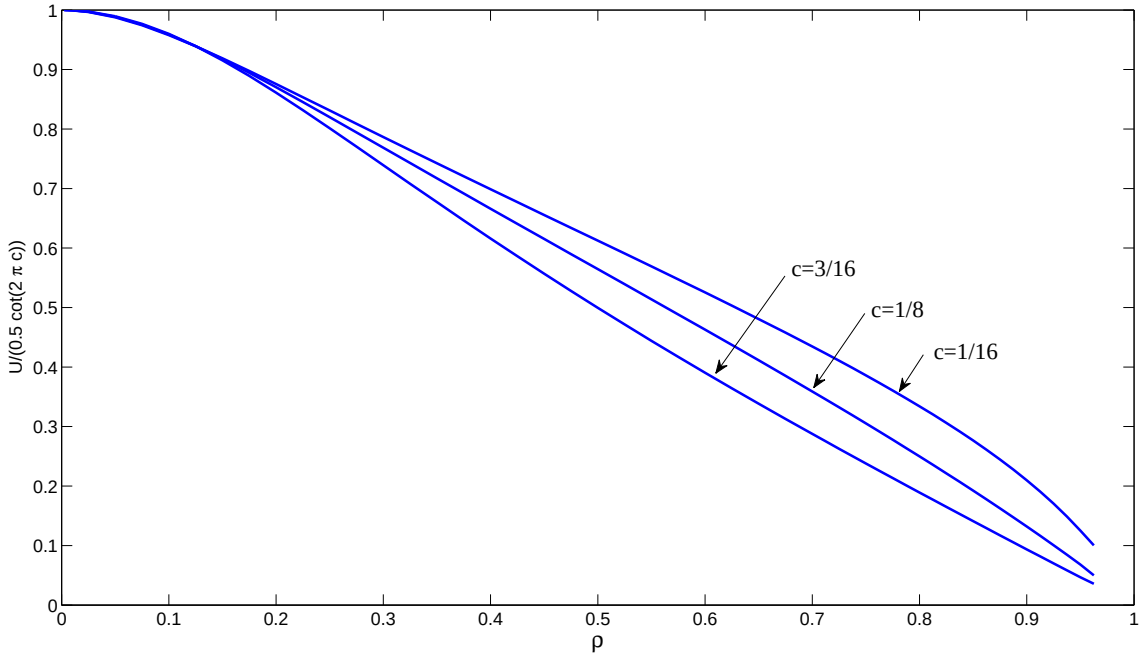


Figure 4.7: Graphs, for three different hollow vortex centroids $\mathrm{Re}[z] = \pm c = 1/16, 1/8, 3/16$, of the ratio of the speed of translation of the hollow vortex pair $U$ to the corresponding point vortex speed $\frac{1}{2}\cot(2\pi c)$ as a function of $\rho$. As expected, each graph is tending to unity in the limit as $\rho \to 0$. When $\mathrm{Re}[z] = \pm c = 1/4$, the hollow vortices are stationary.

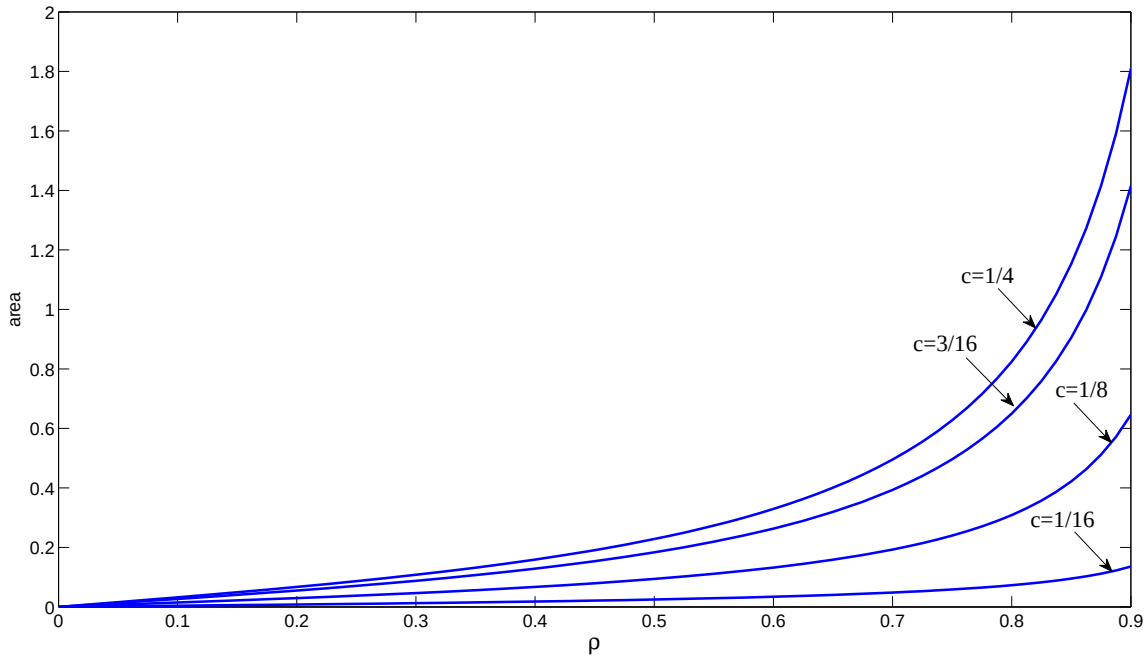


Figure 4.8: Graphs, for four different hollow vortex centroids $\mathrm{Re}[z] = \pm c = 1/16, 1/8, 3/16, 1/4$, of the area of the hollow vortices as a function of $\rho$. As $\rho \to 1$, the area of the hollow vortices grows without bound.

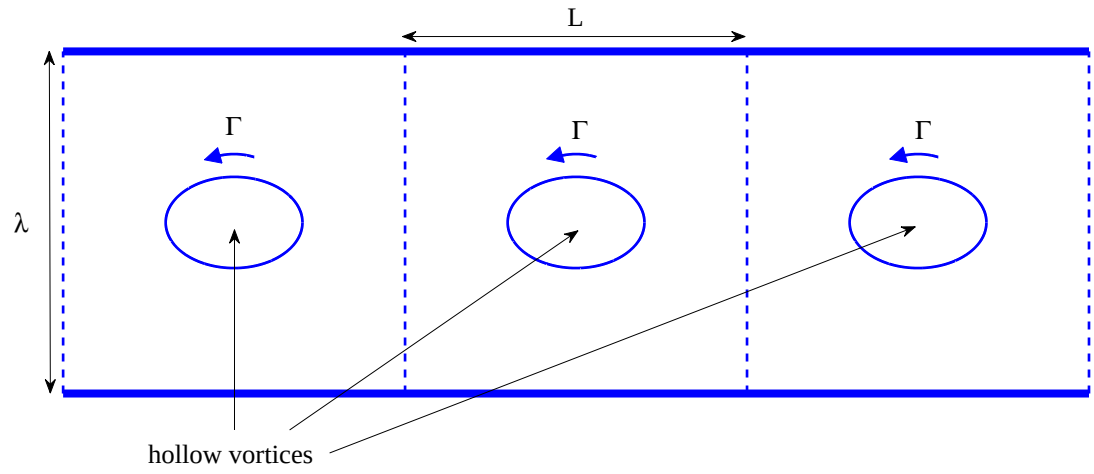


Figure 4.9: Schematic showing three periods of length $L$ of a row of hollow vortices, each of circulation $\Gamma$, in an infinite channel of width $\lambda$ in a $z$-plane. The horizontal channel walls are $\mathrm{Im}[z] = \pm y = \lambda/2$. Each of the hollow vortex centroids in this row lie on the channel centreline $\mathrm{Im}[z] = 0$. The shapes of the hollow vortex boundaries are to be determined.

## 4.4 Row of hollow vortices in an infinite channel

We shall now consider the case of a single row of hollow vortices, whose centroids are aligned along the channel centreline, in an infinite channel. In doing so, we will be considering generalisations of the works of both Michell [77] and Baker, Saffman & Sheffield [7]. The reader is referred to Appendix D for an overview of how the mathematical model we shall develop in the remainder of this chapter can be modified when the centroids of the hollow vortices are moved off the channel centreline.

### 4.4.1 Formulation of problem

In a physical $z = (x + \mathrm{i}y)$-plane, consider a horizontal parallel-sided channel whose two ends extend to infinity in both directions $\infty^{\pm}$ and which has a width $\lambda$. Let the impenetrable walls of the channel be the horizontal lines $y = \pm\lambda/2$ so that the channel centreline is $y = 0$. Let the centroids of the hollow vortices be located at $x = nL$, $n \in \mathbb{Z}$, so that $L$ be the period of the configuration i.e. the horizontal length between two neighbouring hollow vortex centroids on the channel centreline. Let the circulation of each of the hollow vortices

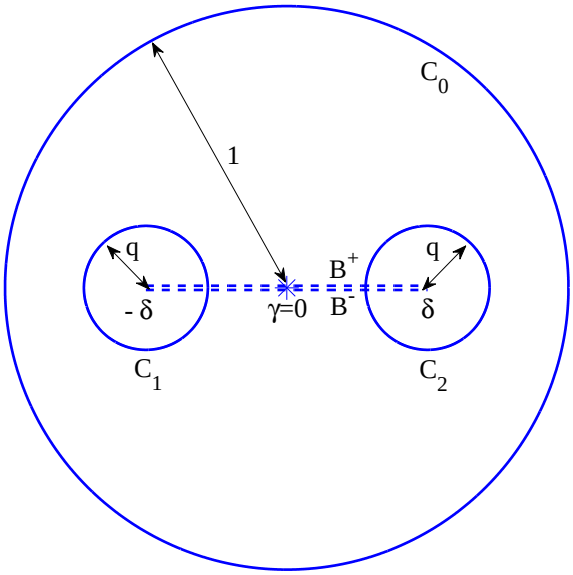


Figure 4.10: Schematic showing the preimage triply connected bounded circular domain $D_\zeta$ in the $\zeta$-plane. Under the conformal map $z(\zeta)$, the unit circle $C_0$ is taken to map to the hollow vortex boundary and the two interior circles $C_1$ and $C_2$ are taken respectively to map to the top and bottom horizontal channel walls of the period window. The branch cut joining the centres of $C_1$ and $C_2$ is shown as a dashed line. The two sides of this branch cut lying in the interior of $D_\zeta$ map to the two vertical edges of the period cell.

in the row be $\Gamma$. These hollow vortices in the row are expected to remain in equilibrium. Given this periodic structure, it suffices to consider a single period cell of the configuration: this cell contains one hollow vortex of finite-area with circulation $\Gamma$, and has the dimensions $L \times \lambda$. Figure 4.9 illustrates this arrangement.

Let $D_\zeta$ be the following triply connected bounded circular domain in a parametric $\zeta$-plane. Let the unit $\zeta$-circle be labelled $C_0$. Take the unit $\zeta$-disc and from it excise two smaller discs whose boundaries are the circles $C_1$ and $C_2$. Let the centre of $C_1$ be $-\delta$ and let the centre of $C_2$ be $+\delta$, where $\delta \in \mathbb{R}$. Owing to the up-down symmetry of the period cell about the channel centreline, let the radius of both $C_1$ and $C_2$ be $q$. Figure 4.10 shows a schematic of $D_\zeta$. In choosing this preimage domain $D_\zeta$, we have used up the three real degrees of freedom associated with the Riemann-Koebe mapping theorem. Let $\omega(\cdot,\cdot)$ denote the Schottky-Klein prime function associated with $D_\zeta$.

Consider a conformal mapping $z(\zeta)$ taking the interior of $D_\zeta$ to a single period cell of the

hollow vortex row in the channel. Our task is to determine the shape of the boundary of the hollow vortex in this period cell. Let the unit circle $C_0$ be mapped onto the boundary of the hollow vortex in the period cell, and let the interior circles $C_1$ and $C_2$ be mapped onto the top and bottom channel walls of the period cell. Note that traversing $C_0$ in an anticlockwise sense corresponds to traversing the boundary of the hollow vortex in a clockwise sense.

In order to capture the periodic structure of the row of hollow vortices in the channel, and uniquely define the conformal map $z(\zeta)$, we must make a choice of branch cut in $D_\zeta$. Since $C_1$ and $C_2$ map to the two channel walls of the period cell, the branch cut must link these two circles. The two sides of this branch cut, lying in the interior of $D_\zeta$, will map to the two straight vertical edges of the period cell of height $\lambda$. A $2\pi$ traversal of either $C_1$ or $C_2$ corresponds to moving a distance $L$ along a channel wall; encircling $C_1$ or $C_2$ by more than $2\pi$ corresponds to moving a distance $L$ along the wall and into the neighbouring period cell. In light of this, it is natural to take the branch cut along the real axis through the origin, joining the centres of $C_1$ and $C_2$ between $\zeta = -\delta$ and $\zeta = \delta$.

Rosenhead [92] has analysed von Kármán point vortex streets in an infinite channel. From Rosenhead's work, we are led to expect two stagnation points lying on the vertical edges of each of our period cells. Moreover, we expect both these stagnation points to lie on the channel centreline. In light of this, we expect the same point in $D_\zeta$, lying on the branch cut, to map to both stagnation points. Let the preimage in $D_\zeta$ of these two stagnation points be labelled $\zeta = \gamma \in \mathbb{R}$. For hollow vortices whose centroids lie on the channel centreline, it is clear from the symmetry that $\gamma = 0$ (see Figure 4.10).

### 4.4.2 Function $W(\zeta)$

Let the complex potential for the flow associated with the hollow vortex row in the channel be denoted by $w(z)$. We need the total circulation in the period cell to be $\Gamma$:

$$\oint_{\partial D} d[w(z)] = \Gamma. \tag{4.36}$$

Here, we denote $\partial D$ by the boundary of the period cell, i.e. the two horizontal walls and the two vertical edges, and is positively oriented in the anticlockwise direction. Introducing the composition

$$W(\zeta) = w(z(\zeta)), \tag{4.37}$$

we see that in the $\zeta$-plane, the integral (4.36) is

$$\oint_{C_1 \cup B^+ \cup C_2 \cup B^-} d[W(\zeta)] = \Gamma. \tag{4.38}$$

Here, $B^+$ denotes the top-side of the branch cut lying in the interior of $D_\zeta$ and $B^-$ denotes the under-side. There is a net zero contribution to this integral as both sides of the branch cut are traversed: this is due to cancellation owing to the opposite directions of integration. This is reflected by the fact that the fluid velocity is equal on the two vertical edges of the period cell; indeed, the fluid velocity is $L$-periodic in the $x$-direction. Consequently, the non-zero contribution to the integral in (4.38) must come from integrating around $C_1$ and $C_2$: recall the 'a-cycle' properties of the $v_j(\zeta)$ functions (2.7) which allow us to fulfil this requirement. We also require the two channel walls and the hollow vortex boundary to be streamlines:

$$\mathrm{Im}[W(\zeta)] = \text{constant} \tag{4.39}$$

for $\zeta \in C_0, C_1, C_2$.

We propose the following function for the complex potential:

$$W(\zeta) = \frac{\Gamma}{2}\left(v_1(\zeta) + v_2(\zeta)\right). \tag{4.40}$$

Given the up-down symmetry of the period cell about the channel centreline, we would expect an equal contribution to the total circulation in the period cell along the two channel walls; this explains the pre-multiplying constant $\Gamma/2$. It follows from the 'a-cycle' properties of the $v_j(\zeta)$ functions (2.7) that (4.40) indeed satisfies (4.38). From the properties (2.8) and (2.9), (4.40) is easily seen to have constant imaginary part on each of the boundary circles of $D_\zeta$. Taking a derivative of (4.40) with respect to $\zeta$ yields

$$\frac{dW}{d\zeta}(\zeta) = \frac{\Gamma}{2}\left(v_1'(\zeta) + v_2'(\zeta)\right). \tag{4.41}$$

Here, $v_j'(\zeta)$ means the derivative of $v_j(\zeta)$ with respect to $\zeta$. (4.41) is required to have a simple zero at $\zeta = 0$. Let us show that this is in fact the case. The 'a-cycle' properties of the $v_j(\zeta)$ functions (2.7) imply that

$$v_j(\zeta) = \frac{1}{2\pi \mathrm{i}} \log(\zeta - \delta_j) + \text{locally analytic function}, \quad j = 1, ..., M. \tag{4.42}$$

Differentiating (4.42) with respect to $\zeta$ implies

$$v_j'(\zeta) = \frac{1}{2\pi \mathrm{i}} \frac{1}{\zeta - \delta_j} + c_j + \text{locally analytic function}, \quad j = 1, ..., M, \tag{4.43}$$

where $c_j \in \mathbb{C}$ are constants. In the present case, we have $\delta_1 = -\delta$ and $\delta_2 = \delta$. Note that as $\zeta \to 0$, it follows from (4.43) that

$$v_1'(\zeta) = \frac{1}{2\pi \mathrm{i}\delta} + c_1 + \text{locally analytic function} \tag{4.44}$$

and

$$v_2'(\zeta) = -\frac{1}{2\pi \mathrm{i}\delta} + c_2 + \text{locally analytic function}, \tag{4.45}$$

where $c_1, c_2 \in \mathbb{C}$ are constants. But, given the symmetry of $D_\zeta$, it turns out that $c_1 = -c_2$. Thus, the simple zero of $dW/d\zeta$ at $\zeta = 0$ is intrinsic in (4.41).

### 4.4.3 Function $dw/dz$

Bernoulli's theorem implies that the fluid speed must be constant on the boundary of the hollow vortex:

$$\left| \frac{dw}{dz}(\zeta) \right| = Q_0, \quad \zeta \in C_0. \tag{4.46}$$

Here, $Q_0 \in \mathbb{R}$ is a positive constant. The fluid velocity $u - \mathrm{i}v$ on the two channel walls must be purely tangential to the walls; that is, the fluid velocity is purely real on the two channel walls:

$$v = -\mathrm{Im}\left[ \frac{dw}{dz}(\zeta) \right] = 0, \quad \zeta \in C_1, C_2. \tag{4.47}$$

We need $dw/dz$ to have a simple zero at $\zeta = 0$ in order to include the two stagnation points:

$$\frac{dw}{dz}(0) = 0. \tag{4.48}$$

We also require $dw/dz$ to be $L$-periodic in the $x$-direction.

In order to construct the complex velocity function, we appeal to a special class of conformal mappings known as polycircular arc mappings. The target domains of these maps are multiply connected regions whose boundaries consist of a union of circular arc segments.

Consider the following polycircular arc mapping:

$$\mathcal{S}(\zeta;R)=\frac{\omega(\zeta,-1)-R\omega(\zeta,1)}{\omega(\zeta,-1)+R\omega(\zeta,1)}, \tag{4.49}$$

where $R\in\mathbb{C}$ is a constant to be determined shortly. This conformal map can be constructed through the following composition:

$$\mathcal{S}(\zeta;R)=\mathcal{S}_2(\mathcal{S}_1(\zeta;R)), \tag{4.50}$$

where

$$\mathcal{S}_1(\zeta;R)=R\xi(\zeta;1,-1),\quad \mathcal{S}_2(\zeta)=\frac{1-\zeta}{1+\zeta}, \tag{4.51}$$

and $\xi(\zeta;1,-1)$ is the radial slit mapping of (2.62):

$$\xi(\zeta;1,-1)=\frac{\omega(\zeta,1)}{\omega(\zeta,-1)}. \tag{4.52}$$

Function $\mathcal{S}(\zeta;R)$ maps $C_0$ to the unit $\mathcal{S}$-circle with $C_1$ and $C_2$ mapping to two finite-length horizontal slits lying on the real axis. Figure 4.11 shows a schematic of this triply connected polycircular domain. Figure 4.12 shows a schematic of the sequence of conformal maps (4.51) required to map $D_\zeta$, as in Figure 4.10, to the polycircular arc domain as in Figure 4.11.

We claim that the complex velocity function is

$$\frac{dw}{dz}=Q_0\mathcal{S}(\zeta;R) \tag{4.53}$$

with function $\mathcal{S}(\zeta;R)$ as in (4.49). Note that the conditions (4.47) are automatically satisfied by this function (4.53) given the nature of the image of $D_\zeta$ under the polycircular arc mapping (4.49), i.e. the triply connected polycircular arc domain shown in Figure 4.11. The condition (4.46) is clearly satisfied. Notice that this mapping (4.53) has a simple zero at $\zeta=0$ if we choose

$$R=\frac{\omega(0,-1)}{\omega(0,1)}, \tag{4.54}$$

thus satisfying (4.48). Function (4.53) is also analytic and single-valued everywhere in the interior of $D_\zeta$ and hence $dw/dz$ is $L$-periodic across the period cell.

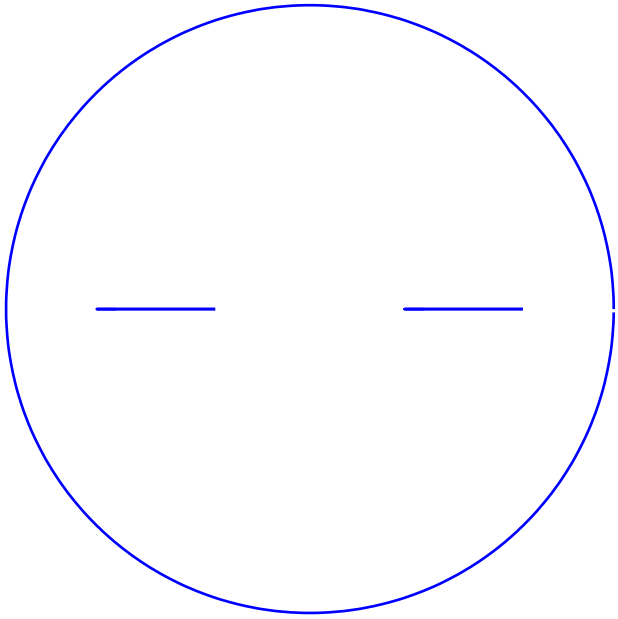

Figure 4.11: Schematic showing the image of $D_\zeta$ under the polycircular arc mapping $\mathcal{S}(\zeta; R)$ given in (4.49). Under this map, $C_0$ is mapped onto the unit-circle whilst $C_1$ and $C_2$ are mapped onto two finite-length horizontal slits on the real axis. The nature of this polycircular arc domain is vital to the construction of $dw/dz$.

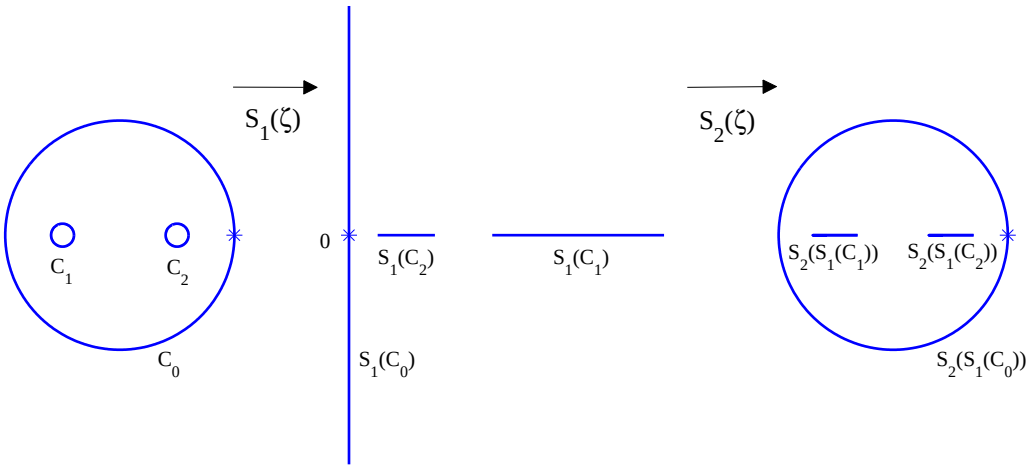


Figure 4.12: Schematic showing the sequence of conformal mappings (4.51) for the construction of an analytical expression for the triply connected polycircular arc domain shown in Figure 4.11.

### 4.4.4 Conformal map $z(\zeta)$

By free streamline theory, the conformal map determining the shape of the boundary of the hollow vortex in a typical period window, with centroid on the channel centreline, is given through the integral

$$z(\zeta) = \frac{\Gamma}{2Q_0} \int_{\zeta_0}^{\zeta} \frac{v_1'(\zeta') + v_2'(\zeta')}{S(\zeta'; R)} d\zeta', \tag{4.55}$$

where $\zeta_0 \in \mathbb{C}$ is an arbitrary point in the interior of $D_\zeta$.

### 4.4.5 Characterisation of the solutions

Let us set one of the length scales of the problem, and the time scale of the motion, by fixing

$$L = \Gamma = 1. \tag{4.56}$$

Let us define the aspect ratio of the period cell to be $\mathcal{R} = \lambda/L$ so that, with $L = 1$, the aspect ratio of the period cell is

$$\mathcal{R} = \lambda. \tag{4.57}$$

We expect to be able to fix this aspect ratio of the period cell; this sets the second length scale of the problem. As usual, the constant $\zeta_0$ in the conformal map (4.55) reflects a translational degree of freedom which can be set arbitrarily and the mapping shifted by an appropriate constant *a posteriori*. The complex potential of Rosenhead [92] for the unstaggered von Kármán point vortex street in a channel is determined by two parameters related to the horizontal distance between consecutive point vortices and their vertical spacing, once the channel width has been fixed. For us, this is equivalent to specifying $L$ and $\lambda$. The area associated with the hollow vortex can be assigned through the parameter $q$; this sets the third length scale of the problem. We shall now proceed to examine the solution class with $q$ as our only free parameter. This leaves just one real parameter, namely $\delta$, to be found in order to determine the shape of the hollow vortex boundary in a typical period cell of the row.

Our general strategy in finding solutions is to choose a value of the aspect ratio $\lambda$ and then gradually vary the value of $q$ in a standard continuation procedure, solving for the value of $\delta$ in each case. Recall the preimage circular domain $D_\zeta$ in the $\zeta$-plane. The centres of $C_1$ and $C_2$ are $\pm\delta \in \mathbb{R}$, and their radii are both $q$. We can choose this value of $q$ *a priori*; this is analogous to fixing the area of the hollow vortex. We are then left with just the real

parameter $\delta$ to determine. This is done by enforcing the single real condition prescribing the aspect ratio of the period cell:

$$\mathcal{R} = \left( \int_{-\delta+q}^{\delta-q} |z_\zeta(\zeta')d\zeta'| \right) \Big/ \left( \oint_{C_1} |z_\zeta(\zeta')d\zeta'| \right). \tag{4.58}$$

Owing to the up-down symmetry of the period cell about the channel centreline, the conformal map turns out to automatically be single-valued. It was checked that the image of $C_0$ under $z(\zeta)$ is indeed a closed curve:

$$\oint_{C_0} z_\zeta(\zeta')d\zeta' = 0. \tag{4.59}$$

From the value of $\delta$ found by solving (4.58), we can calculate the length, $\hat{L}$ (say), of one of the channel walls:

$$\hat{L} = \oint_{C_1} |z_\zeta(\zeta')d\zeta'|. \tag{4.60}$$

Then we can find the value of the pre-multiplicative constant in (4.55) *a posteriori*; this can be thought of as a rescaling parameter in order to fulfil our requirement that $L = 1$:

$$\frac{\Gamma}{2Q_0} = \frac{1}{\hat{L}}. \tag{4.61}$$

For a given area of the hollow vortex, we find that for any given channel width $\lambda$, there are two different sets of values of $\delta$ and $q$ defining the preimage domain $D_\zeta$. Both of these two sets of conformal moduli correspond to hollow vortices exhibiting two different shapes, but with the same area.

Figure 4.13 shows three period cells making up infinite channels with widths $\lambda = 0.28$, $0.375$ and $0.5$. In each period cell is a superposition of typical hollow vortex members, of different areas, forming part of the row in the channel. For each channel width, we observe that the hollow vortices vary in shape between one which is almost circular to one with long flattened faces along the two regions of their boundary which are closest to the channel walls. It is reassuring to observe that the hollow vortex shapes closely resemble those in free space (obtained either using the conformal map (3.36) presented in Chapter 3, or using the solution in [7]) when the width of the channel becomes large; such hollow vortices are shown in Figure 4.15 for $\lambda = 1$. All of these aforementioned observations are consistent with the behaviour of the graphs shown in Figure 4.16 (to be discussed shortly).

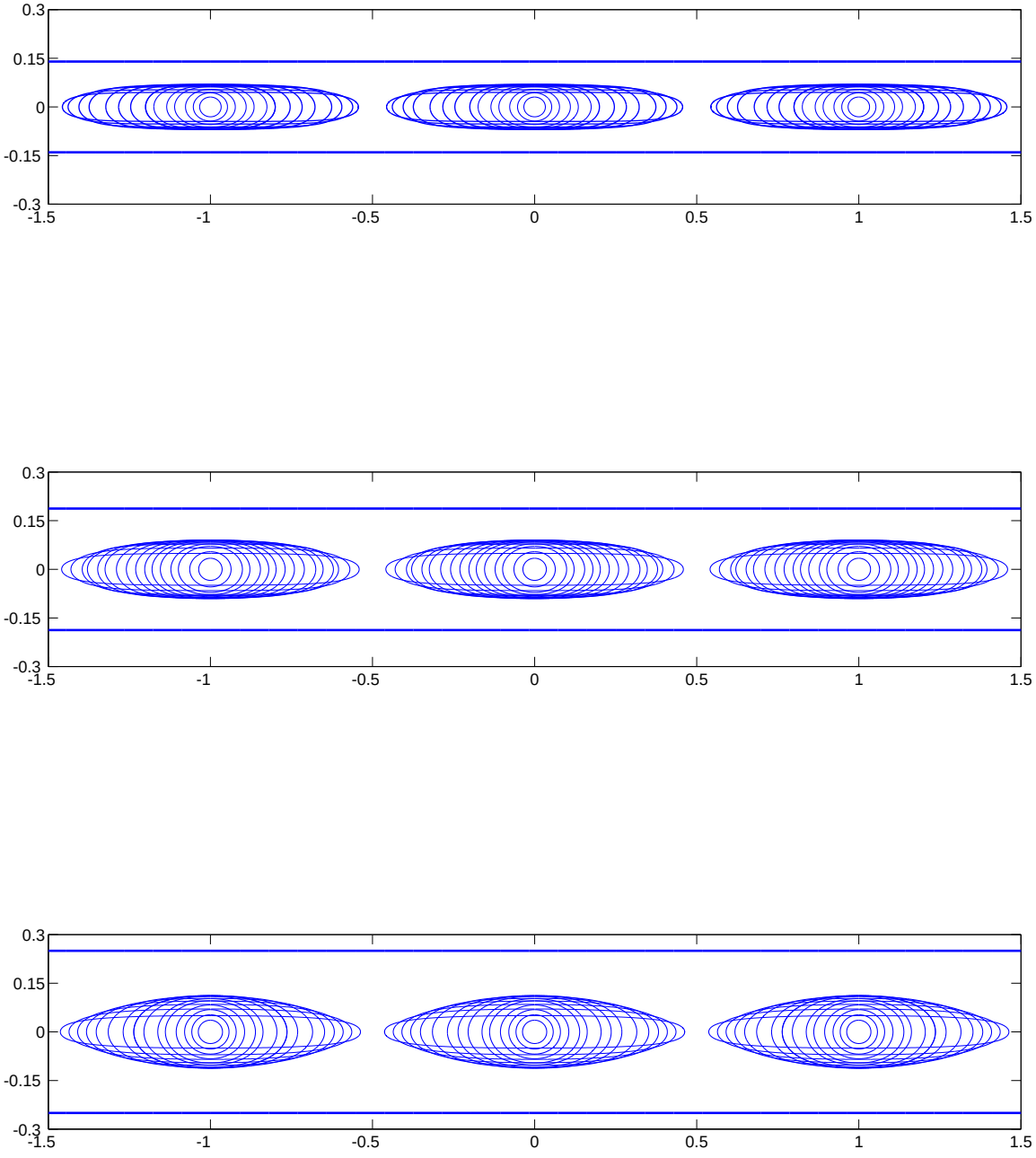


Figure 4.13: Superposition of typical members of the hollow vortex row in an infinite channel, of varying area, for three different channel widths: $\lambda = 0.28$ [top], $\lambda = 0.375$ [centre] and $\lambda = 0.5$ [bottom]. Three periods (of unit length $L = 1$) of the row are shown. For each $\lambda$, there is a hollow vortex with some maximum area.

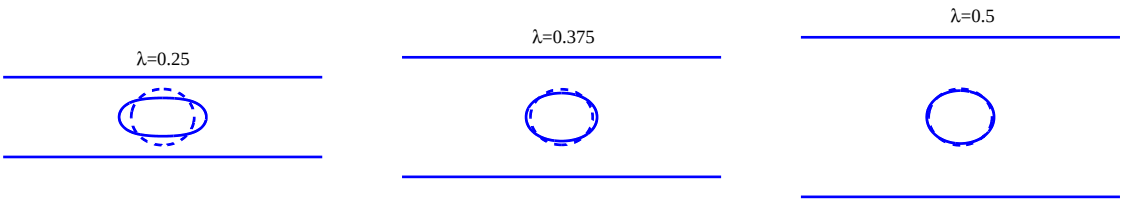


Figure 4.14: Three plots, for channel widths $\lambda = 0.25$ (left), $\lambda = 0.375$ (centre) and $\lambda = 0.5$ (right), of typical hollow vortex members in a row, of area 0.027. Superposed for comparison is a Baker, Saffman & Sheffield [7] hollow vortex in free space also of area 0.027; these are shown as dashed lines. As the channel widens, our solutions tend towards the free space shapes.

Although not immediately apparent in Figures 4.13 and 4.15, the graphs in Figure 4.16 also confirm that there exists a unique hollow vortex shape of some maximum area for a given channel width. Figure 4.14 compares one shape of hollow vortex, all of the same area, in three different channels with widths $\lambda = 0.25, 0.375, 0.5$. The free space hollow vortex is superposed on each. It is seen that there is a noticeable difference in shape compared with the free space hollow vortex for small channel widths $\lambda \lesssim 0.375$, but when $\lambda \approx 0.5$, the hollow vortex shapes assume essentially the same shapes as in free space. Our solutions can be viewed as the generalisation of the free space hollow vortex row solutions due to Baker, Saffman & Sheffield [7] to the case of an infinite channel of finite width, and are also the singly periodic generalisations of the Michell [77] hollow vortex in an infinite channel.

Figure 4.16 shows graphs, each corresponding to a different channel width $\lambda$, of the hollow vortex perimeter $P$ as a function of inverse separation between the hollow vortex centroids, each rescalled by the square root of the hollow vortex area $A$. Both of these quantities $P/A^{1/2}$ and $A^{1/2}/L$ (with $L = 1$) are dimensionless. Figure 3 in Baker, Saffman & Sheffield [7] shows a graph of the same quantities for the single row of hollow vortices in free space: this is shown in Figure 4.16 by a dashed line. One observation to make is that for each channel width $\lambda$, there is a maximum value of $A^{1/2}$ that can be attained, and this occurs at a unique value of $P/A^{1/2}$. As $\lambda$ is reduced, this maximum value of $A^{1/2}$ is also reduced, but the unique value of $P/A^{1/2}$ for which this is attained increases. For $\lambda = 1$, the

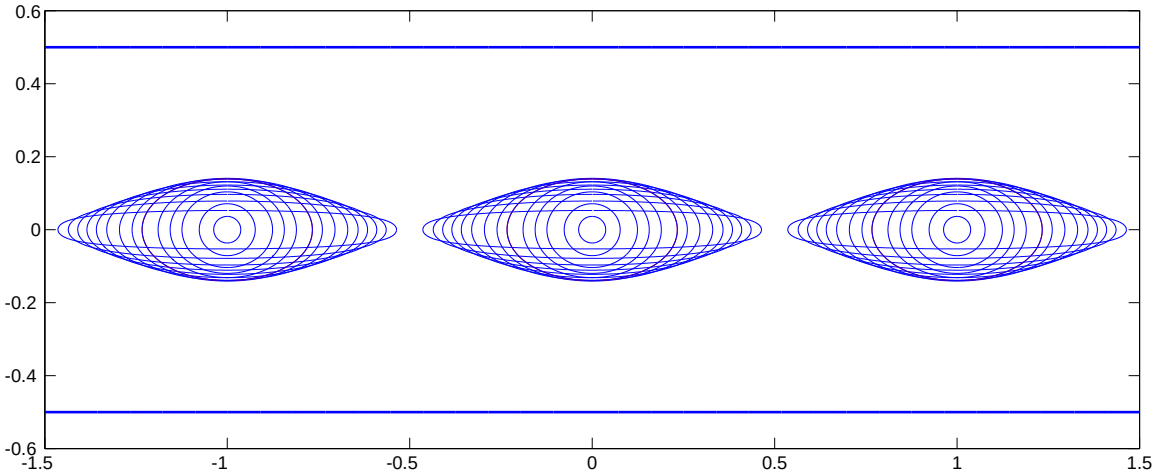


Figure 4.15: Superposition of typical members of the hollow vortex row, of varying areas, in an infinite channel of width $\lambda = 1$. Three periods (of unit length $L = 1$) of the row are shown. These hollow vortices essentially share the same shapes as hollow vortices in a row in free space.

maximum $A^{1/2} \approx 0.375$ and this is very close to value for a single row of hollow vortices in free space which is $A^{1/2} \approx 0.38$ as reported by Baker, Saffman & Sheffield [7]: this was expected since $\lambda = 1$ corresponds to a wide channel. For $\lambda = 0.375$, the maximum $A^{1/2} \approx 0.33$, and for $\lambda = 0.28$, the maximum $A^{1/2} \approx 0.3$.

We observe that each of the graphs turn around on themselves implying non-uniqueness of the solutions for a given value of the area $A$ and channel width $\lambda$; that is to say, for a given area $A$ and channel width $\lambda$, there will be two possible hollow vortex shapes with the same area. There will exist two possible shapes provided the value of $A^{1/2}$ is less than the maximum possible value; there do not exist any solutions for a given channel width $\lambda$ if one specifies an area greater than this permissible maximum. For a fixed area not close to the maximum, it appears that the hollow vortex with the higher value of $P/A^{1/2}$ exhibits a boundary shape with two elongated faces, whilst the hollow vortex with the lower value of $P/A^{1/2}$ appears to exhibit a quasi-elliptical or quasi-circular shape. For each channel width $\lambda$, the graphs each tend towards the free space graph when $A^{1/2} \to 0$ and when $P/A^{1/2} \to \infty$. When $A^{1/2} \to 0$, the hollow vortices are tending towards their point vortex counterparts by assuming near circular shapes of small area. Quantity $P/A^{1/2}$ has the minimum value $2\sqrt{\pi}$ for circles and each graph tends precisely to this value as $A^{1/2} \to 0$.

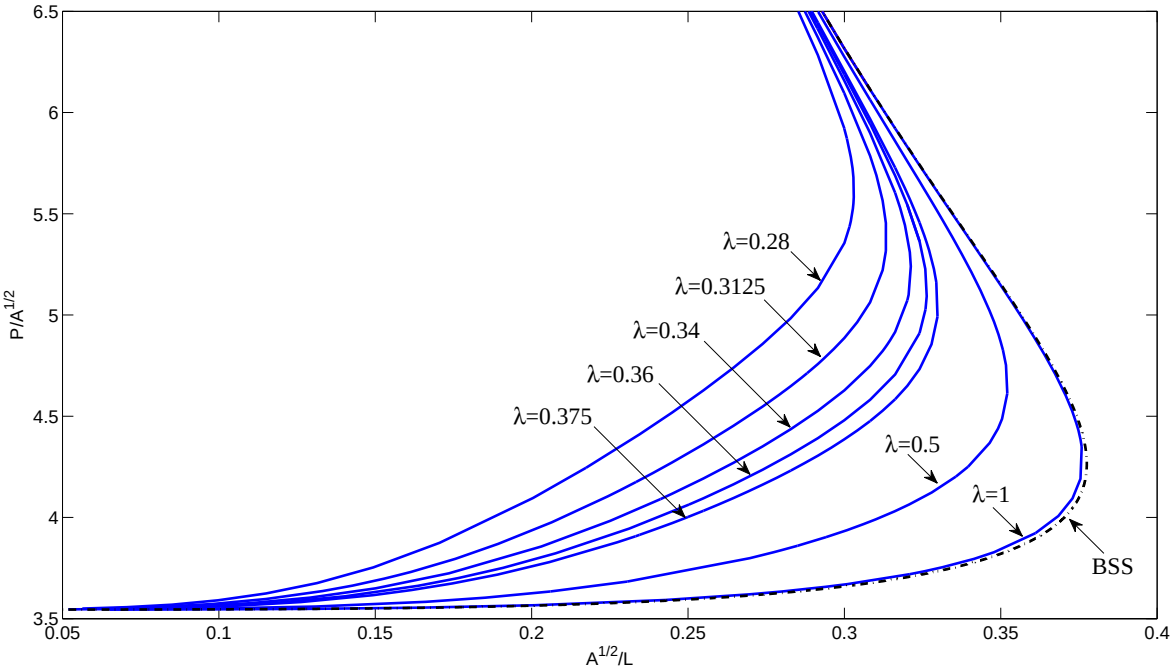


Figure 4.16: Graphs, for seven different channel widths $\lambda$, of the quantity $P/A^{1/2}$ as a function of $A^{1/2}/L$ (with $L = 1$ fixed). Here, $A$ and $P$ denote the perimeter and area of the hollow vortex, respectively, and $L$ denotes the separation between hollow vortex centroids. The corresponding graph for a single row of hollow vortices in free space is shown by the dashed line.

As $P/A^{1/2} \to \infty$, the graphs will eventually intersect the vertical axis at infinity; this again corresponds to zero area solutions. The nature of these limiting shapes is of particular interest. As reported in Baker, Saffman & Sheffield [7], as $P/A^{1/2} \to \infty$ in free space, the result is a vortex sheet of constant strength. Our results seem to suggest that the same phenomenon occurs in channels; that is, for any channel width $\lambda$, it is expected that a vortex sheet of constant strength will form along the channel centreline as the hollow vortex area shrinks to zero from its maximum value (i.e. a hollow vortex, in each period cell, of zero area).

It is important to note that the vertical axis in Figure 4.16 has been deliberately truncated at $P/A^{1/2} = 6.5$ since beyond this point, for all the solution branches, accurate computation of the Schottky-Klein prime function becomes very difficult; this is because the inner circles $C_1$ and $C_2$ of the preimage circular domain become close to the unit circle $C_0$, and such domains pertain to the hollow vortices which are very close to one another at an edge between two neighbouring period windows. Also, for channel widths $\lambda \leq 0.28$, the radii of $C_1$ and $C_2$ become rather large, and again, accurate computation of the Schottky-Klein prime function is known to become more challenging. Consequently, we stopped reducing the size of the channel widths at $\lambda = 0.28$. All the solution branches in Figure 4.16 were terminated when convergence of the Newton iteration became hard to achieve. The shapes of all our computed hollow vortices do not exhibit any singularities, and all are univalent.

Finally, it is worth describing how the preimage circular domain $D_\zeta$ changes as the hollow vortex shapes vary in qualitative appearance, for a given channel width $\lambda$. The inner circles $C_1$ and $C_2$ are initially centred in the vicinity of the origin with small radii; these domains correspond to small circular hollow vortices. $C_1$ and $C_2$ then gradually increase in radii and move apart until a maximum radius $q$ is reached at some value of $\delta$; this domain corresponds to the quasi-elliptical hollow vortices (note that this maximum radius $q$ does not correspond to the maximum area hollow vortex). $C_1$ and $C_2$ continue moving apart, but with their radii now decreasing, until they get very close to the unit circle $C_0$; these domains correspond to the hollow vortices impinging on their neighbours.

## 4.5 Summary

We have found closed-form analytical solutions for two types of free boundary problem involving hollow vortex configurations, and sharing the common feature that they are both

set is an infinite channel with straight, parallel-sided, impenetrable walls. We determined the free boundary shapes for a hollow vortex pair and for a single row of hollow vortices in an infinite channel. Incorporating the channel walls into the mathematical model (which are not themselves free boundaries) in addition to the free boundaries of the hollow vortices, required a delicate consideration of how the boundary conditions were to be enforced. As in Chapter 3, we used ideas from free streamline and conformal mapping theory which again proved to be advantageous. We also used our branch cut technique to assist in constructing the desired conformal mappings. Our analytical solutions for the single row of hollow vortices in an infinite channel appear to be the first of their kind whilst our analytical solutions for the co-travelling hollow vortex pair in an infinite channel complement those analytical solutions found recently by Zannetti & Lasagna [128].

In the case of the hollow vortex pair in an infinite channel, we constructed a conformal mapping from the interior of a concentric annulus to the fluid region exterior of the hollow vortex pair with some choice of branch cut mapping to the two channel walls. We found that the integral (4.55) for this conformal map shares an integrand with the same functional form as that found in the integral (3.78) governing the hollow vortex shapes in a von Kármán street. The use of both radial and circular conformal slit maps proved to be crucial. We determined that there exist solutions, each corresponding to a distinct shape of hollow vortex, with an infinite continuum of possible areas; that is to say, the hollow vortices can have their areas 'grown' without bound. We established that both the area and the relative position of the pair to the channel side walls has an effect on the speed of translation in the channel. Connections with two classical works were also made. Our solutions can be considered as generalisations to the infinite channel geometry of the solutions due to Pocklington [85]. When the centroids of the hollow vortex pair were equi-distant to themselves and the channel walls, we obtained the stationary solutions due to Michell [77].

To determine the boundary shapes for hollow vortices arranged in a single row in an infinite channel, we restricted attention to a period cell containing a typical member of the row, with centroid on the channel centreline, and incorporated the periodic nature of the problem by introducing a branch cut in the preimage circular domain whose two sides were required to map to the vertical edges of the cell. We found a concise formula for the conformal map as an explicit indefinite integral to the interior of this period cell from a particular triply connected bounded circular domain. In devising this conformal map, we made use of the integrals of the first kind $v_j(\zeta)$ associated with the preimage circular domain and

a special choice of polycircular arc map. Our solutions are natural generalisations to an infinite channel of the hollow vortex row solutions in free space due to Baker, Saffman & Sheffield [7]; our solutions are also the singly periodic generalisations of the single hollow vortex in an infinite channel due to Michell [77]. Three interesting discoveries were made for a given channel width: there exist two possible hollow vortex shapes for a given value of area, there exists a boundary shape with a maximum obtainable area, and the formation of a vortex sheet of constant strength is theoretically possible as the maximum area shape is deformed to zero area in a particular limit. Our approach to the single row in an infinite channel can be readily generalised to the case where the centroids of the hollow vortices are not aligned on the channel centreline (see Appendix D).

# Chapter 5

# Föppl hollow vortex pair behind a circular cylinder

## 5.1 Introduction and background

In this chapter, we will desingularise another point vortex equilibrium: the Föppl vortex pair behind a circular cylinder. We will consider a pair of up-down symmetric hollow vortices, of equal and opposite circulation, positioned behind a circular cylinder of unit radius superposed with a steady uniform flow. As in Chapters 3 and 4, our aim is to solve for the free boundary shapes of the hollow vortices. Rather than find explicit analytical solutions, we will instead devise a hybrid analytical-numerical method to solve this free boundary problem. More specifically, by employing the 'new calculus' of Crowdy [14, 22] for ideal fluid mechanics in multiply connected geometries, we can write down an analytical formula for the complex potential; if we then express the conformal mapping determining the hollow vortex boundary shapes in terms of a Fourier-Laurent series expansion, the free boundary problem is reduced to a finite-set of non-linear equations to be solved numerically.

The topic of flow around a circular cylinder is a classical one and a problem of fundamental importance in fluid dynamics owing to the fact that, at a moderate Reynolds number, stationary counter-rotating vortical eddies form in the wake of the cylinder which, when the symmetry about the flow centreline is lost at a higher Reynolds number, can evolve into a von Kármán vortex street. To gain insight into this vortex shedding phenomenon behind a cylinder, it is expedient to first study a simplified model of this system using a pair of point vortices of equal and opposite circulation placed behind the circular cylinder within

a uniform stream of ideal fluid with an up-down symmetry about the flow centreline: this flow is a potential flow and the configuration is known as a 'Föppl system' or 'Föppl equilibrium' owing to the first study of this system by Föppl in 1913 [46]. He found that the point vortices lie on particular curves when in equilibrium with the cylinder (these curves now go by the name of 'Föppl curves'), and that the position and circulation of the point vortices are related by two simple algebraic expressions (see Appendix E). As indicated by Föppl [46], this simplified point vortex model agrees with observations of the locations of the centroids of the vortical eddies as seen in experiments. The review by Protas [89] makes further references to the Föppl system in a variety of different contexts.

In this chapter, we will solely focus on desingularising Föppl equilibria with the two vortices positioned strictly behind the circular cylinder. One reason for this choice is that this configuration is likely to be the most physically relevant scenario in applications and is also most likely to occur in nature. A second reason for this choice is related to the issue of stability. Föppl [46] found that this class of point vortex equilibria is stable against symmetric perturbations with respect to the flow centreline. Moreover, Elcrat, Fornberg & Miller [42] found that when the Föppl equilibrium is desingularised by finite-area vortex patches of constant vorticity that the system shares the same stability properties as the associated point vortex system. In light of this, it seems reasonable to hypothesise that our hollow vortex desingularisations, when positioned strictly behind the cylinder, should also be stable with respect to such symmetric perturbations about the flow centreline.

Recently, Vasconcelos, Moura & Schakel [118] have reappraised the Föppl point vortex system from the point of view of Hamiltonian dynamics and have discovered some novel and interesting dynamical features of the configuration. They have presented the phase portrait of the governing Hamiltonian for a pair of point vortices moving symmetrically with respect to the flow centreline, and discovered the existence of a nilpotent saddle point at infinity whose homoclinic orbits throw further light on the non-linear stability of the Föppl equilibria. The Föppl point vortex model has also fuelled various other studies, including the investigation of the control of vortex shedding (Protas [86, 88]), the modelling of symmetrical wakes behind slender bodies using equilibria consisting of multiple point vortices (Weihs & Boasson [123]), and the determination of point vortex equilibrium conditions in flows past bluff bodies with arbitrary shapes (Zannetti [127]).

The Föppl point vortex system has already been desingularised using vortex patches. In-

deed, Elcrat et al [44] have undertaken a comprehensive numerical investigation into the desingularised Föppl system using the vortex patch model. They demonstrated the existence of continuous families of finite-area vortex patches of constant vorticity in equilibrium behind a circular cylinder. Furthermore, they were able to show that solutions exist for vortex patches which are close-to-touching with the circular cylinder; in particular, they found that as the area of the vortex patch is increased, it eventually attains a maximum area shape which is bounded by the cylinder. Subsequently, Protas [87] has constructed a two-parameter family of 'higher-order Föppl systems'; Protas has described these as generalisations of the Föppl point vortex system which approximate the velocity field for a given flow of the type considered by Elcrat et al [44].

There have been two recent studies involving hollow vortices in the wakes of obstacles. Elcrat & Zannetti [41] have very recently examined hollow vortices in the wake of a plate normal to an oncoming uniform flow. Of most interest to us is the study by Telib & Zannetti [112]. They have presented solutions, obtained using a combination of conformal mapping techniques and elliptic function theory, describing hollow vortex equilibria in the wakes behind 'bumps' of various shapes on an infinite horizontal wall; in particular, they found a continuous family of hollow vortex solutions in the wake of a semi-circular bump i.e. hollow vortex desingularisations of the Föppl system in the upper-half plane. Like ours, the approach of Telib & Zannetti [112] can also be described as a hybrid analytical-numerical method and, even though our mathematical approaches are different, several similar theoretical threads appear to run through both our work and theirs. Owing to the solutions of Telib & Zannetti [112], the solutions we present in this chapter are therefore not the first desingularisations of the Föppl point vortex pair using the hollow vortex model. Nevertheless, our approach is valuable since it has a large analytical component, is conceptually straightforward to understand, and pertains entirely to hollow vortex equilibria behind a circular cylinder. It is also fair to say that Telib & Zannetti [112] did not devote much of their study to the Föppl desingularisation, presenting only one family of hollow vortex solutions (for some circulation value) in this particular case. We will recover this family of solutions featuring in [112], and present three other families, and therefore build on the contribution of Telib & Zannetti [112].

When devising the complex potential for the pair of hollow vortices in a uniform flow behind a circular cylinder, we will adhere to the work of Crowdy [14, 22] who has found generalised analytical expressions for the complex potentials, in terms of the Schottky-Klein

prime function, describing various inviscid flows in multiply connected geometries. Indeed, the hollow vortex configuration of interest in this chapter can equivalently be viewed as a uniform flow past three arbitrary obstacles with circulation, and thus naturally lends itself to the analytical treatment of Crowdy [14, 22]. This new calculus due to Crowdy is expected to arise in the modelling of many exciting future applications. One such example is the recent interesting study by Subhash Reddy, Muddada & Patnaik [107]. They have examined the uniform flow past a circular cylinder in the presence of two small counter-rotating circular control cylinders. By employing the analytical results of Crowdy, they used a Föppl model to establish the optimum position and circulation strength of the two counter-rotating control cylinders in order to suppress vortex formation behind the cylinder.

## 5.2 Formulation of problem

Consider a circular cylinder of unit radius, centred at the origin in a $z$-plane, surrounded by inviscid, incompressible, irrotational fluid. The boundary of the circular cylinder $|z| = 1$ is assumed to be solid and impenetrable. Suppose there is a uniform flow of speed $U$ translating left-to-right, parallel to the real axis. Suppose there are two hollow vortices, positioned strictly behind the circular cylinder, of equal and opposite circulation; let the hollow vortex in the upper-half plane have circulation $-\Gamma$ ($\Gamma > 0$) and let the hollow vortex in the lower-half plane have circulation $\Gamma$. We assume that the hollow vortices are in equilibrium, and are up-down symmetric about the flow centreline. Figure 5.1 shows a schematic of this configuration.

Let $D_\zeta$ be the following triply connected circular domain in a parametric $\zeta$-plane. Take the unit $\zeta$-disc and from it excise two smaller discs whose boundaries are the circles $C_1$ and $C_2$. Let the unit $\zeta$-circle be labelled $C_0$, let $C_1$ label the circle $|\zeta| = \rho$ and let $C_2$ label the circle with centre $\delta \in \mathbb{R}$, $\delta > 0$, and radius $q$. In choosing this preimage domain $D_\zeta$, we have used up the three real degrees of freedom associated with the Riemann-Koebe mapping theorem. Let $\omega(\cdot, \cdot)$ denote the Schottky-Klein prime function associated with $D_\zeta$.

Consider a conformal mapping $z(\zeta)$ taking the interior of $D_\zeta$ to the exterior of the circular cylinder $|z| = 1$ and the pair of hollow vortices. We wish to determine the shape of the boundaries of the two hollow vortices. Let $C_0$ and $C_1$ map to the two hollow vortices, with $C_0$ mapping to the hollow vortex in the upper-half plane and $C_1$ mapping to the hollow vortex in the lower-half plane. Let $C_2$ map to the boundary of the circular cylinder. In light

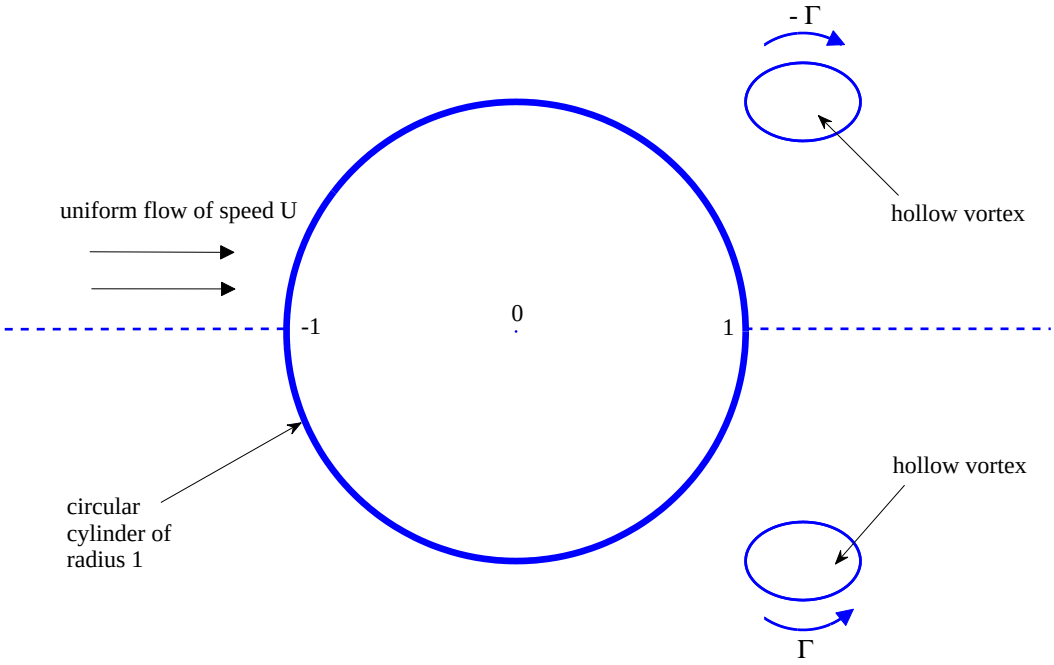


Figure 5.1: Schematic of the physical configuration in the $z$-plane. A pair of hollow vortices, whose free boundary shapes are to be determined, are positioned behind the circular cylinder $|z| = 1$ within a uniform flow of speed $U$. The hollow vortices are in equilibrium with the cylinder, and are up-down symmetric about the flow centreline (the real axis). The hollow vortex in the upper-half plane has circulation $-\Gamma$ and the hollow vortex in the lower-half plane has circulation $\Gamma$.

of the up-down symmetry in the $z$-plane, the arc of the circle $|\zeta| = \sqrt{\rho}$ lying in the interior of $D_\zeta$ will map to the real line through the point at infinity. Note that the interior of $D_\zeta$ such that $\sqrt{\rho} < |\zeta| < 1$ maps into the upper-half $z$-plane whilst the interior of $D_\zeta$ such that $\rho < |\zeta| < \sqrt{\rho}$ maps into the lower-half $z$-plane; thus, the up-down symmetry of the configuration is intrinsic in the definition of $z(\zeta)$. There will be some point $\zeta = \beta = \sqrt{\rho}\mathrm{e}^{\mathrm{i}\theta}$ mapping to infinity. This implies that

$$z(\zeta) = \frac{a}{\zeta - \beta} + \text{locally analytic function}, \quad \zeta \to \beta, \tag{5.1}$$

where $a \in \mathbb{C}$. At all other points in $D_\zeta$, the map $z(\zeta)$ is analytic. Figure 5.2 shows a schematic of the preimage domain $D_\zeta$.

We will now devise a hybrid analytical-numerical method, in a similar spirit to Telib & Zannetti [112], to solve our free boundary problem. We will first construct an analytical expression for the complex potential $W(\zeta)$ using the work of Crowdy [14, 22]. We will then write a Fourier-Laurent expansion for the conformal mapping $z(\zeta)$ governing the hollow vortex boundary shapes whose coefficients, in addition to some other parameters, will need to be determined numerically.

## 5.3 Function $W(\zeta)$

Let us first construct an analytical expression for the complex potential function $W(\zeta)$. The complex potential $w(z)$ in the $z$-plane is related to the complex potential $W(\zeta)$ in the $\zeta$-plane through the composition

$$W(\zeta) = w(z(\zeta)). \tag{5.2}$$

We opt to form $W(\zeta)$ as the sum of two auxiliary functions, i.e.

$$W(\zeta) = W_1(\zeta) + W_2(\zeta), \tag{5.3}$$

where $W_1(\zeta)$ is the complex potential for the uniform flow at infinity, and $W_2(\zeta)$ is the complex potential associated with the pair of hollow vortices. Owing to the fact that the circular cylinder and the hollow vortex boundaries are streamlines, we require

$$\mathrm{Im}[W(\zeta)] = \text{constant}, \quad \zeta \in C_0, C_1, C_2. \tag{5.4}$$

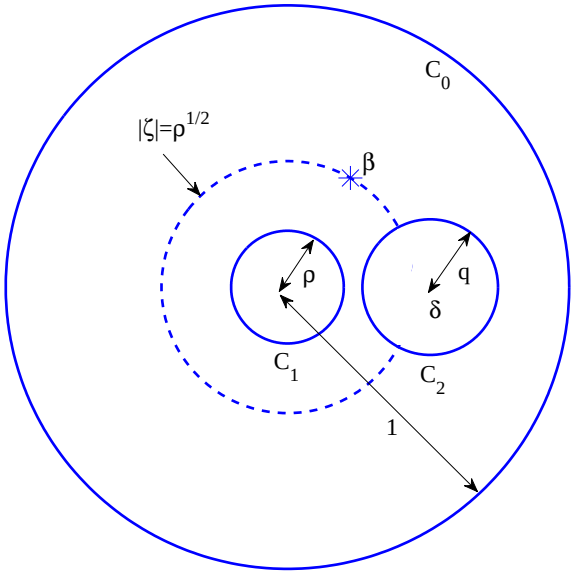


Figure 5.2: The preimage bounded triply connected circular domain $D_\zeta$ in the $\zeta$-plane. Let $C_0$ denote $|\zeta| = 1$, let $C_1$ denote $|\zeta| = \rho$, and let $C_2$ denote $|\zeta - \delta| = q$. The circles $C_0$ and $C_1$ are mapped by $z(\zeta)$ onto the two hollow vortices. The interior circle $C_2$ is mapped onto the circular cylinder. The arc of the circle $|\zeta| = \sqrt{\rho}$ lying in the interior of $D_\zeta$ is mapped onto the real axis. The point $\zeta = \beta$ lying on $|\zeta| = \sqrt{\rho}$ is mapped to infinity.

To ensure that the hollow vortices have the correct circulations around them, and that there is zero circulation around the circular cylinder, we must also have

$$\oint_{C_0} d[W(\zeta)] = -\Gamma, \quad \oint_{C_1} d[W(\zeta)] = \Gamma, \quad \oint_{C_2} d[W(\zeta)] = 0, \tag{5.5}$$

where all three boundary circles are positively oriented in the anticlockwise direction.

### 5.3.1 Function $G_0(\zeta;\alpha)$

An important function to be used in the proceeding analysis is

$$G_0(\zeta;\alpha) = -\frac{\mathrm{i}}{2\pi}\log\left(\frac{\omega(\zeta,\alpha)}{|\alpha|\omega(\zeta,1/\overline{\alpha})}\right), \tag{5.6}$$

where $\alpha = \alpha_x + \mathrm{i}\alpha_y \in \mathbb{C}$ is some point lying in the interior of $D_\zeta$. Function $G_0(\zeta,\alpha)$ is the complex potential for a point vortex of circulation $+1$ in a multiply connected domain (Crowdy [14, 22]). Function $G_0(\zeta,\alpha)$ is also the analytic extension of the modified Green's function for Laplace's equation in $D_\zeta$ (Crowdy & Marshall [32]). Function $G_0(\zeta,\alpha)$ is analytic everywhere in $D_\zeta$ except for a logarithmic singularity at $\zeta = \alpha$. It has constant imaginary part on each of the boundary circles of $D_\zeta$; this is easily realised on noting that

$$G_0(\zeta;\alpha) = -\frac{\mathrm{i}}{2\pi}\log\eta(\zeta;\alpha), \tag{5.7}$$

where $\eta(\zeta;\alpha)$ is the bounded circular slit mapping of (2.53).

Crowdy [14] used the function $G_0(\zeta;\alpha)$ to derive the complex potential for a uniform flow past multiple obstacles by taking parametric derivatives of $G_0(\zeta;\alpha)$ i.e. derivatives with respect to its second argument. Note that

$$\frac{\partial G_0(\zeta;\alpha)}{\partial\alpha_x} = \left(\frac{\partial}{\partial\alpha} + \frac{\partial}{\partial\overline{\alpha}}\right)G_0(\zeta;\alpha) \tag{5.8}$$

and

$$\frac{\partial G_0(\zeta;\alpha)}{\partial\alpha_y} = \mathrm{i}\left(\frac{\partial}{\partial\alpha} - \frac{\partial}{\partial\overline{\alpha}}\right)G_0(\zeta;\alpha). \tag{5.9}$$

We have

$$\frac{\partial G_0}{\partial\alpha} = \frac{\mathrm{i}}{2\pi}\frac{1}{\zeta-\alpha} + \text{locally analytic function}, \quad \zeta\to\alpha, \tag{5.10}$$

and so it follows from (5.8) and (5.9) that

$$2\pi\frac{\partial G_0}{\partial \alpha_x} = \frac{\mathrm{i}}{\zeta-\alpha} + \text{locally analytic function}, \quad \zeta \to \alpha, \tag{5.11}$$

and

$$-2\pi\frac{\partial G_0}{\partial \alpha_y} = \frac{1}{\zeta-\alpha} + \text{locally analytic function}, \quad \zeta \to \alpha, \tag{5.12}$$

i.e. both these quantities have simple pole singularities at $\zeta = \alpha$. Since both $\partial G_0/\partial\alpha_x$ and $\partial G_0/\partial\alpha_y$ are partial derivatives taken with respect to real quantities, we have that

$$\mathrm{Im}\left[\frac{\partial G_0}{\partial \alpha_x}\right] = \text{constant}, \quad \zeta \in C_0, C_1, C_2, \tag{5.13}$$

and

$$\mathrm{Im}\left[\frac{\partial G_0}{\partial \alpha_y}\right] = \text{constant}, \quad \zeta \in C_0, C_1, C_2. \tag{5.14}$$

We are now in a position to construct, in turn, the two auxiliary functions $W_1(\zeta)$ and $W_2(\zeta)$. Recall that $W_1(\zeta)$ is the complex potential for the uniform flow at infinity, and $W_2(\zeta)$ is the complex potential associated with the pair of hollow vortices.

### 5.3.2 Function $W_1(\zeta)$

We have a uniform flow parallel to the real axis. This means that

$$w(z) = Uz + \text{locally analytic function}, \quad z \to \infty. \tag{5.15}$$

It follows from (5.1) that we require

$$W(\zeta) = \frac{Ua}{\zeta-\beta} + \text{locally analytic function}, \quad \zeta \to \beta. \tag{5.16}$$

Consider, thus, the function

$$W_1(\zeta) = UA_x\left(-2\pi\frac{\partial G_0}{\partial \alpha_y}\bigg|_{\alpha=\beta}\right) + UA_y\left(2\pi\frac{\partial G_0}{\partial \alpha_x}\bigg|_{\alpha=\beta}\right), \tag{5.17}$$

or, equivalently,

$$W_1(\zeta) = -2\pi\mathrm{i}U\left(a\frac{\partial G_0}{\partial \alpha}\bigg|_{\alpha=\beta} - \overline{a}\frac{\partial G_0}{\partial \overline{\alpha}}\bigg|_{\alpha=\beta}\right), \tag{5.18}$$

where

$$a = A_x + \mathrm{i}A_y. \tag{5.19}$$

Note that $W_1(\zeta)$ in (5.18) has the correct behaviour (5.16) as $\zeta \to \beta$, and is such that

$$\mathrm{Im}[W_1(\zeta)] = \text{constant}, \quad \zeta \in C_0, C_1, C_2, \tag{5.20}$$

as required. Note also that $W_1(\zeta)$ in (5.18) is single-valued when a $2\pi$ traversal is made around each of the boundary circles (as can be seen from the behaviours (5.11) and (5.12)); this immediately implies

$$\oint_{C_0} d[W_1(\zeta)] = \oint_{C_1} d[W_1(\zeta)] = \oint_{C_2} d[W_1(\zeta)] = 0. \tag{5.21}$$

That is, function $W_1(\zeta)$ puts zero circulation around the hollow vortices and zero circulation around the circular cylinder.

### 5.3.3 Function $W_2(\zeta)$

We need to add circulation around the hollow vortices and ensure that their boundaries are streamlines of the flow. The hollow vortex whose preimage is $C_0$ has circulation $-\Gamma$ and the hollow vortex whose preimage is $C_1$ has circulation $\Gamma$ (with $\Gamma > 0$). Consider the function

$$W_2(\zeta) = \Gamma v_1(\zeta). \tag{5.22}$$

It is immediate that

$$\mathrm{Im}[W_2(\zeta)] = \text{constant}, \quad \zeta \in C_0, C_1, C_2, \tag{5.23}$$

owing to the properties (2.8) and (2.9). From the '$a$-cycle' properties of the $v_j(\zeta)$ functions (2.7), we have

$$\oint_{C_1} d[W_2(\zeta)] = \Gamma, \quad \oint_{C_2} d[W_2(\zeta)] = 0, \tag{5.24}$$

as required, where $C_1$ and $C_2$ are positively oriented in the anticlockwise direction. We also have

$$\oint_{C_0} d[W_2(\zeta)] = -\Gamma, \tag{5.25}$$

where the integral is positively oriented in the anticlockwise direction around $C_0$, as required. To evaluate this integral (5.25), consider integrating along the contour shown in Figure 5.3. We make $v_1(\zeta)$ a single-valued function in $D_\zeta$ by introducing a branch cut

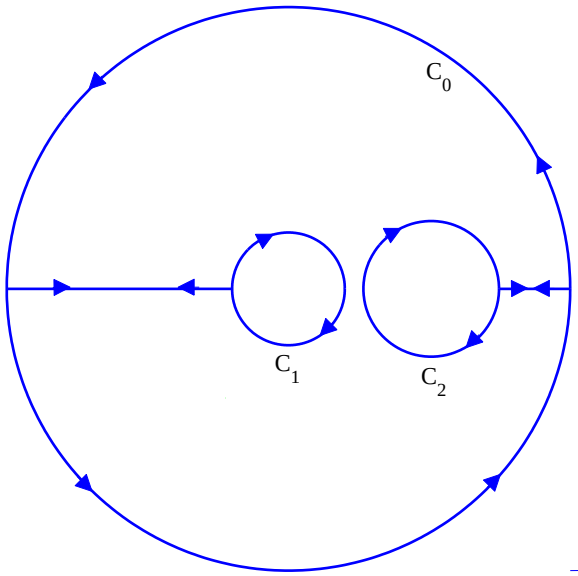


Figure 5.3: Contour to evaluate the integral (5.25) around $C_0$.

along the negative real axis joining $0$ and $\infty$. It is then apparent, using (5.24), that

$$\oint_{C_0} d[W_2(\zeta)] = -\left(\oint_{C_2} + \oint_{C_1}\right) d[W_2(\zeta)] = -\Gamma. \tag{5.26}$$

### 5.3.4 Function $W(\zeta)$

Adding (5.18) and (5.22), we conclude that the complex potential function is

$$W(\zeta) = -2\pi \mathrm{i} U \left( a \frac{\partial G_0}{\partial \alpha}\bigg|_{\alpha=\beta} - \overline{a} \frac{\partial G_0}{\partial \overline{\alpha}}\bigg|_{\alpha=\beta} \right) + \Gamma v_1(\zeta). \tag{5.27}$$

## 5.4 Function $W_\zeta(\zeta)$

In taking the derivative of $W(\zeta)$ with respect to $\zeta$, it is required to evaluate the following mixed second-order derivatives of function $G_0(\zeta;\alpha)$:

$$\frac{\partial^2 G_0}{\partial \zeta \partial \alpha} \quad \text{and} \quad \frac{\partial^2 G_0}{\partial \zeta \partial \overline{\alpha}}. \tag{5.28}$$

To evaluate these, we must use the infinite product form of the Schottky-Klein prime function (2.3). From (5.6), we have

$$\frac{\partial G_0}{\partial \alpha} = \frac{\mathrm{i}\Gamma}{2\pi}\left(\frac{1}{2\alpha} - \frac{\partial \omega(\zeta,\alpha)/\partial\alpha}{\omega(\zeta,\alpha)}\right) \tag{5.29}$$

and

$$\frac{\partial G_0}{\partial \overline{\alpha}} = \frac{\mathrm{i}\Gamma}{2\pi}\left(\frac{1}{2\overline{\alpha}} + \frac{\partial \omega(\zeta,1/\overline{\alpha})/\partial\overline{\alpha}}{\omega(\zeta,1/\overline{\alpha})}\right). \tag{5.30}$$

By taking logarithmic derivative of (2.3) with respect to $\alpha$, and then taking a derivative with respect to $\zeta$, we obtain from (5.29) that:

$$\frac{\partial^2 G_0(\zeta;\alpha)}{\partial\zeta\partial\alpha} \equiv -\frac{\mathrm{i}\Gamma}{2\pi}\frac{\partial}{\partial\zeta}\left(\frac{\partial\omega(\zeta,\alpha)/\partial\alpha}{\omega(\zeta,\alpha)}\right)$$

$$= -\frac{\mathrm{i}\Gamma}{2\pi}\left[\frac{1}{(\zeta-\alpha)^2} + \sum_{\theta\in\Theta''}\frac{\theta'(\alpha)}{(\zeta-\theta(\alpha))^2} + \sum_{\theta\in\Theta''}\frac{\theta'(\zeta)}{(\alpha-\theta(\zeta))^2}\right]. \tag{5.31}$$

Similarly, taking a logarithmic derivative of (2.3) with respect to $\overline{\alpha}$, followed by a derivative with respect to $\zeta$, we obtain from (5.30) that:

$$\frac{\partial^2 G_0(\zeta;\alpha)}{\partial\zeta\partial\overline{\alpha}} \equiv \frac{\mathrm{i}\Gamma}{2\pi}\frac{\partial}{\partial\zeta}\left(\frac{\partial\omega(\zeta,1/\overline{\alpha})/\partial\overline{\alpha}}{\omega(\zeta,1/\overline{\alpha})}\right)$$

$$= -\frac{\mathrm{i}\Gamma}{2\pi\overline{\alpha}^2}\left[\frac{1}{(\zeta-1/\overline{\alpha})^2} + \sum_{\theta\in\Theta''}\frac{\theta'(1/\overline{\alpha})}{(\theta(1/\overline{\alpha})-\zeta)^2} + \sum_{\theta\in\Theta''}\frac{\theta'(\zeta)}{(\theta(\zeta)-1/\overline{\alpha})^2}\right]. \tag{5.32}$$

Written out in full, the derivative of $W(\zeta)$ with respect to $\zeta$ is:

$$W_\zeta(\zeta) = -2\pi\mathrm{i}U\left(a\frac{\partial^2 G_0}{\partial\zeta\partial\alpha}\bigg|_{\alpha=\beta} - \overline{a}\frac{\partial^2 G_0}{\partial\zeta\partial\overline{\alpha}}\bigg|_{\alpha=\beta}\right) + \Gamma v_1'(\zeta) \tag{5.33}$$

with the mixed derivatives $\partial^2 G_0/\partial\zeta\partial\alpha$ and $\partial^2 G_0/\partial\zeta\partial\overline{\alpha}$ given in (5.31) and (5.32), respectively.

## 5.5 Conformal map $z(\zeta)$

Let us now consider the conformal mapping $z(\zeta)$ from the interior of $D_\zeta$ to the exterior of the unit radius circular cylinder and the two hollow vortices in the $z$-plane. Consider the

following ansatz:

$$z(\zeta) = \frac{a}{\zeta - \beta} + \sum_{j=0}^{\infty} c_j \zeta^j + \sum_{j=1}^{\infty} \frac{d_j \rho^j}{\zeta^j} + \sum_{j=1}^{\infty} \frac{e_j q^j}{(\zeta - \delta)^j}. \tag{5.34}$$

This Fourier-Laurent series expansion is a very convenient representation for the conformal mapping. It is obviously single-valued and analytic everywhere in $D_\zeta$ except for the required simple pole singularity at $\zeta = \beta$. The coefficients $\{c_j, d_j, e_j \in \mathbb{C}\}$, in addition to the numbers $a \in \mathbb{C}$ and $\beta = \sqrt{\rho}\mathrm{e}^{\mathrm{i}\theta} \in \mathbb{C}$, are to be determined; once found, the free boundary shapes of the two hollow vortices will be revealed. Obviously, for numerical implementation, it is required to truncate the infinite sums.

## 5.6 Function $z_\zeta(\zeta)$

The derivative of the conformal map $z(\zeta)$ with respect to $\zeta$ can easily be obtained once all the parameters in (5.34) have been determined. It is

$$z_\zeta(\zeta) = -\frac{a}{(\zeta - \beta)^2} + \sum_{j=1}^{\infty} j c_j \zeta^{j-1} - \sum_{j=1}^{\infty} \frac{j d_j \rho^j}{\zeta^{j+1}} - \sum_{j=1}^{\infty} \frac{j e_j q^j}{(\zeta - \delta)^{j+1}}. \tag{5.35}$$

## 5.7 Characterisation of the solutions

Upon consideration of the Föppl point vortex system, we note that the solution family can be described by four real parameters: $\Gamma$, $U$, $x_0$, $y_0$, where $z_0 = x_0 + \mathrm{i}y_0$ is the equilibrium position of the point vortex in the upper-half plane. By the symmetry, there is a corresponding equilibrium position at $\overline{z_0}$. Without loss of generality, we can set $U = 1$. If we then fix the value of $\Gamma$, then the position of the point vortex equilibrium $z_0$ is determined from two simple algebraic equations (see Appendix E).

Consider the parameters $U$, $\Gamma$ and $\rho$. These parameters correspond to the length scale of the problem, the time scale of the problem, and the area of the hollow vortices, respectively. In a similar fashion to our work in Chapters 3 and 4, we will assume that small hollow vortices are close-to-circular, and trace out a family of solutions for fixed values of $\Gamma$ and $U$ by a standard continuation procedure in the free parameter $\rho$. Analogously to the Föppl system, fixing the values of both $\Gamma$ and $U$ will fix the centroids of our two hollow vortices for a particular value of $\rho$. Note however that these centroid positions will change as $\rho$ is varied (keeping $\Gamma$ and $U$ fixed).

It is required to truncate the Fourier-Laurent series in (5.34). Let us truncate each series in (5.34) at $\mathcal{O}(N)$. We must solve for the following $3N+2$ real parameters

$$\mathrm{Im}[a], \quad \mathrm{Im}[c_0], \quad \{\mathrm{Im}[c_j], \mathrm{Im}[d_j], \mathrm{Im}[e_j] \mid j = 1, ..., N\}, \tag{5.36}$$

and the following $3N+6$ real parameters

$$c, \quad \delta, \quad q, \quad \arg[\beta], \quad \mathrm{Re}[a], \quad \mathrm{Re}[c_0], \quad \{\mathrm{Re}[c_j], \mathrm{Re}[d_j], \mathrm{Re}[e_j] \mid j = 1, ..., N\}, \tag{5.37}$$

where $c$ is the speed of the fluid on both of the hollow vortex boundaries:

$$\left|\frac{dw}{dz}(\zeta)\right| = c, \quad \zeta \in C_0, C_1. \tag{5.38}$$

Thus, it is apparent that we have a total of $6N+8$ real parameters to determine.

To obtain good initial estimates for these parameters in (5.36) and (5.37), and hence lock onto a family of hollow vortex solutions, with the values of $\Gamma$ and $U$ fixed, it is possible to construct a Möbius map from the interior of $D_\zeta$ to the exterior of $|z| = 1$ and two small circular hollow vortices whose centroids are located at the Föppl equilibrium positions $z_0$ and $\overline{z_0}$ corresponding to the chosen fixed values of $\Gamma$ and $U$. When these two circular hollow vortices are small, the parameters we seek should be very close to those obtained via this Möbius map (see Appendix E for details). As mentioned previously, we shall restrict attention to finding hollow vortex equilibria which lie strictly behind the circular cylinder since these are likely to be of most physical interest.

We require that the image of $C_2$ under $z(\zeta)$ is $|z| = 1$. We take $2N+2$ equi-spaced collocation points around $C_2$, and enforce at each of these points the real equation

$$|z(\zeta)| = 1. \tag{5.39}$$

We further require that Bernoulli's theorem be satisfied on the hollow vortex boundaries. We take $2N+3$ equi-spaced collocation points around both $C_0$ and $C_1$, and enforce at each of these points the real equation

$$\left|\frac{dw}{dz}\right| \equiv \left|\frac{W_\zeta(\zeta)}{z_\zeta(\zeta)}\right| = c, \tag{5.40}$$

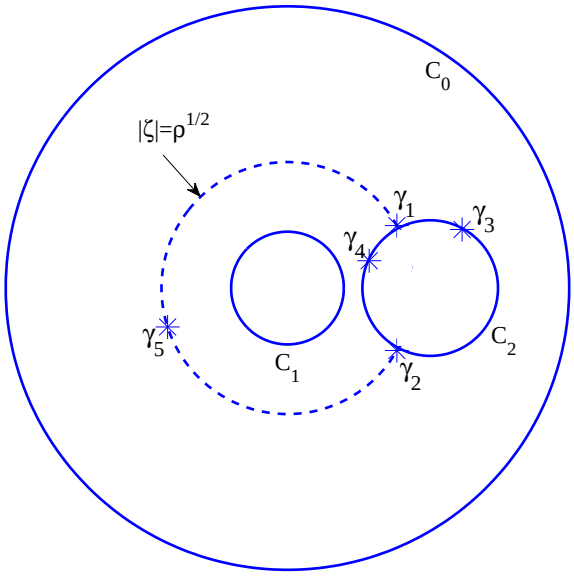


Figure 5.4: Schematic of the preimage circular domain $D_\zeta$ illustrating the locations of the preimages of the five stagnation points $\{\gamma_j \mid j = 1, ..., 5\}$ (these are shown as stars).

where we recall from (5.38) that $c$ is the speed of the fluid on both of the hollow vortex boundaries (to be determined as part of the solution), $W_\zeta(\zeta)$ is given by (5.33), and $z_\zeta(\zeta)$ is given by (5.35). Since we have explicit forms for both functions $W_\zeta(\zeta)$ and $z_\zeta(\zeta)$, the complex velocity function $dw/dz$ does not need to be constructed separately (like it was in Chapters 3 and 4) and is given by the chain rule. Together, (5.39) and (5.40) then comprise a set of $6N + 8$ real equations in $6N + 8$ real unknowns. We proceed using Newton's method to find solutions to our free boundary problem, and thus determine the shapes of the hollow vortex boundaries.

From consideration of the Föppl system, we expect five stagnation points in the flow field. We expect a stagnation point at the front and back of the circular cylinder, two on the circular cylinder surface, and one on the real axis. It was verified numerically, for the solutions we have found, that function $W_\zeta(\zeta)$ does indeed have five such zeroes in $D_\zeta$, and in the locations where they would be expected. Let us label these zeroes by $\{\gamma_j \in \mathbb{C} \mid j = 1, ..., 5\}$. Figure 5.4 shows a schematic of the preimage locations of these stagnation points. $\zeta = \gamma_1$ and $\zeta = \gamma_2 = \overline{\gamma_1}$ are the preimages of the two stagnation points at the front and back of the circular cylinder, $\zeta = \gamma_3$ and $\zeta = \gamma_4 = \rho/\overline{\gamma_3}$ are the preimages of the two stagnation points on the circular cylinder surface, and $\zeta = \gamma_5 = \sqrt{\rho}e^{i\sigma}$ is the preimage of

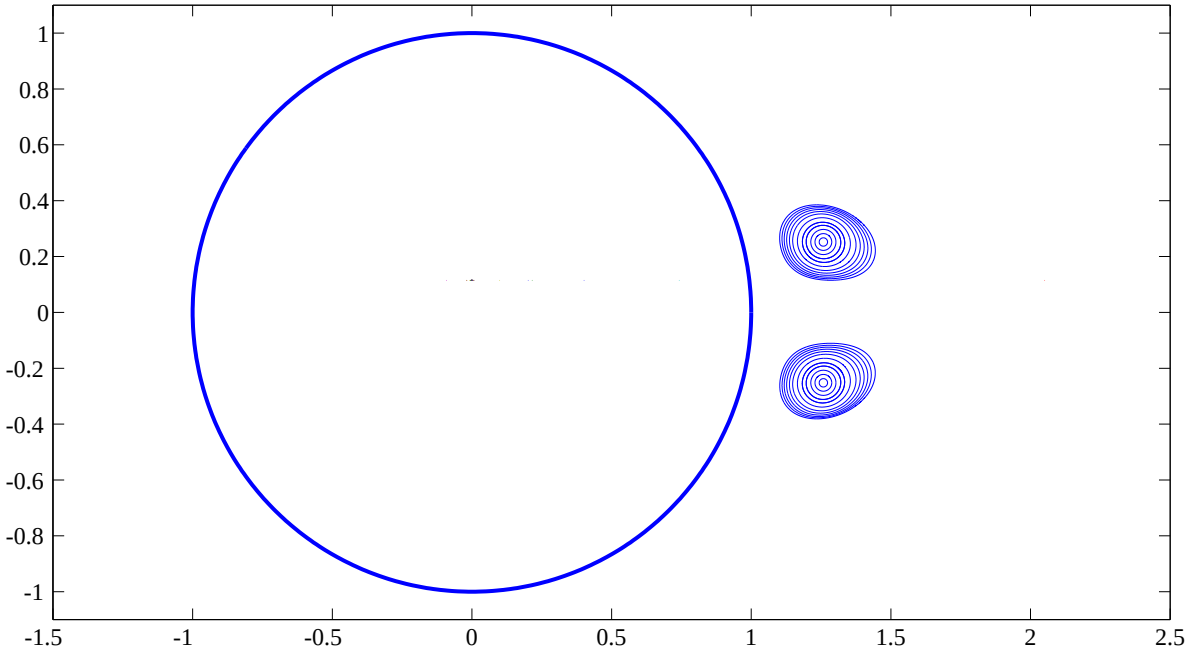


Figure 5.5: Superposition of Föppl hollow vortex pairs of different areas behind a unit radius circular cylinder for $U = 1$ and $\Gamma = 2$. The Föppl equilibria corresponding to $U = 1$ and $\Gamma = 2$ are $1.258 \pm 0.252$i.

the stagnation point on the real axis.

For the remainder of this section, we shall fix $U = 1$ and find solution families for four fixed values of the circulation $\Gamma$. Figures 5.5-5.8 show superpositions of hollow vortices of different areas located behind $|z| = 1$ for $\Gamma = 2, 4, 8, 16.61$, respectively. The value $\Gamma = 16.61$ was chosen by Telib & Zannetti [112]; the family of solutions in Figure 4 of their paper correspond to this value. In each of the Figures 5.5-5.8, the hollow vortices have been 'grown' in area from the corresponding Föppl point vortex equilibrium locations. Figures 5.5-5.8 collectively show the existence of continuous families of hollow vortex equilibria taking a finite range of area values, up to some maximum admissible value, dependent on the choice of $\Gamma$. For $\Gamma = 2, 4, 8$, the hollow vortices essentially exhibit quasi-circular shapes. For $\Gamma = 16.61$, the hollow vortices develop increasingly flattened faces along the sides of their boundaries which are closest together.

We terminated the solution branches when we noticed that the image of circle $C_2$ under $z(\zeta)$ was no longer $|z| = 1$ to within an acceptable numerical accuracy. This phenomenon

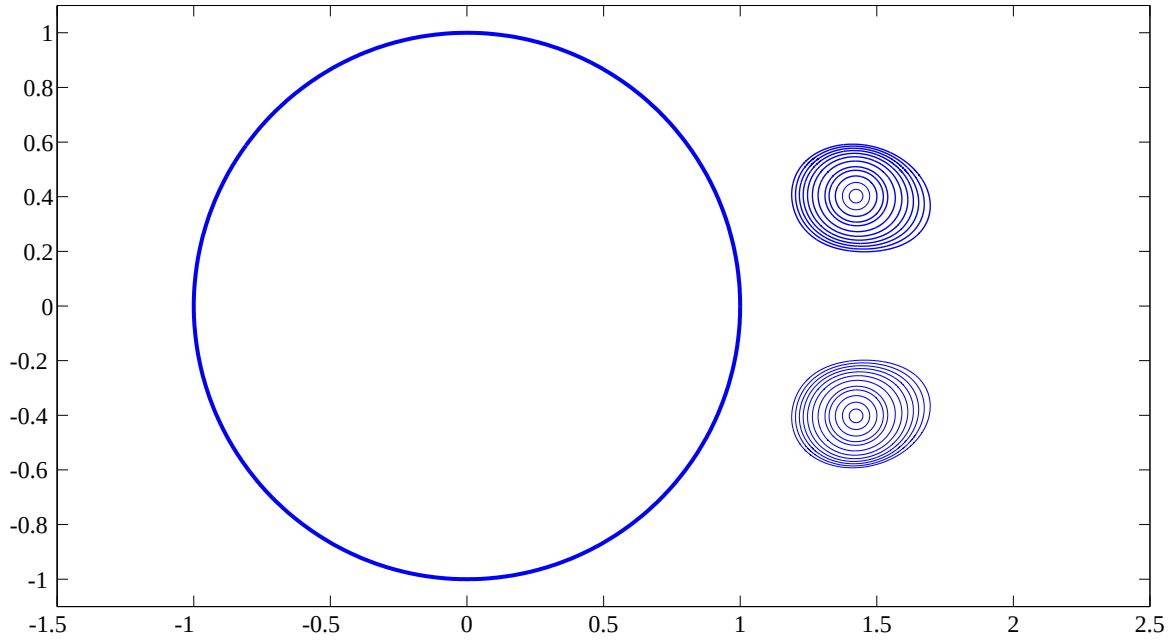


Figure 5.6: Superposition of Föppl hollow vortex pairs of different areas behind a unit radius circular cylinder for $U = 1$ and $\Gamma = 4$. The Föppl equilibria corresponding to $U = 1$ and $\Gamma = 4$ are $1.424 \pm 0.402$i.

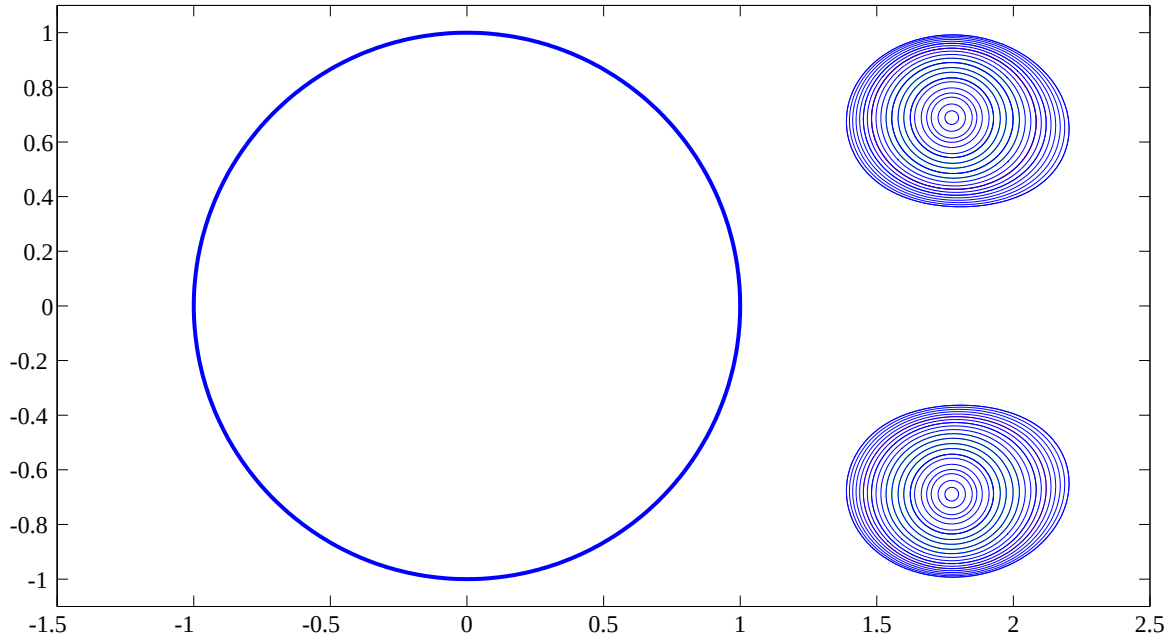


Figure 5.7: Superposition of Föppl hollow vortex pairs of different areas behind a unit radius circular cylinder for $U = 1$ and $\Gamma = 8$. The Föppl equilibria corresponding to $U = 1$ and $\Gamma = 8$ are $1.774 \pm 0.689$i.

always occurred at the same point in the solution branch for any number of modes $N$ and regardless of the choice of collocation points on the boundary circles of $D_\zeta$ (suggesting it is not the manifestation of a numerical 'crowding' problem). The Newton iterations we performed did not encounter any difficulties with convergence, and the values of the coefficients in the Fourier-Laurent series also appeared to continue naturally between two consecutive solutions. For each solution, the boundary circles of $D_\zeta$ were sufficiently separated thus ruling out any possible numerical error associated with the computation of the Schottky-Klein prime function. It is worth noting that Elcrat & Zannetti [41] also experienced "peculiar accuracy issues" in their hollow vortex wake models.

It therefore seems reasonable to conclude that hollow vortex solutions do not exist beyond a particular point in the solution branch, at which point some maximum area configuration has been attained. This conclusion is supported by a qualitative comparison of our hollow vortex solutions for $\Gamma = 16.61$ in Figure 5.8 with those obtained in Figure 4 of Telib & Zannetti [112]. For this value of $\Gamma$, we find a maximum area configuration which appears identical to the one found by Telib & Zannetti [112] (although they do not state explicitly if they actually attained a maximum area configuration), and we observe excellent qualitative agreement between all our hollow vortex boundary shapes and theirs in this particular family, implying that we have traced out precisely the same solutions. This gives us confidence in our analytical-numerical method and the hollow vortex solutions we have computed in Figures 5.5-5.8. The maximum area configurations observed in Figures 5.5-5.8 are not close-to-touching with the circular cylinder; such hollow vortex configurations would appear not to exist. This is in contrast to the findings of Elcrat et al [44] in the case of vortex patches where the maximum area configurations are special limiting cases bounded by the circular cylinder. Until the nature of the existence of our solutions is properly understood, it will remain a matter for future investigation to determine the limiting behaviour of our hollow vortex solutions as their area is increased (if such solutions exist at all).

## 5.8 Summary

Through a combination of numerical and analytical techniques, we have been able to solve the free boundary problem for a pair of hollow vortices of equal and opposite circulation in equilibrium behind a circular cylinder in a uniform stream. We first wrote down a closed-form analytical expression for the complex potential of the system using the specialist techniques of Crowdy [14, 22] and proceeded to solve a non-linear system of equations

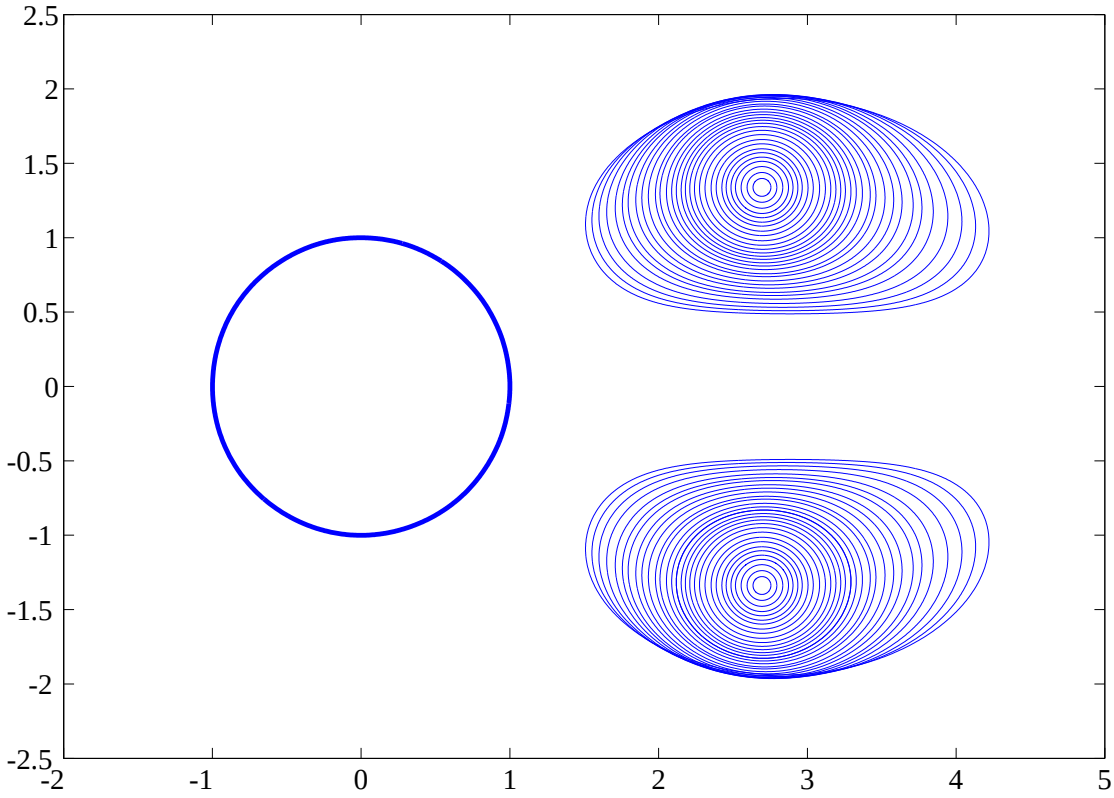


Figure 5.8: Superposition of Föppl hollow vortex pairs of different areas behind a unit radius circular cylinder for $U = 1$ and $\Gamma = 16.61$. The hollow vortices shown here look qualitatively very similar to those shown in Figure 4 of Telib & Zannetti [112]. The Föppl equilibria corresponding to $U = 1$ and $\Gamma = 16.61$ are $2.695 \pm 1.338\mathrm{i}$.

determining a finite set of conformal mapping parameters governing the shapes of the free boundaries of the hollow vortices. Our new solutions are valuable contributions to the expanding body of work on hollow vortex wakes behind bluff bodies.

For four fixed values of the circulation, we were able to determine the hollow vortex free boundary shapes over a finite range of areas, up to some maximum admissible area value. A better understanding regarding the existence of these solutions would throw some light on the limiting behaviour of the hollow vortex shapes as the area is increased. We obtained a particular family of solutions (Figure 5.8) which were found to be qualitatively very similar to those obtained by Telib & Zannetti [112] whose mathematical approach is different to ours. The three solution families we have presented in Figures 5.5-5.7 appear to be new and do not feature in [112].

# Chapter 6

# Multiple steadily translating bubbles in a Hele-Shaw channel

## 6.1 Introduction

For the final free boundary problem we shall solve in this thesis, we will determine the shapes of multiple bubble interfaces as they steadily translate along a Hele-Shaw channel with straight, parallel-sided walls. Of particular interest are the analytical methods that we have chosen to employ to tackle this problem. Crowdy [19] made an attempt at solving this free boundary problem, but it was subsequently found that part of his argument contained erroneous reasoning (Crowdy [private communication]). This chapter presents an alternative, successful approach for solving this free boundary problem.

As discussed in Chapter 1, Hele-Shaw flows are paradigmatic free boundary problems taking a wide variety of forms, and have a rich array of solutions. We shall resolve our free boundary problem using methods related to a special class of scalar Riemann-Hilbert problem (Gakhov [49]). Crowdy [20] recently solved the following special Riemann-Hilbert problem: find function $w(\zeta)$, which is analytic and single-valued in $D_\zeta$, satisfying

$$\mathrm{Re}[\overline{\lambda_j} w(\zeta)] = d_j, \quad \zeta \in C_j, \quad j = 0, 1, ..., M. \tag{6.1}$$

Here, $\lambda_j \in \mathbb{C}$ are constants such that $|\lambda_j| = 1$, and $d_j \in \mathbb{R}$ are constants. Such a problem is intimately related to the classical Schwarz problem in multiply connected domains (Crowdy [18]); indeed, such a problem is retrieved on taking $\lambda_j = 1$ for all $j$ in (6.1). Just like a standard Riemann-Hilbert problem which has an 'inner' and 'outer' region, so

does this special type of Riemann-Hilbert problem: this is encapsulated through the identity $\mathrm{Re}[f(\zeta)] = \frac{1}{2}\left(f(\zeta) + \overline{f(\zeta)}\right)$ and the analytic continuation of $f(\zeta)$ off each boundary component. Crowdy found the solution to this special Riemann-Hilbert problem in the form of a concise integral formula in terms of Schottky-Klein prime functions, the construction of which is related to the method of formulating his generalised Schwarz-Christoffel formulae to multiply connected polygonal domains (Crowdy [13, 16]). We will see that the free boundary problem in consideration in this chapter can be couched in the form of this special Riemann-Hilbert problem solved by Crowdy [20]. We will solve this free boundary problem in its most generality, for any finite number of bubbles in a given assembly, using similar ideas to those in [20]. The final expression for the conformal map revealing the bubble boundary shapes is given as an explicit indefinite integral whose integrand consists of a product of Schottky-Klein prime functions.

## 6.2 Background

There are some relevant prior results pertaining to steady multiple bubbles in Hele-Shaw systems which we will now survey to motivate the free boundary problem of this chapter. An important assumption that is made in each of these works is the exclusion of surface tension effects on the bubble boundaries: from a theoretical standpoint, this makes the problem analytically tractable and allows for exact solutions to be found. Taylor & Saffman [111] found an exact solution for a single bubble in a channel with reflectional symmetry about the channel centreline. Tanveer [109] was able to generalise this solution using elliptic function theory to describe a single asymmetric bubble in the channel. Vasconcelos [117] reported exact solutions for a finite number of steadily translating bubbles in a Hele-Shaw channel. He considered two symmetrical classes of solution pertaining to bubbles which are either symmetrical about the channel centreline or which possess fore-and-aft symmetry. He derived Schwarz-Christoffel type formulae for the conformal mappings determining the bubble interfaces. Adopting the same bubble symmetry assumptions as in [117], Silva & Vasconcelos [104] have recently found exact solutions for a doubly periodic array of multiple symmetrical bubbles, with Schwarz-Christoffel methods again proving to be fruitful. Vasconcelos has also found families of exact solutions for various infinite streams of bubbles in the Hele-Shaw system [115, 116].

Most relevant to our present free boundary problem is the work of Crowdy [21] who found analytical solutions determining the shapes of any finite number of steadily translating

bubbles, with no *a priori* symmetry assumptions concerning the geometrical arrangement of the bubbles, in an unbounded Hele-Shaw cell. He derived analytical expressions for both the complex potential and the conformal map from a bounded multiply connected circular domain to the exterior of the bubble assembly by using conformal mappings to multiply connected slit domains and the Schottky-Klein prime function. The solutions we will present in this chapter can be viewed as the generalisation of the solutions due to Crowdy [21] in the case of the Hele-Shaw channel: our solutions account for the effect of the two channel walls which greatly influence the nature of the free boundary problem (otherwise, the boundary conditions in the two problems are the same). We also shall not make any assumptions about the geometrical arrangements of the bubbles.

## 6.3 Formulation of problem

In this section, we discuss the details of the problem to be solved. We then establish the functional form of several auxiliary functions, before writing down an explicit indefinite integral for the conformal mapping $z(\zeta)$ which will determine the shapes of the free boundaries we seek.

Without loss of generality, we will consider a Hele-Shaw channel of width 2 containing incompressible viscous fluid, extending to infinity $\infty^{\pm}$ in both horizontal directions. In this fluid, we suppose there are $M$ finite-area bubbles. We choose to neglect surface tension effects on their boundaries. Let us label the viscous fluid region by $D_z$ and let us label the boundary of the $j$-th bubble $\partial D_j$. In order to have a steady configuration of bubbles, we suppose that each of the $M$ bubbles translates uniformly left-to-right in the horizontal direction with speed $U > 1$, and that the viscous fluid has uniform speed $V = 1$ in the far field. See Figure 6.1 for a schematic.

Our model will be centred around some simplifying assumptions in order to render the problem analytically tractable. We shall assume that the fluid inside the bubbles has negligible viscosity so that the pressure inside each bubble is constant. We shall assume that the Hele-Shaw channel is horizontally placed so that the effects of gravity can be neglected. As mentioned before, for all the bubbles, we neglect any surface tension effects; this implies that the viscous fluid pressure will have a constant value on each bubble boundary. Finally, we shall also neglect any three-dimensional thin film effects. With these assumptions, we shall first formulate the free boundary problem to be solved in the physical $z = (x + \mathrm{i}y)$-

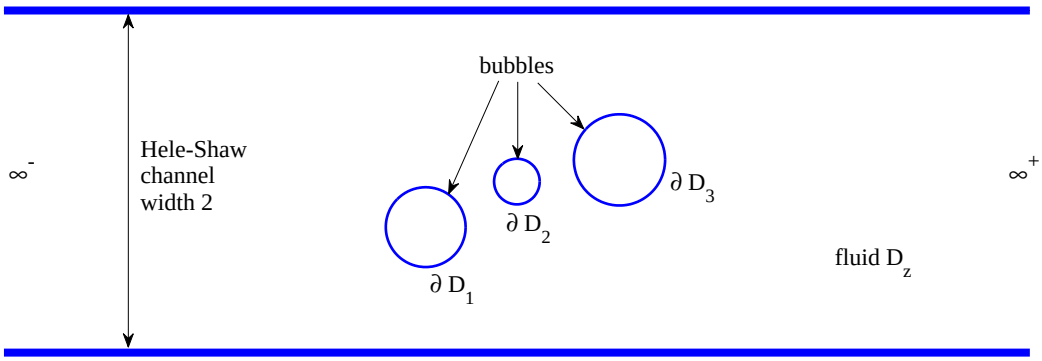


Figure 6.1: Schematic of a Hele-Shaw channel of width 2 containing an assembly of steadily translating bubbles. In the case illustrated, the assembly contains 3 bubbles. The shapes of the bubble boundaries, in a co-travelling frame with the bubbles, are to be determined.

plane.

In a laboratory frame of reference (not co-travelling with the bubble assembly), let

$$F(z,t) = \phi(x,y,t) + \mathrm{i}\psi(x,y,t) \tag{6.2}$$

be the complex potential describing the flow. Here, $\phi$ is the velocity potential and $\psi$ is the streamfunction. In this laboratory frame, we shall assume that the motion of the incompressible viscous fluid in our Hele-Shaw channel is governed by Darcy's law:

$$\mathbf{v} = \nabla\phi = -\frac{b^2}{12\mu}\nabla p. \tag{6.3}$$

Here, $\mathbf{v}$ is the averaged fluid velocity across the channel, $p$ is the viscous fluid pressure, $b$ is the channel width, and $\mu$ is the viscosity. On taking the divergence of (6.3), we obtain Laplace's equation

$$\nabla\cdot\mathbf{v} = \nabla^2\phi = -\frac{b^2}{12\mu}\nabla^2 p = 0 \tag{6.4}$$

implying that our free boundary problem is amenable to techniques of complex analysis.

From (6.3), it is immediate that

$$\phi = -\frac{b^2}{12\mu}p + \text{constant}. \tag{6.5}$$

The bubble assembly is assumed to be steadily translating along the channel with speed $U$, hence the complex potential $F(z,t)$ in (6.2) must be of the form

$$F(z,t) = \tau(z') \tag{6.6}$$

for some function $\tau(z')$, where

$$z' = z - Ut. \tag{6.7}$$

Let $w(z')$ be the complex potential describing the flow in a co-travelling frame of reference with the bubbles. Then $w(z)$ is related to $\tau(z)$ by

$$w(z) = \tau(z) - Uz, \tag{6.8}$$

where we have dropped the prime notation with the understanding that we will be henceforth working in the co-travelling frame with the bubbles. The viscous fluid is assumed to have unit speed in the far-field. Thus, as $z \to \infty^{\pm}$, we require

$$w(z) = (1-U)z + \text{locally analytic function}. \tag{6.9}$$

Apart from this simple pole at infinity, the complex potential function $w(z)$ is analytic everywhere in the viscous fluid region.

Taking the real part of (6.8) evaluated on the bubble boundaries, i.e. for $z \in \partial D_j$, $j = 1, ..., M$, yields

$$\mathrm{Re}[\tau(z)] = \mathrm{Re}[w(z) + Uz] = -\frac{b^2}{12\mu}p + \text{constant}. \tag{6.10}$$

Recall that, in the laboratory frame, the viscous fluid pressure $p$ is constant on each bubble boundary. Thus:

$$\mathrm{Re}[\tau(z)] = \mathrm{Re}[w(z) + Uz] = \text{constant}. \tag{6.11}$$

In the co-travelling frame with the bubble assembly, the bubble boundaries are necessarily

streamlines of the flow; thus

$$\mathrm{Im}[w(z)] = \text{constant} \tag{6.12}$$

for $z \in \partial D_j$, $j = 1, ..., M$. In light of (6.9), the channel walls $y = \pm 1$ are also streamlines of the flow since

$$\mathrm{Im}[w(z)] = \pm(1 - U) \tag{6.13}$$

for $y = \pm 1$.

In order to determine the shapes of the bubbles (which are in equilibrium in the co-travelling frame), we shall construct the conformal map $z(\zeta)$ from some bounded $M + 1$ connected circular domain $D_\zeta$ in a parametric $\zeta$-plane to the $M+1$ connected fluid region $D_z$ exterior to $M$ bubbles in a $z$-plane. Label the unit circle by $C_0$ and label the $M$ inner circular boundaries as $C_1, ..., C_M$. Let the centre and radius of $C_j$ be $\delta_j$ and $q_j$ respectively. A schematic of $D_\zeta$ is shown in Figure 6.2 in the case where $M = 3$ (quadruply connected). Let $C_0$ map to the channel walls: this implies that $z(\zeta)$ will necessarily have two logarithmic singularities on $C_0$. By a rotational freedom afforded by the Riemann-Koebe mapping theorem, we can place one of these logarithmic singularities at $\zeta = 1$; the other will be at some point $\zeta = \alpha$ on $C_0$ to be found as part of the solution. Let the interior circles $C_1, ..., C_M$ map to the bubble boundaries $\partial D_1, ..., \partial D_M$.

## 6.4 Function $W(\zeta)$

First, we construct an explicit expression for the complex potential $W(\zeta)$ in the $\zeta$-plane. Function $W(\zeta)$ is related to the complex potential $w(z)$ in the $z$-plane co-travelling with the bubble assembly through the composition

$$W(\zeta) = w(z(\zeta)). \tag{6.14}$$

From conditions (6.12) and (6.13), this function $W(\zeta)$ must be such that

$$\mathrm{Im}[W(\zeta)] = \text{piecewise constant}, \quad \zeta \in C_0, \tag{6.15}$$

and

$$\mathrm{Im}[W(\zeta)] = \gamma_j, \quad \zeta \in C_j, \quad j = 1, ..., M. \tag{6.16}$$

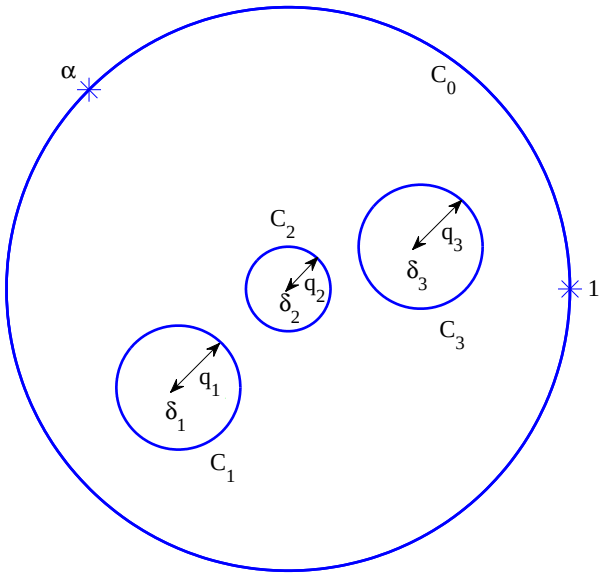


Figure 6.2: The preimage bounded multiply connected circular domain $D_\zeta$. The case of a quadruply connected domain is illustrated, to be conformally equivalent to the physical domain in Figure 6.1. The unit circle $|\zeta| = 1$ maps to the channel walls with $\zeta = 1$ and $\zeta = \alpha$ being the preimages of $\infty^+$ and $\infty^-$ (the ends of the channel). The circle $C_j$ maps, under $z(\zeta)$, to the boundary of bubble $\partial D_j$ (for $j = 1, 2, 3$).

Here, $\gamma_j \in \mathbb{R}$ are constants. This ensures that the bubble boundaries and the channel walls are streamlines. We note that function $W(\zeta)$ can be interpreted as the conformal mapping from $D_\zeta$ to an infinite horizontal channel of width $2(U-1)$ with $M$ finite-length horizontal slits. See Figure 6.3. $W(\zeta)$ is required to be a single-valued analytic function everywhere in the interior of $D_\zeta$.

From (6.15) and (6.16), we notice that the function

$$\exp W(\zeta) \tag{6.17}$$

must have constant argument on each of the $M + 1$ boundary circles of $D_\zeta$. Recall the conformal radial slit mapping of (2.60):

$$\chi(\zeta; \zeta_1, \zeta_2) = \frac{\omega(\zeta, \zeta_1)\omega(\zeta, 1/\overline{\zeta_1})}{\omega(\zeta, \zeta_2)\omega(\zeta, 1/\overline{\zeta_2})}. \tag{6.18}$$

Recall from Chapter 2 that this function $\chi(\zeta; \zeta_1, \zeta_2)$ has constant argument on each of the

boundary circles of $D_\zeta$, a simple zero at $\zeta = \zeta_1$ and a simple pole at $\zeta = \zeta_2$. Now consider

$$\exp W(\zeta) = a\left(\chi(\zeta; 1, \alpha)\right)^b, \tag{6.19}$$

where $a \in \mathbb{C}$ and $b \in \mathbb{R}$ are constants, and $\zeta = 1$ and $\zeta = \alpha$ are the two points lying on $C_0$ which map to the two ends of the channel at infinity $\infty^{\pm}$. Since $\zeta = 1$ and $\zeta = \alpha$ are two points on $C_0$, (6.18) becomes

$$\chi(\zeta; 1, \alpha) = \frac{\omega^2(\zeta, 1)}{\omega^2(\zeta, \alpha)}. \tag{6.20}$$

Hence, it follows from (6.19), on taking a logarithm, that

$$W(\zeta) = c + d \log\left(\frac{\omega(\zeta, 1)}{\omega(\zeta, \alpha)}\right), \tag{6.21}$$

where $c$ is an inconsequential complex constant and $d \in \mathbb{R}$ is another constant. Notice that this function (6.21) satisfies the requirements (6.15) and (6.16). This function (6.21) also has logarithmic singularities at $\zeta = 1$ and $\zeta = \alpha$. Passing through either $\zeta = 1$ or $\zeta = \alpha$ results in a $\pi\mathrm{i}$ jump in the logarithm. Hence, in order that the channel width is $2$, we require

$$z(\zeta) = \frac{2}{\pi}\log(\zeta - 1) + \text{locally analytic function}, \quad \zeta \to 1, \tag{6.22}$$

and

$$z(\zeta) = -\frac{2}{\pi}\log(\zeta - \alpha) + \text{locally analytic function}, \quad \zeta \to \alpha. \tag{6.23}$$

Recall that, in the co-travelling frame with the bubbles, the fluid far-field looks like a uniform flow of speed $1 - U$ (translating right-to-left), i.e.

$$w(z) = (1 - U)z + \text{locally analytic function}, \quad z \to \infty^{\pm}. \tag{6.24}$$

Thus

$$W(\zeta) = \frac{2(1 - U)}{\pi}\log\left(\frac{\omega(\zeta, 1)}{\omega(\zeta, \alpha)}\right). \tag{6.25}$$

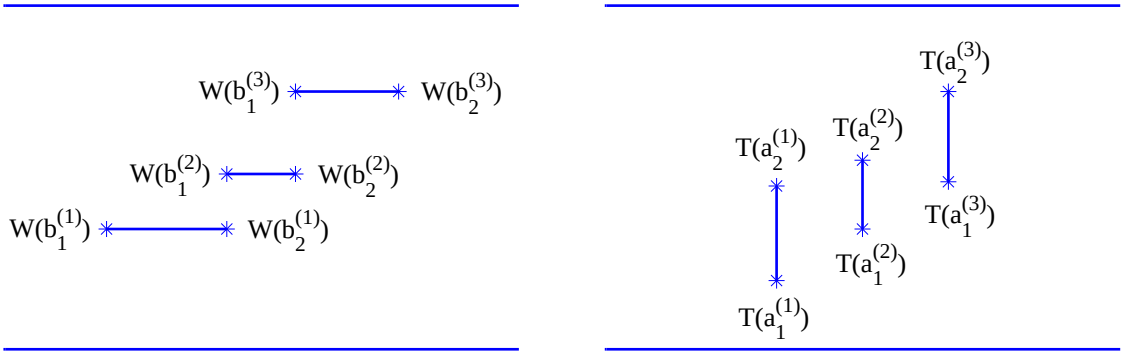


Figure 6.3: Schematic showing the conformally equivalent image domains of $D_\zeta$ (as in Figure 6.2) under the conformal mappings $W(\zeta)$ [left] and $T(\zeta)$ [right]. Both are infinite channels with three finite-length slits which are either horizontally or vertically aligned. The infinite channel in the $W$-plane has width $2(U-1)$ whilst the infinite channel in the $T$-plane has width 2. The slit end-points are labelled accordingly.

## 6.5 Function $W_\zeta(\zeta)$

The derivative of function $W(\zeta)$ in (6.25) with respect to $\zeta$ is given by

$$W_\zeta(\zeta) = \frac{2(1-U)}{\pi}\left(\frac{\omega_\zeta(\zeta,1)}{\omega(\zeta,1)} - \frac{\omega_\zeta(\zeta,\alpha)}{\omega(\zeta,\alpha)}\right), \tag{6.26}$$

where $\omega_\zeta(\zeta,\cdot)$ denotes the derivative with respect to $\zeta$ of the Schottky-Klein prime function. Let $\{b_1^{(j)}, b_2^{(j)} \in C_j \mid j = 1,...,M\}$ be the set of preimages of the $2M$ horizontal slit end-points in the $W$-plane (see Figure 6.3). Function $W_\zeta(\zeta)$ has $2M$ simple zeroes at $\{b_1^{(j)}, b_2^{(j)} \in C_j \mid j = 1,...,M\}$; these are simple zeroes because the arguments of $W(\zeta;\beta) - W(b_1^{(j)};\beta)$ and $W(\zeta;\beta) - W(b_2^{(j)};\beta)$ change by $2\pi$ as $\zeta$ passes through these points. These points $\{b_1^{(j)}, b_2^{(j)} \in C_j \mid j = 1,...,M\}$ are also the preimages of the $2M$ stagnation points in the $z$-plane (there are two stagnation points lying on each of the $M$ bubbles); these preimages can in principle be computed from (6.26), but this is not necessary for our present purposes.

## 6.6 Function $T(\zeta)$

We now construct an explicit expression for the function $T(\zeta)$ which we will now define. Function $T(\zeta)$ is related to the complex potential $\tau(z)$ through the composition

$$T(\zeta) = \tau(z(\zeta)). \tag{6.27}$$

In light of (6.8), we can thus define

$$T(\zeta) = W(\zeta) + Uz(\zeta). \tag{6.28}$$

From the conditions (6.11), we require

$$\mathrm{Re}[W(\zeta) + Uz(\zeta)] = \nu_j, \quad \zeta \in C_j, \quad j = 1, ..., M. \tag{6.29}$$

Here, $\nu_j \in \mathbb{R}$ are constants. Noting that, due to channel walls, we must have

$$\mathrm{Im}[z(\zeta)] = \text{piecewise constant}, \quad \zeta \in C_0, \tag{6.30}$$

we can now see that our free boundary problem is the following special type of Riemann-Hilbert problem: find function $T(\zeta)$, analytic and single-valued inside $D_\zeta$, satisfying

$$\mathrm{Im}[T(\zeta)] = \text{piecewise constant}, \quad \zeta \in C_0, \tag{6.31}$$

owing to the conditions (6.15), (6.16) and (6.30), and

$$\mathrm{Re}[T(\zeta)] = \text{constant}, \quad \zeta \in C_j, \quad j = 1, ..., M, \tag{6.32}$$

owing to the conditions (6.29). This type of Riemann-Hilbert problem is of the same type solved by Crowdy in [20]. The success of his approach came from introducing the auxiliary conformal mapping $\eta(\zeta; \beta)$ taking $D_\zeta$ to a bounded multiply connected circular slit domain in an $\eta$-plane; recall these maps are of the functional form given in (2.53):

$$\eta(\zeta; \beta) = \frac{\omega(\zeta, \beta)}{|\beta|\omega(\zeta, 1/\overline{\beta})}. \tag{6.33}$$

Let $\zeta = \gamma_1^{(j)}$ and $\zeta = \gamma_2^{(j)}$ be the preimages of the two slit end-points on the $j$-th circular slit; these will lie on the interior circle $C_j$, $j = 1, ..., M$. Note that if one specifies $D_\zeta$ and a

value of $\zeta = \beta$, the set of points $\{\gamma_1^{(j)}, \gamma_2^{(j)} \in C_j \mid j = 1, ..., M\}$ is completely determined. The derivative of $\eta(\zeta; \beta)$ with respect to $\zeta$ has simple zeroes at these points:

$$\eta_\zeta(\gamma_1^{(j)}; \beta) = \eta_\zeta(\gamma_2^{(j)}; \beta) = 0, \quad j = 1, ..., M. \tag{6.34}$$

These $2M$ zeroes of $\eta_\zeta(\zeta; \beta)$ are simple zeroes since the arguments of $\eta(\zeta; \beta) - \eta(\gamma_1^{(j)}; \beta)$ and $\eta(\zeta; \beta) - \eta(\gamma_2^{(j)}; \beta)$ change by $2\pi$ as $\zeta$ passes through these points.

From the requirements (6.31) and (6.32), and then following the same arguments in Crowdy [20], it can be shown that function

$$\eta \hat{T}_\eta(\eta) \tag{6.35}$$

must have constant argument on each boundary component in the auxiliary $\eta$-plane, where

$$\hat{T}(\eta(\zeta; \beta)) = T(\zeta), \tag{6.36}$$

and $\hat{T}_\eta(\eta)$ denotes the derivative with respect to $\eta$ of $\hat{T}(\eta)$. In light of the conditions (6.22) and (6.23), we need

$$T(\zeta) = \frac{2}{\pi} \log(\zeta - 1) + \text{locally analytic function}, \quad \zeta \to 1, \tag{6.37}$$

and

$$T(\zeta) = -\frac{2}{\pi} \log(\zeta - \alpha) + \text{locally analytic function}, \quad \zeta \to \alpha. \tag{6.38}$$

We note that function $T(\zeta)$ can be interpreted as the conformal mapping from $D_\zeta$ to an infinite horizontal channel of width 2 with $M$ finite-length vertical slits: $C_0$ mapping to the channel walls, and $C_1, ..., C_M$ mapping to the $M$ vertical slits. See Figure 6.3. Let $\zeta = a_1^{(j)}$ and $\zeta = a_2^{(j)}$ be the preimages of the two slit end-points on the $j$-th vertical slit; these will lie on the interior circle $C_j$. The set of points $\{a_1^{(j)}, a_2^{(j)} \in C_j \mid j = 1, ..., M\}$ is unknown *a priori*, and must be found as part of the solution. The derivative of $T(\zeta)$ with respect to $\zeta$ has simple zeroes at these points:

$$T_\zeta(a_1^{(j)}) = T_\zeta(a_2^{(j)}) = 0, \quad j = 1, ..., M. \tag{6.39}$$

These $2M$ zeroes of $T_\zeta(\zeta)$ are simple zeroes since the arguments of $T(\zeta; \beta) - T(a_1^{(j)}; \beta)$ and $T(\zeta; \beta) - T(a_2^{(j)}; \beta)$ change by $2\pi$ as $\zeta$ passes through these points. The construction of this mapping $T(\zeta)$ is the vital cornerstone upon which our solution scheme is based.

## 6.7 Function $T_\zeta(\zeta)$

Function $\eta\hat{T}_\eta(\eta)$ must have constant argument on each of the boundary components in the $\eta$-plane. We now construct a functional form for $\eta\hat{T}_\eta(\eta)$ and use it to deduce an expression for $T_\zeta(\zeta)$ .

Our strategy is to specify some $M+1$ connected circular domain $D_\zeta$ and find the conformal map $z(\zeta)$ determining the bubble shapes. It is advantageous to specify $D_\zeta$ *a priori* since the conformal moduli defining the Schottky-Klein prime function will not have to be re-computed on each iterative step in our solution scheme. Furthermore, choosing these conformal moduli is analogous to prescribing the bubble areas and the bubble centroids.

We shall now build the function $\eta\hat{T}_\eta(\eta)$. Note that

$$\eta\hat{T}_\eta(\eta) \equiv \eta(\zeta;\beta)\frac{T_\zeta(\zeta)}{\eta_\zeta(\zeta;\beta)}. \tag{6.40}$$

From (6.40), we see that we require function $\eta\hat{T}_\eta(\eta)$ to have a simple zero at $\zeta=\beta$ (function $\eta(\zeta;\beta)$ has a simple zero at $\zeta=\beta$) and simple poles at $\{\gamma_1^{(j)},\gamma_2^{(j)}\in C_j \mid j=1,...,M\}$ (recall (6.34)). In light of the required behaviours (6.37) and (6.38), $\eta\hat{T}_\eta(\eta)$ needs to have simple poles at $\zeta=1$ and $\zeta=\alpha$. We also need $\eta\hat{T}_\eta(\eta)$ to have simple zeroes at $\{a_1^{(j)},a_2^{(j)}\in C_j \mid j=1,...,M\}$ (recall (6.39)). Recall the conformal radial slit mapping of (2.62):

$$\xi(\zeta;\zeta_3,\zeta_4) = \frac{\omega(\zeta,\zeta_3)}{\omega(\zeta,\zeta_4)}. \tag{6.41}$$

Function $\xi(\zeta;\zeta_3,\zeta_4)$ has constant argument on each of the boundary circles of $D_\zeta$. It also has a simple zero at $\zeta=\zeta_3$ and a simple pole at $\zeta=\zeta_4$.

Consider the following function:

$$\prod_{j=1}^{M}\xi(\zeta;a_1^{(j)},\gamma_1^{(j)})\xi(\zeta;a_2^{(j)},\gamma_2^{(j)}). \tag{6.42}$$

Being a product of $2M$ radial slit mappings of the form (6.41), function (6.42) has constant argument on each of the boundary circles of $D_\zeta$. It also has simple zeroes at $\{a_1^{(j)},a_2^{(j)}\in C_j \mid j=1,...,M\}$ and simple poles at $\{\gamma_1^{(j)},\gamma_2^{(j)}\in C_j \mid j=1,...,M\}$, as can easily be

seen from (6.41). Next consider the function:

$$\xi(\zeta;1,\alpha)\chi(\zeta;\beta,1)=\frac{\omega(\zeta,\beta)\omega(\zeta,1/\overline{\beta})}{\omega(\zeta,1)\omega(\zeta,\alpha)}. \tag{6.43}$$

where function $\chi(\zeta;\beta,1)$ is the radial slit mapping of (6.18). This function has two simple zeroes at $\zeta=\beta$ and $\zeta=1/\overline{\beta}$, and two simple poles at $\zeta=1$ and $\zeta=\alpha$. Being a product of two radial slit maps (albeit of different type), function (6.43) has constant argument on each of the boundary circles of $D_\zeta$.

Consider, thus, the product of functions (6.42) and (6.43). Let

$$\eta\hat{T}_\eta(\eta)=\mathcal{B}\chi(\zeta;\beta,1)\xi(\zeta;1,\alpha)\prod_{j=1}^{M}\xi(\zeta;a_1^{(j)},\gamma_1^{(j)})\xi(\zeta;a_2^{(j)},\gamma_2^{(j)}), \tag{6.44}$$

where $\mathcal{B}\in\mathbb{C}$ is a constant, and $\{a_1^{(j)},a_2^{(j)}\in C_j\mid j=1,...,M\}$ is the set of preimages of the slit end-points in the $T$-plane, to be determined. Being a product of radial slit maps, this function has constant argument on $C_0,C_1,...,C_M$, as required. It has simple poles at $\zeta=1$ and $\zeta=\alpha$, simple poles at $\{\gamma_1^{(j)},\gamma_2^{(j)}\in C_j\mid j=1,...,M\}$, and simple zeroes at $\{a_1^{(j)},a_2^{(j)}\in C_j\mid j=1,...,M\}$, as required. The simple zero $\zeta=\beta$ of the map $\eta(\zeta;\beta)$ can be chosen arbitrarily; this is demonstrated in an appendix of Crowdy [20]. Written out in full, (6.44) is

$$\eta\hat{T}_\eta(\eta)\equiv\eta(\zeta;\beta)\frac{T_\zeta(\zeta)}{\eta_\zeta(\zeta;\beta)}=\mathcal{B}\frac{\omega(\zeta,\beta)\omega(\zeta,1/\overline{\beta})}{\omega(\zeta,1)\omega(\zeta,\alpha)}\prod_{j=1}^{M}\frac{\omega(\zeta,a_1^{(j)})\omega(\zeta,a_2^{(j)})}{\omega(\zeta,\gamma_1^{(j)})\omega(\zeta,\gamma_2^{(j)})}. \tag{6.45}$$

It then follows that

$$T_\zeta(\zeta)=\mathcal{B}\left(\frac{\omega_\zeta(\zeta,\beta)\omega(\zeta,1/\overline{\beta})-\omega_\zeta(\zeta,1/\overline{\beta})\omega(\zeta,\beta)}{\omega(\zeta,1)\omega(\zeta,\alpha)}\right)\prod_{j=1}^{M}\frac{\omega(\zeta,a_1^{(j)})\omega(\zeta,a_2^{(j)})}{\omega(\zeta,\gamma_1^{(j)})\omega(\zeta,\gamma_2^{(j)})}. \tag{6.46}$$

The constant $\mathcal{B}$ is calculated *a posteriori* by enforcing the conditions (6.37) and (6.38). It is found to be:

$$\mathcal{B}=\frac{2}{\pi}\left(\frac{\omega(1,\alpha)}{\omega_\zeta(1,\beta)\omega(1,1/\overline{\beta})-\omega_\zeta(1,1/\overline{\beta})\omega(1,\beta)}\right)\prod_{j=1}^{M}\frac{\omega(1,\gamma_1^{(j)})\omega(1,\gamma_2^{(j)})}{\omega(1,a_1^{(j)})\omega(1,a_2^{(j)})}. \tag{6.47}$$

Our construction of (6.46) is reminiscent of two methodologies of Crowdy using conformal slit mappings as 'building block' functions in order to construct some desired function

solving a particular problem: in [13, 16], this desired function was a Schwarz-Christoffel mapping to a multiply connected polygonal domain, while in [20], this desired function was the general solution of the special Riemann-Hilbert problem of the type we are solving. Note that the special type of Riemann-Hilbert problem we are solving in this chapter (i.e. finding single-valued analytic function $T(\zeta)$ solving (6.31) and (6.32)) has boundary conditions of precisely the Schwarz-Christoffel type: it is therefore not surprising that our construction of (6.46) bears some resemblance to the two methodologies in the works of [13, 16, 20].

## 6.8 Conformal map $z(\zeta)$

In light of definition (6.28), the conformal map $z(\zeta)$ we seek will then follow from the integral

$$z(\zeta) = \mathcal{A} + \frac{1}{U}\int_{\zeta_0}^{\zeta} [T_\zeta(\zeta') - W_\zeta(\zeta')]\, d\zeta', \tag{6.48}$$

where $\mathcal{A} \in \mathbb{C}$ is a constant, $\zeta_0 \in \mathbb{C}$ is an arbitrary point inside $D_\zeta$, and expressions for $T_\zeta(\zeta)$ and $W_\zeta(\zeta)$ are given in (6.46) and (6.26), respectively.

## 6.9 Characterisation of the solutions

Let us fix the value of $U$. The number of free real parameters in (6.48) is $3M + 4$: the $3M$ conformal moduli of $D_\zeta$, the complex constant $\mathcal{A}$, and the complex number $\beta$. The value of $\beta$ (the simple zero of $\eta(\zeta;\beta)$) can be selected arbitrarily. There are three real degrees of freedom associated with the Riemann-Koebe mapping theorem and we used up one of these freedoms by insisting that $\zeta = 1$ maps to infinity at one end of the channel. The remaining two real degrees of freedom can be used to fix the value of the complex constant $\mathcal{A}$. This leaves a total of $3M$ free parameters; these correspond to the $3M$ conformal moduli of $D_\zeta$. If we specify the $3M$ conformal moduli of $D_\zeta$, the values of $\{\gamma_1^{(j)}, \gamma_2^{(j)} \mid j = 1, ...M\}$ are set. We are then left to determine the following parameters:

$$\alpha \in C_0, \quad \{a_1^{(j)}, a_2^{(j)} \in C_j \mid j = 1, ..., M\}. \tag{6.49}$$

We will now present the equations to be solved in order to determine the parameters of the conformal mapping $z(\zeta)$. Once we have a solution to these equations, functions $T_\zeta(\zeta)$ and $W_\zeta(\zeta)$ will be fully determined, and the conformal map $z(\zeta)$ found through the integral

(6.48).

First, we must ensure that the $M$ finite-length slits in the $T$-plane are vertical and perpendicular to the channel walls. As one traces out an interior circle $C_j$ in the preimage $\zeta$-plane, on which $\zeta = \delta_j + q_j \mathrm{e}^{\mathrm{i}\theta}$, the corresponding image under the map $T(\zeta)$ in the $T$-plane must be a vertical slit. We require:

$$\mathrm{Re}[T_\zeta(\delta_j + \mathrm{i}q_j)] = 0, \quad j = 1, ..., M. \tag{6.50}$$

To see why, consider the Taylor expansion of function $T(\zeta) = T(\delta_j + q_j \mathrm{e}^{\mathrm{i}\theta})$ about an arbitrary point $\zeta_*^{(j)} = \delta_j + q_j \mathrm{e}^{\mathrm{i}\theta_*^{(j)}} \in C_j$ as a function of $\theta$:

$$T(\theta) = T(\theta_*^{(j)}) + (\theta - \theta_*^{(j)}) T_\theta(\theta_*^{(j)}) + \mathcal{O}(\theta - \theta_*^{(j)})^2. \tag{6.51}$$

Here, $\theta_*^{(j)}$ is close to $\theta$ (and the higher order terms can be neglected). For the slits to be vertical, the difference between any two points on the slit must have zero real part:

$$\mathrm{Re}[T(\theta) - T(\theta_*^{(j)})] = 0, \quad j = 1, ..., M, \tag{6.52}$$

i.e.

$$\mathrm{Re}[T_\theta(\theta_*^{(j)})] \equiv \mathrm{Re}[T_\zeta(\zeta_*^{(j)}) \mathrm{i} q_j \mathrm{e}^{\mathrm{i}\theta_*^{(j)}}] = 0, \quad j = 1, ..., M. \tag{6.53}$$

As a matter of convenience, we pick $\theta_*^{(j)} = \pi/2$ in (6.53) so that it suffices to enforce the following $M$ real equations:

$$\mathrm{Re}[T_\zeta(\delta_j + \mathrm{i}q_j)] = 0, \quad j = 1, ..., M. \tag{6.54}$$

In order to ensure that $T(\zeta)$ is everywhere single-valued in $D_\zeta$, there are $M$ further real equations to enforce. A $2\pi$ traversal of $C_j$ should correspond to returning to the same point on the $j$-th vertical slit, i.e.

$$\mathrm{Im}\left[\oint_{C_j} T_\zeta(\zeta') d\zeta'\right] = 0, \quad j = 1, ..., M. \tag{6.55}$$

The conditions (6.55) will then, in turn, imply that the conformal map $z(\zeta)$ is everywhere single-valued in $D_\zeta$ (recall that $W(\zeta)$ is single-valued by construction).

We have one further real equation to enforce in order to ensure that the channel walls in the $T$-plane are horizontal. It is

$$\mathrm{Im}[T_\zeta(\mathrm{i})] = 0 \tag{6.56}$$

and can be derived in a similar fashion to (6.54).

Newton's method was used to solve the set of $2M + 1$ real equations (6.54), (6.55) and (6.56) for the following $2M + 1$ real parameters:

$$\alpha, \quad \{\arg[a_1^{(j)} - \delta_j],\ \arg[a_2^{(j)} - \delta_j] \mid j = 1, ..., M\}. \tag{6.57}$$

We will now illustrate the foregoing theory by considering some specific examples of various bubble configurations. Henceforth, we shall set $U = 2$; it is demonstrated in Vasconcelos [117] that all other bubble assemblies corresponding to different values of $U$ can be obtained from the $U = 2$ solutions by a simple re-scaling. Taylor & Saffman [111] considered the case of a reflectionally symmetric bubble about the channel centreline, and Tanveer [109] considered the case of a single bubble with fore-and-aft symmetry with no symmetry about the channel centreline: both the solutions of [109] and [111] should be able to be retrieved using our solution scheme. We shall present examples of steadily translating assemblies of two, three and five bubbles.

Figure 6.4 shows an example of two bubbles whose centroids are aligned along the channel centreline and which are reflectionally symmetric about the channel centreline. Given their up-down symmetry about the channel centreline, this pair of bubbles in Figure 6.4 could have been generated using the solution scheme presented by Vasconcelos [117]. In fact, we were able to successfully recover the same bubbles shapes as in Figure 6.4 using the analytical solutions of Vasconcelos [117]. Figure 6.5 shows an example of two asymmetric bubbles. Three streamlines in the local flow field of the bubbles have also been plotted: these streamlines provide a qualitative check on the solutions. Figure 6.6 shows an example of the bubble shapes for a particular asymmetric assembly of three bubbles.

The versatility and generality of our method can be demonstrated through solving for parameters yielding more than three bubbles in some asymmetric configuration. We chose $M = 5$ bubbles by way of example (a higher number of bubbles can be treated in a similar manner). It appears that this is the first time these most general bubble solutions have been

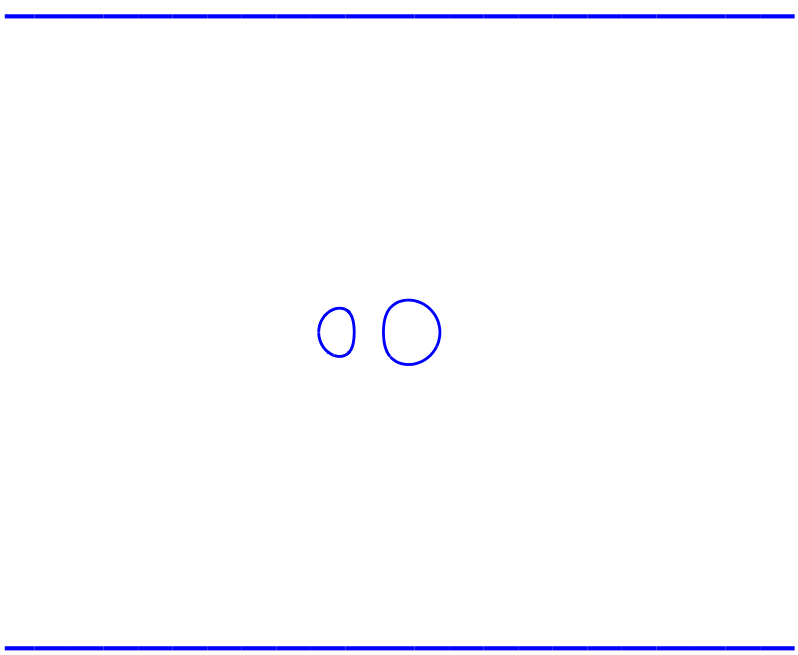

Figure 6.4: An example of two bubbles whose centroids lie on the channel centreline and which are reflectionally symmetry about it. To obtain these bubbles, we chose the following conformal moduli of $D_\zeta$: $\delta_1 = 0$, $\delta_2 = 0.185$, $q_1 = 0.075$, $q_2 = 0.05$.

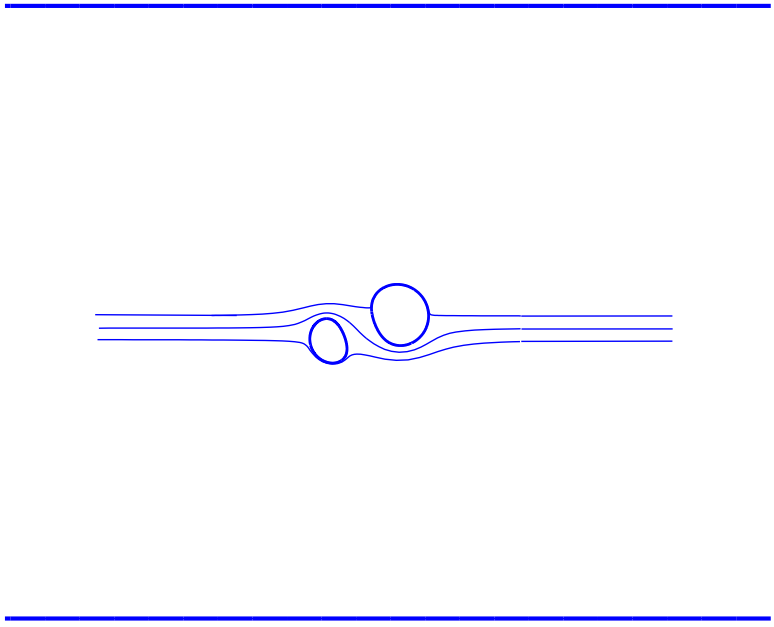

Figure 6.5: An example of two bubbles in a general asymmetric configuration with three typical streamlines superposed. To obtain these bubbles, the following conformal moduli of $D_\zeta$ were chosen: $\delta_1 = 0$, $\delta_2 = 0.185 + 0.07\mathrm{i}$, $q_1 = 0.075$, $q_2 = 0.05$.

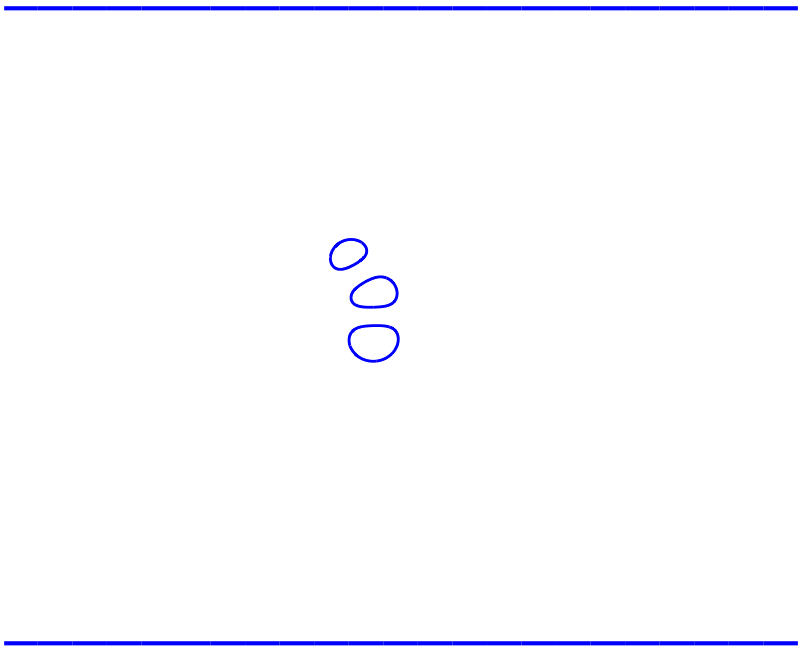

Figure 6.6: An example of three bubbles in a general asymmetric configuration. For this bubble assembly, the following conformal moduli of $D_\zeta$ were picked: $\delta_1 = 0.1$, $\delta_2 = 0.175\mathrm{e}^{\pi\mathrm{i}/4}$, $\delta_3 = 0.19\mathrm{e}^{-\pi\mathrm{i}/5}$, $q_1 = 0.045$, $q_2 = 0.05$, $q_3 = 0.04$.

retrieved. Figure 6.7 reveals the shape of the five bubble boundaries in a particular assembly. The assembly is not symmetric about any axis and the areas of the bubbles are each different (corresponding to the different choices of $q_j$ values).

It is worth pointing out that we were unable to produce bubbles with areas much larger than those shown in Figures 6.4-6.7, or bubble assemblies with bubbles close to the channel walls. This is because computing the Schottky-Klein prime function in these cases becomes difficult: in these special cases, in the preimage domain $D_\zeta$, there will either be multiple close-to-touching boundary circles, or interior circles with large radii, or both. As mentioned in Chapter 4, computing the Schottky-Klein prime function becomes numerically challenging in these circumstances. With improved methods of computation of the Schottky-Klein prime function, obtaining such bubble assemblies should be a straightforward matter.

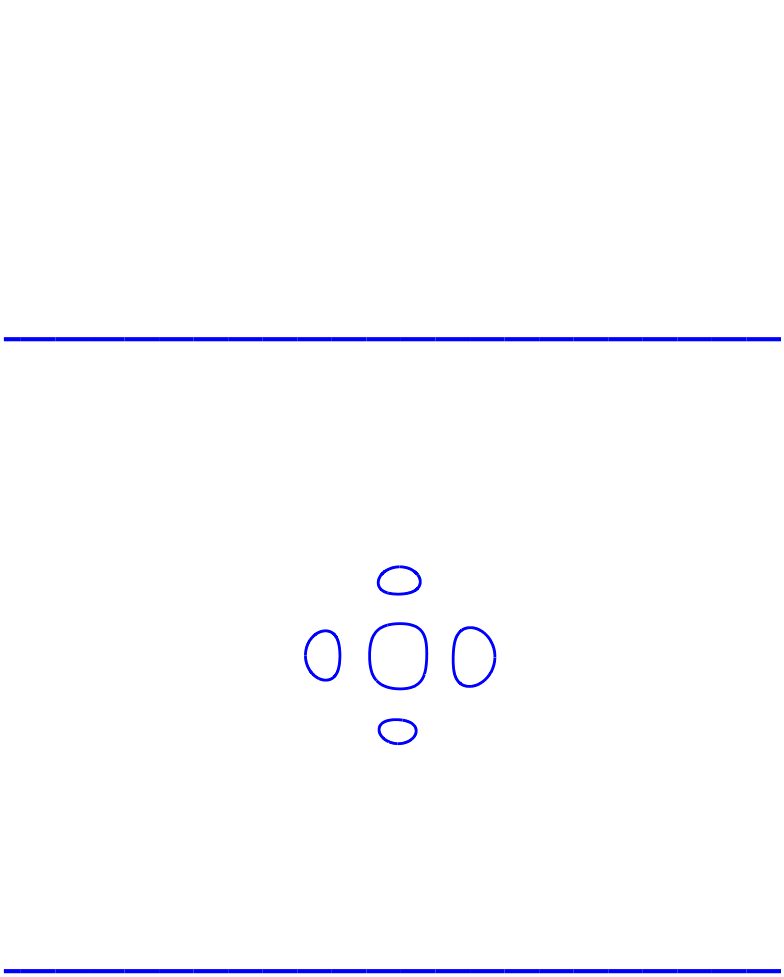

Figure 6.7: An example of five bubbles in a general asymmetric configuration. We chose the following conformal moduli of $D_\zeta$: $\delta_1 = 0$, $\delta_2 = 0.185$, $\delta_3 = -0.185$, $\delta_4 = 0.185\mathrm{i}$, $\delta_5 = -0.185\mathrm{i}$, $q_1 = 0.075$, $q_2 = 0.05$, $q_3 = 0.06$, $q_4 = 0.04$, $q_5 = 0.045$.

## 6.10 Summary

In this chapter, we have presented analytical solutions to the free boundary problem of determining the interface shapes of a finite number $M$ of bubbles, without surface tension, steadily translating along a Hele-Shaw channel. To do this, we found a concise formula for the conformal map in the form of an explicit indefinite integral from a bounded $M+1$ connected circular domain to the fluid region in the channel exterior to the $M$ bubbles, with the unit circle mapping to the channel walls. The integrand of our indefinite integral is neatly expressed in terms of products of Schottky-Klein prime functions and is known up to a finite set of accessory parameters to be found as part of the solution.

Our formula for the conformal map determining the bubble shapes is very general. An important characteristic of the derivation of this conformal map is that we made no *a priori* symmetry assumptions concerning the geometrical arrangement of the bubbles: indeed, all the geometrical information about the physical domain is encapsulated in the prescription of the preimage domain $D_\zeta$ over which each of the Schottky-Klein prime functions appearing in (6.48) is defined. In previous works on bubbles in Hele-Shaw channels, such symmetries had to be enforced in order to make progress; for example, in the works of Taylor & Saffman [111] and Vasconcelos [117]. Our solution scheme now readily incorporates the solutions found in these works and these solutions can be viewed as special cases of ours. It also generalises the work of Tanveer [109] on a single asymmetric bubble in a channel to more than one bubble, and the free space solutions of Crowdy [21] to the Hele-Shaw channel geometry. On the latter, it should be possible to retrieve the solutions of Crowdy [21] from those obtained using the methods of this chapter by taking the limit as the channel width becomes infinite, although we have not done this.

We have devised a constructive method for finding solutions to the free boundary problem based on ideas presented by Crowdy [13, 16, 20]. The free boundary problem determining the bubble shapes turns out to be equivalent to a special scalar Riemann-Hilbert problem solved in [20] and this Riemann-Hilbert problem, in turn, is related to the construction of generalised Schwarz-Christoffel formulae in [13, 16]. We made liberal use of conformal slit mappings as building block functions to incorporate the desired properties into the functions we were constructing. Consequently, just as in the other free boundary problems of this thesis, the Schottky-Klein prime function is the central mathematical object and the key to the success of our solution scheme.

We considered examples of various bubble assemblies, demonstrating that our solution scheme is capable of modelling any finite number of bubbles in a particular assembly. In each of the Figures 6.4-6.7 for the bubble assemblies we considered, the interaction between the bubbles is clearly visible from the shapes of their boundaries. We made choices of the conformal moduli defining $D_\zeta$ in order to find the finite set of accessory parameters in our conformal map determining the bubble shapes. Alternatively, we could have specified the areas and the centroids of each of the individual bubbles and solved for the conformal moduli of $D_\zeta$. However, this would have been a rather challenging undertaking, owing to the fact that the parameters $\{\gamma_1^{(j)}, \gamma_2^{(j)} \mid j = 1, ..., M\}$ (the set of preimages of the ends of the $M$ circular slits in the $\eta$-plane) would need to be calculated in each iterative step.

# Chapter 7

# Discussion

In this thesis, we have solved six different free boundary problems arising in fluid mechanics, in various multiply connected geometries. Each of the six free boundary problems we have solved has required individual and special mathematical treatments. The overriding challenge in each of these problems was to determine the shape of the multiple fluid interfaces defining the physical system: namely, in this thesis, hollow vortices and Hele-Shaw bubbles. The solutions we have presented are essentially special solutions of Laplace's equation in geometries with multiple boundaries. Constructing these solutions required employing the Schottky-Klein prime function in combination with elements of complex function theory, conformal mapping between multiply connected domains, and specialist techniques developed in recent years by Crowdy and collaborators. The solutions to each of the problems in this thesis also clearly illustrate the fundamental role of conformal slit mappings when solving free boundary problems with multiple boundaries. Further evidence of this is elucidated in a recent review by Crowdy [24] where a survey of usages of conformal slit mappings in applied mathematics is presented.

When analysing von Kármán streets of hollow vortices, we introduced the idea of capturing the periodicity of the street structure by restricting attention to a single period window containing two hollow vortex members of the street, and introducing a particular choice of branch cut in the preimage domain. We found a concise formula for the conformal mapping as an explicit indefinite integral describing the shapes of the free boundaries of the pair of hollow vortices in the period window; this formula captures both staggered and unstaggered street configurations. We then made an interesting qualitative comparison of our staggered street solutions with the solutions of Saffman & Schatzman [94] who studied von Kármán streets of finite-area vortex patches. By compiling analogues of Figures 2 and

3 in Saffman & Schatzman [94], we highlighted that approximately the same street aspect ratio in both inviscid vortex models is found to have a special significance; that is, there exists a critical aspect ratio determining whether or not we have unique solutions.

When studying the hollow vortex pair and a single row of hollow vortices in an infinite channel, we again incorporated the periodicity into our models by introducing appropriate branch cuts in the preimage circular domains. For both problems, we found concise formulae for the conformal mappings as explicit indefinite integrals determining the shapes of the hollow vortex boundaries. For the hollow vortex pair, we were able to make connections with the classical Michell [77] and Pocklington [85] solutions. With an eye on a recent experimental study by Stewart et al [106], where particle image velocimetry was used to study the evolution of vortex ring circulation in a channel, we note that our solutions could be used as a two-dimensional model of a vortex ring in a pipe. Since the study of Zannetti & Lasagna [128] only recently appeared after our work in Chapter 4 was complete, it is of great interest to undertake a direct numerical comparison of our solutions with theirs and to confirm that our two different methods of solution give identical free boundary shapes. The solutions pertaining to a single row of hollow vortices in a channel are generalisations of the Baker, Saffman & Sheffield [7] solutions to a confined environment, and also the singly periodic generalisations of the Michell [77] solution. We were able to verify that as the channel width becomes large, the hollow vortex shapes tend to the free space solutions due to [7]. We then compiled an intriguing analogue of Figure 3 in [7] for different channel widths and found that for a given hollow vortex area, two possible hollow vortex shapes can exist and which appear qualitatively very different in two particular limiting cases.

Saffman & Schatzman [95] used the vortex patch street solutions they found in [94] to devise an inviscid model of the vortex street wake behind a cylinder. It would be of great physical interest, and important for applications, to mimic this work of Saffman & Schatzman [95] for von Kármán hollow vortex streets and formulate an analogous model involving the solutions we constructed in Chapter 3. A natural extension of the work in both Chapter 3 and 4 would be to find analytical solutions for a von Kármán street of hollow vortices in an infinite channel. Analytical solutions of this particular free boundary problem will offer an inviscid wake structure model in a confined environment, and will be couched in a rich mathematical structure. This problem presents several mathematical challenges, not least because of the intrinsic periodicity structure and a typical period window being quadruply connected, but also because the analysis is expected to involve inverse conformal slit

mappings.

The new hollow vortex solutions of this thesis should facilitate studies into the effects of compressibility on the various hollow vortex structures we have considered. These studies are usually accomplished by performing low Mach number weakly compressible analyses using so-called Rayleigh-Jansen expansions; indeed, our new hollow vortex solutions are expected to be the leading order terms in these Rayleigh-Jansen expansions when such studies are undertaken. These analyses would be particularly valuable in the investigation of the compressibility effects in trailing von Kármán vortex streets in the wakes of aircraft. Ardalan, Meiron & Pullin [5] have examined the effects of compressibility on the structure of the single hollow vortex row by taking the Baker, Saffman & Sheffield [7] solution as the leading order term in their Rayleigh-Jansen expansion. Moore & Pullin [82] and Leppington [69] have also studied the effects of compressibility on types of vortex pairs.

Determining the stability properties of the new hollow vortex solutions presented in this thesis also remains as a task for the future. Recently, some stability analyses of certain classes of hollow vortex solution have appeared in the literature, and it should be possible to adapt the ideas in these works to our new hollow vortex solutions in order to make progress in this direction. Llewellyn Smith & Crowdy [72] have carried out a linear stability analysis of the equilibrium solutions they found for a single hollow vortex in both linear and non-linear straining flows. This paper also features a linear stability analysis, using ideas from Floquet theory, for the hollow vortex row due to Baker, Saffman & Sheffield [7]. In addition, Crowdy, Llewellyn Smith & Freilich [37] have examined the linear stability properties of their co-travelling hollow vortex pair solutions, whilst Luzzatto-Fegiz & Williamson [73] have presented a fascinating and detailed investigation using energy-based stability arguments into the possible equilibrium flows, and their associated stability properties, for von Kármán streets of finite-area vortex patches. Kida [66] and Meiron, Saffman & Schatzman [76] have also conducted investigations into the stability of von Kármán streets of vortex patches.

In Chapter 5, we derived a hybrid analytical-numerical scheme determining the shapes of the free boundaries of a pair of hollow vortices in the wake of a circular obstacle. The ‘new calculus’ proposed by Crowdy [14, 22] was a key ingredient in our work. We were able to trace out continuous families of hollow vortices and found that solutions exist for a finite range of area values. We saw that we were able to obtain qualitatively similar hollow

vortex shapes to Telib & Zannetti [112] for a particular value of the circulation. It is of pressing importance to make a closer comparison of our solutions with those of Telib & Zannetti [112], not least to understand the issue regarding existence of our solutions. The important question of stability of our solutions naturally arises. Elcrat, Fornberg & Miller [42] carried out a stability analysis of their solutions for a pair of vortex patches behind a circular cylinder. It would be interesting to make a similar line of enquiry with our hollow vortex solutions. This may shed light on why we were only able to determine classes of solution having a finite range of area values and without ever becoming close to the circular obstacle, unlike in the case of vortex patches (Elcrat et al [44]). It would also be interesting to desingularise other point vortex equilibria around a circular cylinder using our solution scheme of Chapter 5: there exists another equilibrium configuration when the two point vortices lie directly above and below the cylinder (documented in Protas [87] and Elcrat et al [44]), and Miller [78] has shown that there exists another class of point vortex equilibria consisting of two up-down symmetric point vortex pairs lying on either side of the cylinder.

In determining the shapes of any finite number of bubbles in a Hele-Shaw channel, we have generalised the work of Crowdy [21] who found the shapes of any finite number of bubbles in an unbounded Hele-Shaw cell. We have solved another version of a classical Laplacian growth free boundary problem and added to the vast body of prior work on bubbles in Hele-Shaw channels and cells. This particular free boundary problem turned out to be a special type of scalar Riemann-Hilbert problem. Consequently, we emulated the constructive methods of Crowdy [13, 20] and built the relevant formulae using conformal mappings to multiply connected slit domains. Our solution scheme is very general: all our formulae are applicable to any finite number of bubbles in a Hele-Shaw channel and the configuration of bubbles can be completely devoid of any symmetries. An interesting extension of our work would be to consider a doubly periodic array of asymmetric bubble assemblies. This, in turn, would generalise the solutions of Silva & Vasconcelos [104]. Another interesting line of enquiry would be to investigate the effects of surface tension on the bubble boundaries in the assemblies we have considered. This gives rise to so-called selection problems: for non-zero surface tensions, there is no longer a continuum of bubble speeds for which solutions can exist. It is also important to point out that obtaining exact analytical solutions for steady Hele-Shaw systems naturally paves the way to finding time-dependent solutions which are of great physical interest. An example of an extension to the steady theory is the very recent study by Mineev-Weinstein & Vasconcelos [81] who have been able to determine an exact solution for the time evolution of a bubble of arbi-

trary initial shape using elliptic functions. Our new solutions will be the starting point for any future endeavours looking into constructing time-dependent solutions for asymmetric configurations of multiple bubbles in a Hele-Shaw channel.

If more important problems in applied mathematics involving geometries in multiply connected domains are to be tackled successfully (which perhaps proved too computationally impenetrable in the past), having robust and volatile software at our disposal to rapidly and accurately compute the Schottky-Klein prime function given any multiply connected geometry, however complicated, would be highly desirable: for example, when resolving complicated parameter problems associated with the computation of Schwarz-Christoffel or polycircular arc mappings, or further improving the accuracy of certain solutions presented in this thesis. Computing the Schottky-Klein prime function becomes a challenging numerical undertaking if the circular domain over which it is defined becomes highly multiply connected, or when there are some boundary circles which are close-to-touching. Conformal mappings are usually susceptible to numerical problems such as 'crowding' if the preimage domain is of this type. One way to overcome the effects of crowding is to use a very high number of collocation points and compute with very high accuracy; however, this is computationally expensive. On this issue, it has been proposed recently by Crowdy, DeLillo & Marshall [35] that the use of so-called 'hybrid methods' can dramatically reduce computational time and can actually increase the overall accuracy of the solution being computed when boundary circles become closer and closer together. Further investigation into the (as yet unknown) special properties of these 'hybrid methods' would no doubt shed light on devising an efficient and accurate way to compute the Schottky-Klein prime function over a complicated circular domain. Work on developing an optimum method to compute the Schottky-Klein prime function is already in progress.

# Appendix A

# Von Kármán streets of point vortices

In this appendix, we outline some details of the analysis for constructing steady von Kármán point vortex streets. We will focus here on staggered streets, but the unstaggered case involves only minor changes in detail. Such details can also be found, for example, in the monographs of Acheson [2] and Saffman [93].

Consider a staggered von Kármán street of point vortices. Suppose the point vortices in the top row are all of circulation $\Gamma$, and the point vortices in the lower row are all of circulation $-\Gamma$. Suppose the configuration moves, without change of form, with speed $U$. The point vortices in both rows are assumed to be separated by a distance $L$. The complex potential in co-travelling frame of speed $U$ is

$$w(z) = -Uz - \frac{\mathrm{i}\Gamma}{2\pi}\log\sin\left(\frac{\pi(z-c)}{L}\right) + \frac{\mathrm{i}\Gamma}{2\pi}\log\sin\left(\frac{\pi(z+c)}{L}\right), \tag{A.1}$$

where $-L/2 < \mathrm{Re}[\pm c] < L/2$. The complex velocity is

$$\frac{dw}{dz} = -U - \frac{\mathrm{i}\Gamma}{2L}\cot\left(\frac{\pi(z-c)}{L}\right) + \frac{\mathrm{i}\Gamma}{2L}\cot\left(\frac{\pi(z+c)}{L}\right). \tag{A.2}$$

The condition that the vortex at $z = c$ is stationary (and, hence, by periodicity, all the other vortices in this row) is

$$-U + \frac{\mathrm{i}\Gamma}{2L}\cot\left(\frac{2\pi c}{L}\right) = 0. \tag{A.3}$$

By the symmetry, the same condition ensures that the point vortices in the lower row are also stationary. Thus

$$\tan\left(\frac{2\pi c}{L}\right) = \frac{\mathrm{i}\Gamma}{2LU}. \tag{A.4}$$

On use of the well-known identity

$$\tan(X+\mathrm{i}Y) = \frac{\tan X \operatorname{sech}^2 Y}{1+\tan^2 X \tanh^2 Y} + \frac{\mathrm{i}\tanh Y \sec^2 X}{1+\tan^2 X \tanh^2 Y}, \tag{A.5}$$

we see that we require

$$\frac{2\pi c}{L} = \frac{\pi}{2} + \mathrm{i}Y, \tag{A.6}$$

with

$$\coth Y = \frac{\Gamma}{2LU}. \tag{A.7}$$

Hence:

$$c = \frac{L}{4} + \frac{\mathrm{i}L}{2\pi}\coth^{-1}\left(\frac{\Gamma}{2LU}\right). \tag{A.8}$$

If $L = \Gamma = 1$, solutions for staggered point vortex streets exist provided

$$0 < U < \frac{1}{2}. \tag{A.9}$$

It can be shown in a similar fashion that solutions exist for unstaggered streets provided

$$U > \frac{1}{2}. \tag{A.10}$$

# Appendix B

# Re-derivation of the Baker, Saffman & Sheffield [7] solution

In this appendix, we will show that the conformal map we derived in Chapter 3 describing the shape of a typical hollow vortex in a row is equivalent to the solution presented by Baker, Saffman & Sheffield [7].

Recall from (3.36) that the conformal map from the interior of the unit $\zeta$-disc to a period cell containing a typical hollow vortex in a row is

$$z(\zeta) = \frac{L}{\pi}\left(\tan^{-1}(\zeta/a) - a^2\tan^{-1}(a\zeta)\right) \tag{B.1}$$

(ignoring the additive constant). This map takes the unit $\zeta$-circle to the boundary of the hollow vortex. Baker, Saffman & Sheffield [7] have given parametric equations $X(\lambda)$ and $Y(\lambda)$ for the same hollow vortex in terms of a perimeter parameter $\lambda$, taking values $0 \leq \lambda < 2\pi$. Motivated by this, put $\zeta = \mathrm{e}^{\mathrm{i}\phi}$, with $0 \leq \phi < 2\pi$, so that

$$z(\phi) = x(\phi) + \mathrm{i}y(\phi) = \frac{L}{\pi}\left(\tan^{-1}(\mathrm{e}^{\mathrm{i}\phi}/a) - a^2\tan^{-1}(a\mathrm{e}^{\mathrm{i}\phi})\right). \tag{B.2}$$

At some point on the hollow vortex boundary, $x(\phi)$ and $y(\phi)$ (for some value of $\phi$) must be equal to $X(\lambda)$ and $Y(\lambda)$ (for some value of $\lambda$). Thus, our aim is to show that $\phi$ is related to $\lambda$ at an arbitrary point on the boundary of the hollow vortex, i.e. when

$$x(\phi) + \mathrm{i}y(\phi) = X(\lambda) + \mathrm{i}Y(\lambda). \tag{B.3}$$

On use of the well-known identity

$$\tan^{-1}(Z) = \frac{\mathrm{i}}{2}\log\left(\frac{\mathrm{i}+Z}{\mathrm{i}-Z}\right), \tag{B.4}$$

(B.2) becomes

$$x(\phi)+\mathrm{i}y(\phi) = \frac{L}{\pi}\left(\frac{\mathrm{i}}{2}\log\left(\frac{a\mathrm{i}+\mathrm{e}^{\mathrm{i}\phi}}{a\mathrm{i}-\mathrm{e}^{\mathrm{i}\phi}}\right) - \frac{a^2\mathrm{i}}{2}\log\left(\frac{\mathrm{i}+a\mathrm{e}^{\mathrm{i}\phi}}{\mathrm{i}-a\mathrm{e}^{\mathrm{i}\phi}}\right)\right), \tag{B.5}$$

or

$$x(\phi)+\mathrm{i}y(\phi) = \frac{L}{\pi}\log\left(\left(\frac{a\mathrm{i}+\mathrm{e}^{\mathrm{i}\phi}}{a\mathrm{i}-\mathrm{e}^{\mathrm{i}\phi}}\right)^{\mathrm{i}/2}\left(\frac{\mathrm{i}-a\mathrm{e}^{\mathrm{i}\phi}}{\mathrm{i}+a\mathrm{e}^{\mathrm{i}\phi}}\right)^{a^2\mathrm{i}/2}\right). \tag{B.6}$$

Let

$$\frac{a\mathrm{i}+\mathrm{e}^{\mathrm{i}\phi}}{a\mathrm{i}-\mathrm{e}^{\mathrm{i}\phi}} = R_1\mathrm{e}^{\mathrm{i}\Theta_1}, \quad \frac{\mathrm{i}-a\mathrm{e}^{\mathrm{i}\phi}}{\mathrm{i}+a\mathrm{e}^{\mathrm{i}\phi}} = R_2\mathrm{e}^{\mathrm{i}\Theta_2}, \tag{B.7}$$

where $R_1, R_2, \Theta_1, \Theta_2 \in \mathbb{R}$ can be found. Then

$$x(\phi)+\mathrm{i}y(\phi) = \frac{L}{\pi}\log\left(\exp\left(\frac{\mathrm{i}}{2}\log(R_1\mathrm{e}^{\mathrm{i}\Theta_1}) + \frac{a^2\mathrm{i}}{2}\log(R_2\mathrm{e}^{\mathrm{i}\Theta_2})\right)\right), \tag{B.8}$$

i.e.

$$x(\phi)+\mathrm{i}y(\phi) = \frac{L}{2\pi}\left(\mathrm{i}(\log R_1 + a^2\log R_2) - (\Theta_1 + a^2\Theta_2)\right). \tag{B.9}$$

Thus, upon equating real and imaginary parts,

$$x(\phi) = -\frac{L}{2\pi}(\Theta_1 + a^2\Theta_2), \quad y(\phi) = \frac{L}{2\pi}\left(\log R_1 + a^2\log R_2\right), \tag{B.10}$$

a first correspondence between (B.2) and the parametric equations of Baker, Saffman & Sheffield [7] is made. Recall from (3.30) and (3.32) that our complex velocity function is

$$\frac{dw}{dz} = \frac{\mathrm{i}U\zeta}{a}. \tag{B.11}$$

Baker, Saffman & Sheffield [7] define the quantity

$$R = \frac{U_\infty}{q_0}. \tag{B.12}$$

In our notation, $U_\infty = U$, and

$$q_0 = \left|\frac{dw}{dz}\right|_{|\zeta|=1} = \frac{U}{a}. \tag{B.13}$$

Hence

$$R = a. \tag{B.14}$$

After some algebra, it can be shown that

$$R_1 = \frac{1 + 2R\sin\phi + R^2}{((1+R^2)^2 - 4R^2\sin^2\phi)^{1/2}} = \frac{1}{R_2}, \quad \Theta_1 = \tan^{-1}\left(\frac{2R\cos\phi}{1-R^2}\right) = \Theta_2, \tag{B.15}$$

and so (B.10) becomes

$$\begin{aligned} x(\phi) &= -\frac{L}{2\pi}(1+R^2)\tan^{-1}\left(\frac{2R\cos\phi}{1-R^2}\right), \\ y(\phi) &= \frac{L}{2\pi}(1-R^2)\log\left(\frac{1+2R\sin\phi+R^2}{((1+R^2)^2-4R^2\sin^2\phi)^{1/2}}\right). \end{aligned} \tag{B.16}$$

The parametric equations of Baker, Saffman & Sheffield [7] are

$$\begin{aligned} X(\lambda) &= \frac{L}{2\pi}(1+R^2)\sin^{-1}\left(\frac{2R\sin\lambda}{1+R^2}\right), \\ Y(\lambda) &= \frac{L}{2\pi}(1-R^2)\sinh^{-1}\left(\frac{2R\cos\lambda}{1-R^2}\right). \end{aligned} \tag{B.17}$$

For (B.3) to hold true, it is clear that we require

$$-\tan^{-1}\left(\frac{2R\cos\phi}{1-R^2}\right) = \sin^{-1}\left(\frac{2R\sin\lambda}{1+R^2}\right) \tag{B.18}$$

and

$$\log\left(\frac{1+2R\sin\phi+R^2}{((1+R^2)^2-4R^2\sin^2\phi)^{1/2}}\right) = \sinh^{-1}\left(\frac{2R\cos\lambda}{1-R^2}\right). \tag{B.19}$$

On use of the well-known identities

$$\sin(\tan^{-1}Z) = \frac{Z}{(1+Z^2)^{1/2}}, \quad \sinh(\log Z) = \frac{1}{2}\left(Z - \frac{1}{Z}\right), \tag{B.20}$$

and after some algebra, we find that

$$\cos\lambda = \frac{(1-R^2)\sin\phi}{((1+R^2)^2-4R^2\sin^2\phi)^{1/2}}, \quad \sin\lambda = -\frac{(1+R^2)\cos\phi}{((1+R^2)^2-4R^2\sin^2\phi)^{1/2}}. \tag{B.21}$$

Thus, we indeed have a consistent correspondence between $\phi$ and $\lambda$.

# Appendix C

# Co-travelling pair of point vortices in an infinite channel

In this appendix, we outline the analysis for a pair of point vortices steadily translating along an infinite channel with vertically-aligned walls.

The complex potential for two point vortices with circulations $\pm\Gamma$ inside the unit circle in a parametric $\zeta$-plane is

$$W(\zeta) = -\frac{\mathrm{i}\Gamma}{2\pi}\log\left(\frac{\zeta-\gamma_1}{\zeta-1/\overline{\gamma}_1}\right) + \frac{\mathrm{i}\Gamma}{2\pi}\log\left(\frac{\zeta-\gamma_2}{\zeta-1/\overline{\gamma_2}}\right). \tag{C.1}$$

The conformal mapping from an infinite vertical channel of unit width in a $z$-plane to the interior of the unit $\zeta$-disc is given by

$$\zeta(z) = \tanh\left(\frac{\pi z}{2\mathrm{i}}\right). \tag{C.2}$$

Suppose the point vortices are located at

$$x = \pm c. \tag{C.3}$$

Their corresponding images in the $\zeta$-plane are

$$\zeta = \pm\tanh(\pi c/2\mathrm{i}). \tag{C.4}$$

It follows that the complex potential in the $z$-plane is

$$w(z) = -\frac{\mathrm{i}\Gamma}{2\pi}\log\left(\frac{\tanh(\pi z/2\mathrm{i})+\tanh(\pi c/2\mathrm{i})}{\tanh(\pi z/2\mathrm{i})-\coth(\pi c/2\mathrm{i})}\right)+\frac{\mathrm{i}\Gamma}{2\pi}\log\left(\frac{\tanh(\pi z/2\mathrm{i})-\tanh(\pi c/2\mathrm{i})}{\tanh(\pi z/2\mathrm{i})+\coth(\pi c/2\mathrm{i})}\right), \tag{C.5}$$

or, after some algebra:

$$w(z) = -\frac{\mathrm{i}\Gamma}{2\pi}\log\left(\frac{\tanh(\mathrm{i}\pi z)+\tanh(\mathrm{i}\pi c)}{\tanh(\mathrm{i}\pi z)-\tanh(\mathrm{i}\pi c)}\right). \tag{C.6}$$

By some further algebra, it can be verified that the vortex pair travels vertically down the channel with velocity

$$\frac{dw}{dz} = U - \mathrm{i}V = -\frac{\mathrm{i}\Gamma}{2}\cot(2\pi c) \tag{C.7}$$

(with $U = 0$) so that

$$\left|\frac{dw}{dz}\right| = \frac{\Gamma}{2}\cot(2\pi c). \tag{C.8}$$

When $c < 1/4$, the stagnation points are complex conjugate pairs lying on the channel centreline. As $c \to 1/4$, the stagnation points move off towards infinity in opposite directions. The point vortex pair is stationary when $c = 1/4$. When $c > 1/4$, these stagnation points move onto one of the channel walls, still as a complex conjugate pair. There is an accompanying pair of stagnation points, with the same imaginary parts, on the other channel wall.

# Appendix D

# Row of hollow vortices in an infinite channel with centroids not on the channel centreline

In this appendix, we briefly outline how our approach presented in Chapter 4 can be generalised to the case where the centroids of the hollow vortices in the row configuration are moved off the channel centreline, with $y$-coordinate $y_0 \neq 0$. This row of hollow vortices is expected to translate steadily in the $x$-direction along the channel with some constant speed $U$ to be determined *a posteriori*.

It is expected that a formula for $U$ should be able to be derived using information about the flux of the fluid through the period cell, but we have so far been unable to do this. We were also not contented by several aspects of our numerical work at the time of writing. Resolving these issues remains a matter for the future.

## D.1 Function $W(\zeta)$

To perform the analysis, we move to a co-travelling frame of reference with the hollow vortex row. A typical period window of this row does not have any up-down symmetry about the channel centreline; consequently, in $D_\zeta$, we expect $q_1 \neq q_2$. See Figure D.1. As before, we expect two stagnation points to lie on the edges of the period window with the same $y$-coordinate.

We propose the following function for the complex potential, in a co-travelling frame with

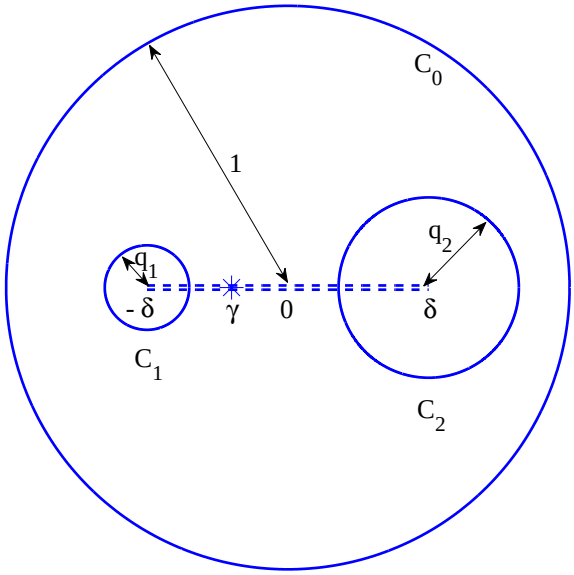


Figure D.1: Schematic showing the preimage triply connected bounded circular domain $D_\zeta$ in the $\zeta$-plane, corresponding to solutions for a hollow vortex row with centroids not on the channel centreline.

the hollow vortices:

$$W(\zeta) = \Gamma_1 v_1(\zeta) + \Gamma_2 v_2(\zeta). \tag{D.1}$$

Here, $\Gamma = \Gamma_1 + \Gamma_2$ is the total circulation in the period cell. Since the period cell is not up-down symmetric, we expect an unequal contribution to the total circulation in the period cell along the two channel walls. It follows from the 'a-cycle' properties of the $v_j(\zeta)$ functions (2.7) that (D.1) satisfies (4.38). Being a sum of $v_j(\zeta)$ functions, (D.1) also has constant imaginary part on all the boundary circles of $D_\zeta$, as required.

## D.2 Function $dw/dz$

We claim that the complex velocity function is again

$$\frac{dw}{dz} = Q_0 \mathcal{S}(\zeta; R) \tag{D.2}$$

with function $\mathcal{S}(\zeta; R)$ as in (4.49). The preimage of the two stagnation points $\zeta = \gamma \neq 0$ will lie on the branch cut joining $\delta_1$ and $\delta_2$, where $\gamma \in \mathbb{R}$ will need to be found as part of

the solution. The value of $R$ will now be

$$R = \frac{\omega(\gamma, -1)}{\omega(\gamma, 1)}, \tag{D.3}$$

thus ensuring that

$$\frac{dw}{dz}(\gamma) = 0. \tag{D.4}$$

## D.3 Conformal map $z(\zeta)$

The conformal map is given through the integral

$$z(\zeta) = \frac{1}{Q_0} \int_{\zeta_0}^{\zeta} \frac{\Gamma_1 v_1'(\zeta') + (\Gamma - \Gamma_1)\, v_2'(\zeta')}{S(\zeta'; R)} d\zeta'. \tag{D.5}$$

Here, $\zeta_0 \in \mathbb{C}$ is an arbitrary point in the interior of $D_\zeta$.

## D.4 Proposed solution scheme

As in Chapter 4, we can fix

$$L = \Gamma = 1. \tag{D.6}$$

The centres of $C_1$ and $C_2$ can again be taken to be $\delta_1 = -\delta_2 = \delta \in \mathbb{R}$ (see Figure D.1). For convenience, introduce a continuation parameter $0 < \varepsilon < 1$ such that

$$\Gamma_1 = \frac{1}{2}(1 + \varepsilon). \tag{D.7}$$

Hence

$$\Gamma_2 = 1 - \Gamma_1 = \frac{1}{2}(1 - \varepsilon). \tag{D.8}$$

There are then the following four real parameters to determine:

$$\delta, \quad q_1, \quad q_2, \quad \gamma. \tag{D.9}$$

These parameters can be found by solving the following four real equations. We expect to be able to specify the aspect ratio of the period cell

$$\lambda = \left( \int_{-\delta+q_1}^{\delta-q_2} |z_\zeta(\zeta') d\zeta'| \right) \Big/ \left( \oint_{C_1} |z_\zeta(\zeta') d\zeta'| \right), \tag{D.10}$$

and the imaginary part $\mathcal{C}$ of the centroid of the hollow vortex

$$\mathrm{Im}\left[\oint_{C_0} z(\zeta')|z_\zeta(\zeta')d\zeta'|\right] \Big/ \left(\oint_{C_0} |z_\zeta(\zeta')d\zeta'|\right) = \mathcal{C}. \tag{D.11}$$

We require the length of the top and bottom channel walls of the period cell to be equal:

$$\oint_{C_1} |z_\zeta(\zeta')d\zeta'| = \oint_{C_2} |z_\zeta(\zeta')d\zeta'|. \tag{D.12}$$

This condition (D.12) implicitly enforces that the conformal map $z(\zeta)$ be single-valued everywhere in $D_\zeta$. Finally, the derivative of $W(\zeta)$ with respect to $\zeta$ should have a simple zero at $\zeta = \gamma$. It is sufficient to enforce

$$\mathrm{Im}\left[\frac{dW}{d\zeta}(\gamma)\right] = 0, \tag{D.13}$$

since the choice of $D_\zeta$ guarantees that

$$\mathrm{Re}\left[\frac{dW}{d\zeta}(\gamma)\right] = 0. \tag{D.14}$$

# Appendix E

# Initial estimates of the solutions in Chapter 5

In this appendix, we briefly outline the procedure we employed to generate initial estimates for the values of the conformal mapping parameters in Chapter 5. Our procedure is centred around knowledge of the Föppl point vortex system.

## E.1 Föppl point vortex equilibria

In a $z = (x + \mathrm{i}y)$-plane, let two point vortices of strengths $-\Gamma$ and $\Gamma$ be placed behind $|z| = 1$ in a uniform stream $U$ at positions $z = z_0 = x_0 + \mathrm{i}y_0$ and $z = \overline{z_0}$ (where $|z_0| > 1$), respectively. The complex potential for this Föppl point vortex system is

$$w(z) = U\left(z + \frac{1}{z}\right) + \frac{\mathrm{i}\Gamma}{2\pi}\log\left(\frac{(z - z_0)(z - 1/z_0)}{(z - \overline{z_0})(z - 1/\overline{z_0})}\right). \tag{E.1}$$

For fixed values of $\Gamma$ and $U$, it can be shown that the two point vortices are in equilibrium provided $x_0$ and $y_0$ satisfy the two non-linear equations

$$x_0^2 + y_0^2 - 1 = 2ry_0, \tag{E.2}$$

and

$$\Gamma = 4\pi U y_0\left(1 - \frac{1}{(x_0^2 + y_0^2)^2}\right). \tag{E.3}$$

There are five stagnation points in the system, and these are the solutions to

$$\frac{dw}{dz} = 0. \tag{E.4}$$

## E.2 Möbius mappings

We will construct a Möbius map $\zeta(z)$ from the exterior of two small circles of radius $\varepsilon$ around $z_0$ and $\overline{z_0}$ in the $z$-plane to the interior of a concentric annulus $\rho < |\zeta| < 1$ in a $\zeta$-plane (where $\rho$ will be determined). The image of $|z| = 1$ in the $\zeta$-plane is easily determined once the map $z(\zeta)$ is known; this provides the initial estimates for the centre $\delta$ and radius $q$ of circle $C_2$ (recall Figure 5.2).

Consider the following sequence of conformal mappings taking the exterior of $|z - z_0| = \varepsilon$ and $|z - \overline{z_0}| = \varepsilon$ to the interior of an eccentric annulus $\hat{D}_\zeta$ with inner circle having centre $\delta'$ and radius $q'$ (say):

$$\zeta_1(z) = \frac{z - z_0}{\varepsilon}, \quad \zeta_2(\zeta_1) = \frac{1}{\zeta_1}, \quad \zeta_3(\zeta_2) = -\mathrm{i}\zeta_2. \tag{E.5}$$

Next, consider mapping this eccentric annulus $\hat{D}_\zeta$ to a concentric annulus $\rho < |\tilde{\zeta}| < 1$ which we will label $\tilde{D}_\zeta$:

$$\tilde{\zeta}(\zeta_3) = \frac{\zeta_3 - \alpha}{|\alpha|\,(\zeta_3 - 1/\alpha)} \tag{E.6}$$

This map (E.6) is an automorphism of the unit disc which we introduced in Chapter 2 (recall (2.45)). Recall also from Chapter 2 the values (2.46):

$$\rho = \frac{1 - \delta'^2 + q'^2 - ((1 - \delta'^2 + q'^2)^2 - 4q'^2)^{1/2}}{2q'}, \quad \alpha = \left(\frac{\rho - q'}{\rho(1 - q'\rho)}\right)^{1/2}. \tag{E.7}$$

Note that the image of $|z| = 1$ under $(\tilde{\zeta} \circ \zeta_3 \circ \zeta_2 \circ \zeta_1)(z)$ is a circle lying in the interior of the concentric annulus $\tilde{D}_\zeta$ having centre $\delta = |\delta'|\mathrm{e}^{\mathrm{i}(2\pi - \phi)}$ (with $0 < \phi < \pi/2$) and radius $q$ (say). Explicit formulae can be written down determining the values of $\delta$ and $q$ (see Marshall [74]). A final rotation of $\tilde{D}_\zeta$ through

$$\zeta(\tilde{\zeta}) = \mathrm{e}^{\mathrm{i}\phi}\tilde{\zeta} \tag{E.8}$$

yields another concentric annulus $\rho < |\zeta| < 1$ which we label $D_\zeta$. Now the image of $|z| = 1$ under $(\zeta \circ \tilde{\zeta} \circ \zeta_3 \circ \zeta_2 \circ \zeta_1)(z)$ is a circle lying in the interior of the concentric annulus $D_\zeta$ having centre $\delta = |\delta'|$ and radius $q$.

Written out in full, the map from the exterior of $|z - z_0| = \varepsilon$ and $|z - \overline{z_0}| = \varepsilon$ to the interior

of $D_\zeta$ is

$$\zeta(z) = \frac{\mathrm{e}^{\mathrm{i}\phi}\left(\mathrm{i}\varepsilon - \alpha(z_0 - z)\right)}{|\alpha|\left(\mathrm{i}\varepsilon - (z_0 - z)/\alpha\right)}. \tag{E.9}$$

The inverse map $z(\zeta)$ taking the interior of $D_\zeta$ to the exterior of $|z-z_0| = \varepsilon$ and $|z-\overline{z_0}| = \varepsilon$ can now be written down:

$$z(\zeta) = \frac{\mathrm{e}^{\mathrm{i}\phi}\left(\mathrm{i}\varepsilon - \alpha z_0\right) + |\alpha|\zeta\left(z_0/\alpha - \mathrm{i}\varepsilon\right)}{|\alpha|\zeta/\alpha - \alpha\mathrm{e}^{\mathrm{i}\phi}}. \tag{E.10}$$

All the conformal mapping parameters that we require to begin the Newton iterations of Chapter 5 can now be deduced. We can initially take all the coefficients in the Fourier-Laurent series expansion of $z(\zeta)$ in (5.34) to be zero (say). The initial estimate for the value of the fluid speed $c$ on the hollow vortex boundaries is given by

$$c = \frac{\Gamma}{2\pi\varepsilon}. \tag{E.11}$$

# List of Figures

# References


[1] M. J. Ablowitz & A. S. Fokas. *Complex variables: introduction and applications*. Cambridge University Press, Cambridge, 2nd edition, (2003).

[2] D. J. Acheson. *Elementary fluid dynamics*Oxford University Press, Oxford, (1990).

[3] N. I. Akhiezer. *Elements of the theory of elliptic functions*. American Mathematical Society, Providence, (1990).

[4] G. Alobaidi & R. Mallier. Vortex streets on a sphere. *J. Appl. Math.*, **2011**:1-9, (2011).

[5] K. Ardalan, D. I. Meiron & D. I. Pullin. Steady compressible vortex flows: the hollow-core vortex array. *J. Fluid Mech.*, **301**:1-17, (1995).

[6] H. F. Baker. *Abelian functions: Abel's theorem and the allied theory of theta functions*. Cambridge University Press, Cambridge, (1897).

[7] G. R. Baker, P. G. Saffman & J. S. Sheffield. Structure of a linear array of hollow vortices of finite cross-section. *J. Fluid Mech.*, **74**:469-476, (1976).

[8] G. K. Batchelor. *An introduction to fluid dynamics* Cambridge University Press, Cambridge, (1967).

[9] G. Chamoun, E. Kanso & P. K. Newton. Von Kármán vortex streets on the sphere. *Phys. Fluids*, **21**:116603, (2009).

[10] K. P. Chopra & L. F. Hubert. Kármán vortex streets in Earth's atmosphere. *Nature*, **203**:1341-1343, (1964).

[11] K. P. Chopra & L. F. Hubert. Mesoscale eddies in wake of islands. *J. Atmos. Sci.*, **22**:652-657, (1965).

[12] D. G. Crowdy. Quadrature domains and fluid dynamics. In *Quadrature domains and their applications*, Vol. 156 of *Oper. Theory Adv. Appl.* Birkhäuser, Basel, (2005).

[13] D. G. Crowdy. The Schwarz-Christoffel mapping to bounded multiply connected polygonal domains. *Proc. Roy. Soc. A*, **461**:2653-2678, (2005).

[14] D. G. Crowdy. Analytical solutions for uniform potential flow past multiple cylinders. *Eur. J. Mech. B Fluids*, **25**:459-470, (2006).

[15] D. G. Crowdy. Calculating the lift on a finite stack of cylindrical aerofoils. *Proc. Roy. Soc. A*, **462**:1387-1407, (2006).

[16] D. G. Crowdy. Schwarz-Christoffel mappings to unbounded multiply connected polygonal regions. *Math. Proc. Cambridge Philos. Soc.*, **142**:319-339, (2007).

[17] D. G. Crowdy. Geometric function theory: a modern view of a classical subject. *Nonlinearity*, **21**:205-219, (2008).

[18] D. G. Crowdy. The Schwarz problem in multiply connected domains and the Schottky-Klein prime function. *Complex Var. Elliptic Equ.*, **53**:221-236, (2008).

[19] D. G. Crowdy. An assembly of steadily translating bubbles in a Hele-Shaw channel. *Nonlinearity*, **22**:51-65, (2009).

[20] D. G. Crowdy. Explicit solution of a class of Riemann-Hilbert problems. *Ann. Univ. Paedagog. Crac. Stud. Math.*, **8**:5-18, (2009).

[21] D. G. Crowdy. Multiple steady bubbles in a Hele-Shaw cell. *Proc. Roy. Soc. A*, **465**:421-435, (2009).

[22] D. G. Crowdy. A new calculus for two-dimensional vortex dynamics. *Theor. Comput. Fluid Dyn.*, **24**:9-24, (2010).

[23] D. G. Crowdy. The Schottky-Klein prime function on the Schottky double of planar domains. *Comput. Methods Funct. Theory*, **10**:501-517, (2010).

[24] D. G. Crowdy. Conformal slit maps in applied mathematics. *ANZIAM Journal*, **53**:171-189, (2012).

[25] D. G. Crowdy & C. C. Green. Analytical solutions for von Kármán streets of hollow vortices. *Phys. Fluids*, **23**:126602, (2011).

[26] D. G. Crowdy & H. Kang. Squeeze flow of multiply connected fluid domains in a Hele-Shaw cell. *J. Nonlinear Sci.*, **11**:279-304, (2001).

[27] D. G. Crowdy & J. S. Marshall. Constructing multiply connected quadrature domains. *SIAM J. Appl. Math.*, **64**:1334-1359, (2004).

[28] D. G. Crowdy & J. S. Marshall. Analytical formulae for the Kirchhoff-Routh path function in multiply connected domains. *Proc. Roy. Soc. A*, **461**:2477-2501, (2005).

[29] D. G. Crowdy & J. S. Marshall. Conformal mappings between canonical multiply connected domains. *Comput. Methods Funct. Theory*, **6**:59-76, (2006).

[30] D. G. Crowdy & J. S. Marshall. The motion of a point vortex through gaps in walls. *J. Fluid Mech.*, **551**:31-48, (2006).

[31] D. G. Crowdy & J. S. Marshall. Computing the Schottky-Klein prime function on the Schottky double of planar domains. *Comput. Methods Funct. Theory*, **7**:293-308, (2007).

[32] D. G. Crowdy & J. S. Marshall. Green's functions for Laplace's equation in multiply connected domains. *IMA. J. Appl. Math.*, **72**:278-301, (2007).

[33] D. G. Crowdy & J. S. Marshall. Multiply connected quadrature domains and the Bergman kernel function. *Complex Anal. Oper. Theory*, **3**:379-397, (2009).

[34] D. G. Crowdy & S. Tanveer. A theory of exact solutions for annular viscous blobs. *J. Nonlinear Sci.*, **8**:375-400, (1998).

[35] D. G. Crowdy, T. K. DeLillo & J. S. Marshall. Computing electrostatic fields exterior to close-to-touching discs (in preparation).

[36] D. G. Crowdy, A. S. Fokas & C. C. Green. Conformal mappings to multiply connected polycircular arc domains. *Comput. Methods Funct. Theory*, **11**:685-706, (2011).

[37] D. G. Crowdy, S. G. Llewellyn Smith & D. V. Freilich. Translating hollow vortex pairs. *Eur. J. Mech. B Fluids*, **37**:180-186, (2013).

[38] P. J. Davis. *The Schwarz function and its applications*. The Mathematical Association of America, Washington DC, (1974). The Carus Mathematical Monographs, No. 17.

[39] T. K. DeLillo & E. H. Kropf. Slit maps and Schwarz-Christoffel maps for multiply connected domains. *Electron. Trans. Numer. Anal.*, **36**:195-223, (2010).

[40] T. K. DeLillo, T. A. Driscoll, A. R. Elcrat & J. A. Pfaltzgraff. Radial and circular slit maps of unbounded multiply connected circle domains. *Proc. Roy. Soc. A*, **464**:1719-1737, (2008).

[41] A. R. Elcrat & L. Zannetti. Models for inviscid wakes past a normal plate. *J. Fluid Mech.*, **708**:377-396, (2012).

[42] A. R. Elcrat, B. Fornberg & K. G. Miller. Stability of vortices in equilibrium with a cylinder. *J. Fluid Mech.*, **544**:53-68, (2005).

[43] A. R. Elcrat, C. Hu & K. G. Miller. Equilibrium configurations of point vortices for channel flows past interior obstacles. *Eur. J. Mech. B Fluids*, **16**:277-292, (1997).

[44] A. R. Elcrat, B. Fornberg, M. Horn & K. G. Miller. Some steady vortex flows past a circular cylinder. *J. Fluid Mech.*, **409**:13-27, (2000).

[45] J. D. Fay. *Theta functions on Riemann surfaces*. Springer, New York, (2008).

[46] L. Föppl. Wirbelbewegung hinter einem kreiscylinder. *Sitzb. Bayer. Akad. Wiss.*, **1**:1, (1913).

[47] L. R. Ford. *Automorphic functions*. American Mathematical Society, Providence, (1951).

[48] A. Friedman. Free boundary problems in science and technology. *Notices of the AMS*, **47**:854-861, (2000).

[49] F. D. Gakhov. *Boundary value problems*. Dover, New York, (1990).

[50] G. Giannakidis. Prandtl-Batchelor flow in a channel. *Phys. Fluids*, **5**:863, (1993).

[51] H. Glauert. The characteristics of a Kármán vortex street in a channel of finite breadth. *Proc. Roy. Soc. A*, **120**:34-46, (1928).

[52] G. M. Goluzin. *Geometric theory of functions of a complex variable*. American Mathematical Society, Providence, (1969).

[53] V. N. Govorukhin, A. B. Morgulis & V. A. Vladimirov. Planar inviscid flows in a channel of finite length: washout, trapping and self-oscillations of vorticity. *J. Fluid Mech.*, **659**:420-472, (2010).

[54] C. C. Green & J. S. Marshall. Green's function for the Laplace-Beltrami operator on a toroidal surface. *Proc. Roy. Soc. A*, **469**:20120479, (2013).

[55] L. Greengard. Potential flow in channels. *SIAM J. Sci. Statist. Comput.*, **11**:603-620, (1990).

[56] B. Gustafsson & H. S. Shapiro. What is a quadrature domain? In *Quadrature domains and their applications*, Vol. 156 of *Oper. Theory Adv. Appl.* Birkhäuser, Basel, (2005).

[57] D. Hally. Stability of streets of vortices on surfaces of revolution with a reflection symmetry. *J. Math. Phys.*, **21**:211-217, (1980).

[58] R. Heinze, S. Raasch & D. Etling. The structure of Kármán vortex streets in the atmospheric boundary layer derived from large eddy simulation. *Meteorologische Zeitschrift*, **21**:221-237, (2012).

[59] D. A. Hejhal. *Theta functions, kernel functions and Abelian integrals*. American Mathematical Society, Providence, (1972). Memoirs of the American Mathematical Society, Vol. 129.

[60] W. M. Hicks. On the steady motion and small vibrations of a hollow vortex. *Phil. Trans. Roy. Soc. London*, **175**:161-195, (1884).

[61] E. R. Johnson & R. N. McDonald. The motion of a vortex near two circular cylinders. *Proc. Roy. Soc. A*, **460**:939-954, (2004).

[62] E. R. Johnson & R. N. McDonald. Vortices near barriers with multiple gaps. *J. Fluid Mech.*, **531**:335-358, (2005).

[63] E. R. Johnson & R. N. McDonald. Steady vortical flow around a finite plate. *Quart. J. Mech. Appl. Math.*, **60**:65-72, (2007).

[64] E. R. Johnson & R. N. McDonald. Necking in coating flow over periodic substrates. *J. Eng. Math.*, **65**:171-178, (2009).

[65] J. R. Kamm. Shape and stability of two-dimensional uniform vorticity regions. *PhD Thesis, California Institute of Technology*, (1987).

[66] S. Kida. Stabilizing effects of finite core on Kármán vortex street. *J. Fluid Mech.*, **122**:487-504, (1982).

[67] F. Klein. Zur theorie der Abel'schen functionen. *Math. Ann.*, **36**:1-83, (1890).

[68] M. Lagally. Die reibungslose strömung im aussengebiet zweier kreise. *Z. Angew. Math. Mech.*, **9**:299-305, (1929).

[69] F. G. Leppington. The field due to a pair of line vortices in a compressible fluid. *J. Fluid Mech.*, **559**:45-55, (2006).

[70] X. Li, P. Clemente-Colón, W. G. Pichel & P. W. Vachon. Atmospheric vortex streets on a RADARSAT SAR image. *Geophys. Res. Lett.*, **27**:1655-1658, (2000).

[71] J. C. Liao, D. N. Beal, G. V. Lauder & M. S. Triantafyllou. The Kármán gait: novel body kinematics of rainbow trout swimming in a vortex street. *J. Exp. Biol.*, **206**:1059-1073, (2003).

[72] S. G. Llewellyn Smith & D. G. Crowdy. Structure and stability of hollow vortex equilibria. *J. Fluid Mech.*, **691**:178-200, (2012).

[73] P. Luzzatto-Fegiz & C. H. K. Williamson. Stability of conservative flows and new steady-fluid solutions from bifurcation diagrams exploiting a variational argument. *Phys. Rev. Lett.*, **104**:044504, (2010).

[74] J. S. Marshall. Function theory in multiply connected domains and applications to fluid dynamics. *PhD Thesis, Imperial College London*, (2005).

[75] J. S. Marshall. Steady uniform vortex patches around an assembly of walls or flat plates. *Quart. J. Mech. Appl. Math.*, **65**:27-60, (2012).

[76] D. I. Meiron, P. G. Saffman & J. C. Schatzman. The linear two-dimensional stability of inviscid vortex streets of finite-cored vortices. *J. Fluid Mech.*, **147**:187-212, (1984).

[77] J. H. Michell. On the theory of free stream lines. *Phil. Trans. Roy. Soc. London*, **181**:389-431, (1890).

[78] K. G. Miller. Stationary corner vortex configurations. *Z. Angew. Math. Phys.*, **47**:39-56, (1996).

[79] L. M. Milne-Thomson. *Theoretical hydrodynamics*. Macmillan, New York, (1968).

[80] G. W. Milton & S. K. Serkov. Neutral coated inclusions in conductivity and anti-plane elasticity. *Proc. Roy. Soc. A*, **457**:1973-1997, (2001).

[81] M. Mineev-Weinstein & G. L. Vasconcelos. Selection of the Taylor-Saffman bubble without surface tension (in preparation).

[82] D. W. Moore & D. I. Pullin. The compressible vortex pair. *J. Fluid Mech.*, **185**:171-204, (1987).

[83] D. Mumford, C. Series & D. Wright. *Indra's pearls: the vision of Felix Klein*. Cambridge University Press, Cambridge, (2002).

[84] Z. Nehari. *Conformal mapping*. Dover, New York, (1975).

[85] H. C. Pocklington. The configuration of a pair of equal and opposite hollow straight vortices of finite cross-section moving steadily through fluid. *Phil. Trans. Roy. Soc. London*, **8**:178-187, (1894).

[86] B. Protas. Linear feedback stabilization of laminar vortex shedding based on a point vortex model. *Phys. Fluids*, **16**:4473, (2004).

[87] B. Protas. Higher-order Föppl models of steady wake flows. *Phys. Fluids*, **18**:117109, (2006).

[88] B. Protas. Center manifold analysis of a point vortex model of vortex shedding with control. *Physica D*, **228**:179-187, (2007).

[89] B. Protas. Vortex dynamics models in flow control problems. *Nonlinearity*, **21**:203-250, (2008).

[90] S. Richardson. Hele-Shaw flows with time-dependent free boundaries in which the fluid occupies a multiply connected region. *Eur. J. Appl. Math.*, **5**:97-122, (1994).

[91] S. Richardson. Hele-Shaw flows with time-dependent free boundaries involving a multiply connected fluid region. *Eur. J. Appl. Math.*, **12**:571-599, (2001).

[92] L. Rosenhead. The Kármán street of vortices in a channel of finite breadth. *Phil. Trans. Roy. Soc. London*, **228**:275-329, (1929).

[93] P. G. Saffman. *Vortex dynamics*. Cambridge University Press, Cambridge, (1992).

[94] P. G. Saffman & J. C. Schatzman. Properties of a vortex street of finite vortices. *SIAM J. Sci. Statist. Comput.*, **2**:285-295, (1981).

[95] P. G. Saffman & J. C. Schatzman. An inviscid model for the vortex street wake. *J. Fluid Mech.*, **122**:467-486, (1982).

[96] P. G. Saffman & J. C. Schatzman. Stability of a vortex street of finite vortices. *J. Fluid Mech.*, **117**:171-185, (1982).

[97] P. G. Saffman & J. S. Sheffield. Flow over a wing with an attached free vortex. *Stud. Appl. Math.*, **57**:107-117, (1977).

[98] P. G. Saffman & R. Szeto. Structure of a linear array of uniform vortices. *Stud. Appl. Math.*, **65**:223-248, (1981).

[99] H. Saito, T. Aioi & T. Kadokura. Bénard-von Kármán vortex street in an exciton-polariton superfluid. *Phys. Rev. B*, **86**:014504, (2012).

[100] K. Sasaki, N. Suzuki & H. Saito. Bénard-von Kármán vortex street in a Bose-Einstein condensate. *Phys. Rev. Lett.*, **104**:150404, (2010).

[101] F. Schottky. Über eine specielle function welche bei einer bestimmten linearen transformation ihres arguments unverändert bleibt. *J. Reine Angew. Math.*, **101**:227-272, (1887).

[102] L. I. Sedov. *Two-dimensional problems in hydrodynamics and aerodynamics*. Interscience Publishers, New York, (1965).

[103] M. Shao, H. Hu, M. Li, H. Ban, M. Wang & J. Jiang. Kármán vortex street assisted patterning in the growth of silicon nanowires. *Chem. Commun.*, **8**:793-794, (2007).

[104] A. M. P. Silva & G. L. Vasconcelos. Doubly periodic array of bubbles in a Hele-Shaw cell. *Proc. Roy. Soc. A*, **467**:346-360, (2011).

[105] I. J. Sobey. *Introduction to interactive boundary layer theory*. Oxford University Press, Oxford, (2000).

[106] K. C. Stewart, C. L. Niebel, S. Jung & P. P. Vlachos. The decay of confined vortex rings. *Exp. Fluids*, **53**:163-171, (2012).

[107] M. Subhash Reddy, S. Muddada & B. S. V. Patnaik. Flow past a circular cylinder with momentum injection: optimal control cylinder design. *Fluid Dyn. Res.*, **45**:015501, (2013).

[108] T. Suzuki & T. Colonius. Inverse-imaging method for detection of a vortex in a channel. *AIAA Journal*, **41**:1743-1751, (2003).

[109] S. Tanveer. New solutions for steady bubbles in a Hele-Shaw cell. *Phys. Fluids*, **30**:651, (1987).

[110] S. Tanveer. Singularities in water waves and Rayleigh-Taylor instability. *Proc. Roy. Soc. A*, **435**:137-158, (1991).

[111] G. I. Taylor & P. G. Saffman. A note on the motion of bubbles in a Hele-Shaw cell and porous medium. *Quart. J. Mech. Appl. Math.*, **12**:265-279, (1959).

[112] H. Telib & L. Zannetti. Hollow wakes past arbitrarily shaped obstacles. *J. Fluid Mech.*, **669**:214-224, (2011).

[113] G. Valiron. *Cours d'analyse mathématique: théorie des fonctions*. Masson et Cie, Paris, 3rd edition, (1966).

[114] M. Van Dyke. *An Album of Fluid Motion*. Parabolic, Stanford, (1982).

[115] G. L. Vasconcelos. Exact solutions for a stream of bubbles in a Hele-Shaw cell. *Proc. Roy. Soc. A*, **442**:463-468, (1993).

[116] G. L. Vasconcelos. Multiple bubbles in a Hele-Shaw cell. *Phys. Rev. E*, **50**:3306-3309, (1994).

[117] G. L. Vasconcelos. Exact solutions for steady bubbles in a Hele-Shaw cell with rectangular geometry. *J. Fluid Mech.*, **444**:175-198, (2001).

[118] G. L. Vasconcelos, M. N. Moura & A. M. J. Schakel. Vortex motion around a circular cylinder. *Phys. Fluids*, **23**:123601, (2011).

[119] H. von Helmholtz. Über discontinuierliche flüssigkeitsbewegungen. *Monatsber. Akad. Wiss. Berlin*, **23**:215-228, (1868).

[120] T. von Kármán. *Collected works of Theodore von Kármán*, Vol. 1. Butterworths, London, (1956).

[121] T. von Kármán & H. Rubach. On the resistance mechanisms of fluids and air. *Phys. Z.*, **13**:49-59, (1912).

[122] R. Wegmann. Constructive solution of a certain class of Riemann-Hilbert problems on multiply connected circular regions. *J. Comput. Appl. Math.*, **130**:139-161, (2001).

[123] D. Weihs & M. Boasson. Multiple equilibrium vortex positions in symmetric shedding from slender bodies. *AIAA Journal*, **17**:213-214, (1979).

[124] R. W. Whittlesey, S. Liska & J. O. Dabiri. Fish schooling as a basis for vertical axis wind turbine farm design. *Bioinsp. Biomim.*, **5**:035005, (2010).

[125] C. H. K. Williamson. Vortex dynamics in the cylinder wake. *Ann. Rev. Fluid Mech.*, **28**:477-539, (1996).

[126] K. Yu, M. B. S. Hesselberth, P. H. Kes & B. L. T. Plourde. Vortex dynamics in superconducting channels with periodic constrictions. *Phys. Rev. B*, **81**:184503, (2010).

[127] L. Zannetti. Vortex equilibrium in flows past bluff bodies. *J. Fluid Mech.*, **562**:151-171, (2006).

[128] L. Zannetti & D. Lasagna. Hollow vortices and wakes past Chaplygin cusps. *Eur. J. Mech. B Fluids*, **38**:78-84, (2013).